Electrokinetic and electrohydrodynamic problems in multifluid flows

Submitted in part fulfilment of the
requirements for the degree of
Doctor of Philosophy of Imperial College London
and the
Diploma of Imperial College London
by

Elizaveta Dubrovina

Department of Mathematics
Imperial College London

May 2016

Declaration of Originality

I certify that this thesis, and the research to which it refers, are the product of my own work, and that any ideas or quotations from the work of other people, published or otherwise, are fully acknowledged in accordance with the standard referencing practices of the discipline.

Elizaveta Dubrovina
May 2016

Copyright Declaration

Acknowledgements

I would like to thank my primary supervisor Prof Richard Craster for his guidance and constant support throughout my PhD. I would also like to thank my secondary supervisor Prof Demetrios Papageorgiou for his helpful advice and excellent suggestions. Finally, I would like to acknowledge the financial support of NERC.

Many thanks must go to all the lovely people I have met during my time at Imperial College. Sophie for all the advice and encouragement during our walks in Hyde Park; Curtis and David for the fun coffee breaks; Tom and Marco for fun and silliness; Joe and Liam for the coffee breaks, support and conference adventures; Alice for the incredibly useful mathematical discussions; Susana, Alex, Michael, Adam, Radu, Hannah and Vikas for being great officemates and excellent travel companions during conferences; Dan and Michael for the fun times in the last stretch of the writing up period. A special mention must also go to all the friends that despite often being in other countries have provided constant support during the past 3.5 years.

I would like to thank my family for the inspiration, the constant encouragement and support without which I would not have gotten this far.

Finally I would like to thank Jonathan Kim for always being there for me, even on the rainiest days.

Abstract

The present thesis deals with microfluidic systems under the influence of electric fields. The purpose of this research is to identify key behaviours which are highly relevant for applications in lab-on-chip devices such as pH control, patterning, mixing and cell trapping. In the first part of the thesis we consider the electrokinetics of charged, porous membranes and present a mathematical model for the ionic transport under the effects of a horizontal electric field. First, we investigate the behaviour of a system that consists of one anion membrane with two reservoirs and produce numerical solutions with the aim to gain a better understanding of the mechanisms that lead to overlimiting current. We then analyse the features of a system where a bipolar membrane is held in an electrolyte bath with water and a salt. We use our model to confirm findings from experiments such as the hysteretic behaviour of the IV curve and the water splitting phenomenon. In the second part of the thesis we examine the behaviour of interfaces between two fluids that are sandwiched between two electrodes. We find that introducing a constant flow rate into the system leads to time modulated travelling waves. In the case of flat channel walls these look like moving strips which are reminiscent of the patterns found in the no flow case. Adding corrugations on one or both electrodes leads to a rich variety of dynamics. We develop a Floquet stability analysis which takes into account the fact that the base state of the system is nonuniform. This is a very useful tool for identifying the different types of behaviours which arise as we change the applied voltage and the overall flow rate. We examine the streamlines of the fluid to explore the advantages of the different regimes: just by changing the applied voltage it is possible to transition from an environment which is favourable to efficient mixing to one which could enhance cell trapping.

Contents

List of Publications

Dubrovina, E., Craster R. V. & Papageorgiou D. T. (2016). Two layer electrified pressure-driven flow in topographically structured channels. *Journal of Fluid Mechanics, submitted for publication.*

List of Figures

Part I.

Electrokinetics of ion exchange membranes

1. Introduction

Ion selective membranes have long been used for the production of potable water and for the treatment of industrial waste (Strathmann *et al.*, 2013; Xu, 2005). In more recent years they have been integrated into microfluidic devices and their features have been exploited to enhance a variety of processes on diagnostic chips (see Slouka *et al.* (2014) for a comprehensive review). The main feature is ion selectivity and is described in a review by Sollner (1950) as the ability of a charged porous membrane to allow the passage of counter-ions and to prevent the flow of co-ions. This is achieved by restricting the width of the pores to be narrow enough for the fixed surfaces charges to have an effect. The maximum pore/channel size that ensures ion selectivity is found by estimating the Debye length. This is the characteristic thickness of the layer that forms near a charged surface: a charged plate will attract oppositely charged ions (counter-ions) that will rearrange themselves to form the electrical double layer (see figure 1.1). The charge of this layer will balance the surface charge of the plate in order for the system to remain electroneutral. It is necessary for the double layers to overlap in nanopores and nanochannels to create a barrier for co-ions and enable the free flow of counter-ions.

Ion exchange membranes are mostly used in large scale industrial processes, but are also incorporated in microfluidic devices in particular for proteomics analyses (Ko *et al.*, 2012; Lee *et al.*, 2008; Wang *et al.*, 2005). One of the challenges of analysing small samples of blood is the large variation of protein concentration. Microfluidic devices operate with nano and pico litre volumes of fluid meaning it is harder to detect some biomolecules which exist in low concentration in the sample. Wang *et al.* (2005) and Lee *et al.* (2008) developed biomolecule preconcentrators to collect and trap analytes. They used an ion selective nanofluidic filter to generate an ion-depletion region to prevent convection of molecules and trap them upstream (see figure 1.2).

By joining a cation and an anion membrane to form a p-n junction a bipolar membrane is created. Applying a forward bias causes the formation of an ion enrichment region at the junction. A reverse bias causes the ions to deplete at the junction thus increasing the local electric field which at high enough voltages splits water into H^+ and OH^- ions (Cheng & Chang, 2011; Conroy *et al.*, 2012). This phenomenon can be exploited for pH

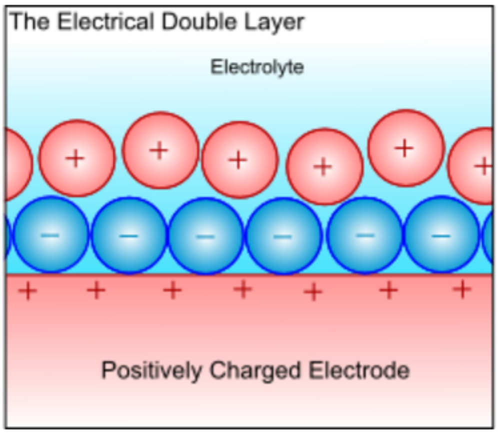

Figure 1.1. Schematic of an electrical double layer in a liquid in contact with a positively charged surface (Image taken from *DoITPoMS Teaching and Learning Packages*).

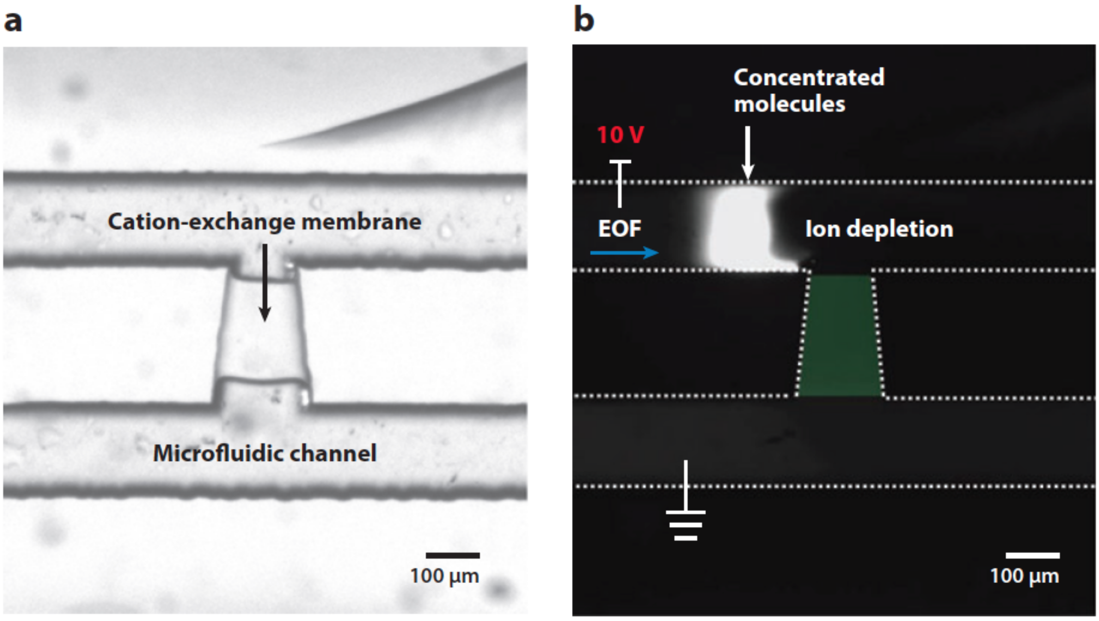

Figure 1.2. (a) A cation-exchange membrane built into a microfluidic channel. (b) The membrane causes a depletion region to form on one side which is used to concentrate charged dye molecules. Abbreviation: EOF, electroosmotic flow. Figure and caption taken from Slouka *et al.* (2014)

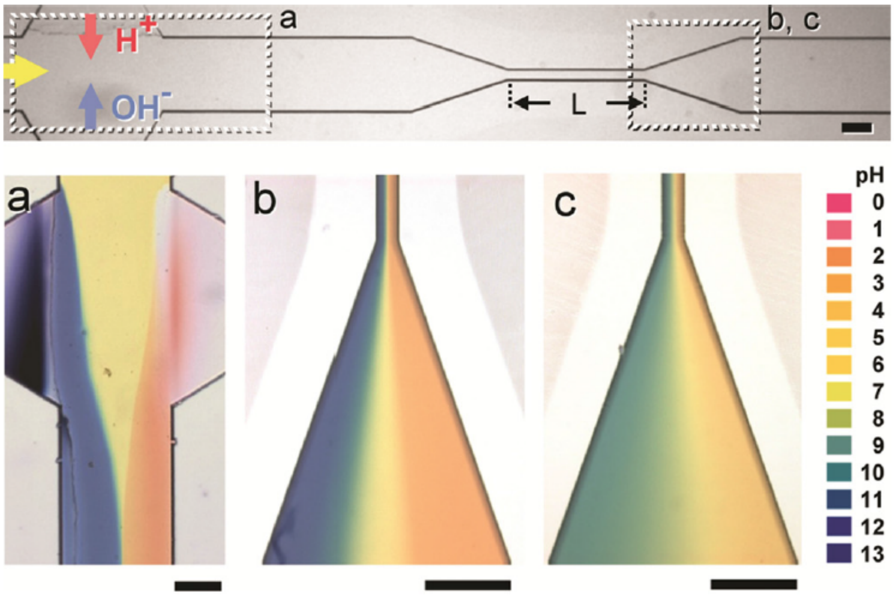

Figure 1.3. (a) Abrupt pH profile builds up near the pH actuators upstream. Different pH gradients were generated across a 500 lm wide channel downstream after passing through a 0.8mm long (b) or a 2mm long *(c)* , 50 lm wide narrowed channel. The scale bars in images indicate 200 lm. Figure and caption taken from Cheng & Chang (2011)

control which in turn is used to achieve isoelectric focusing for molecular separation in microfluidic devices (Cheng & Chang, 2011; Kohlheyer *et al.*, 2007) (see figure 1.3).

1.1. Ion exchange membranes

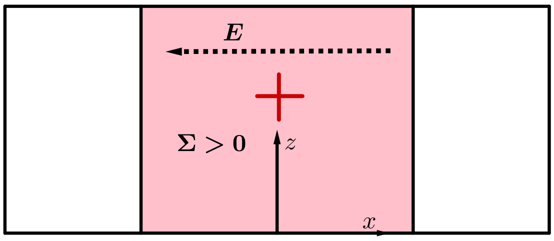

Figure 1.4. Schematic of an anion selective membrane where Σ is the membrane charge.

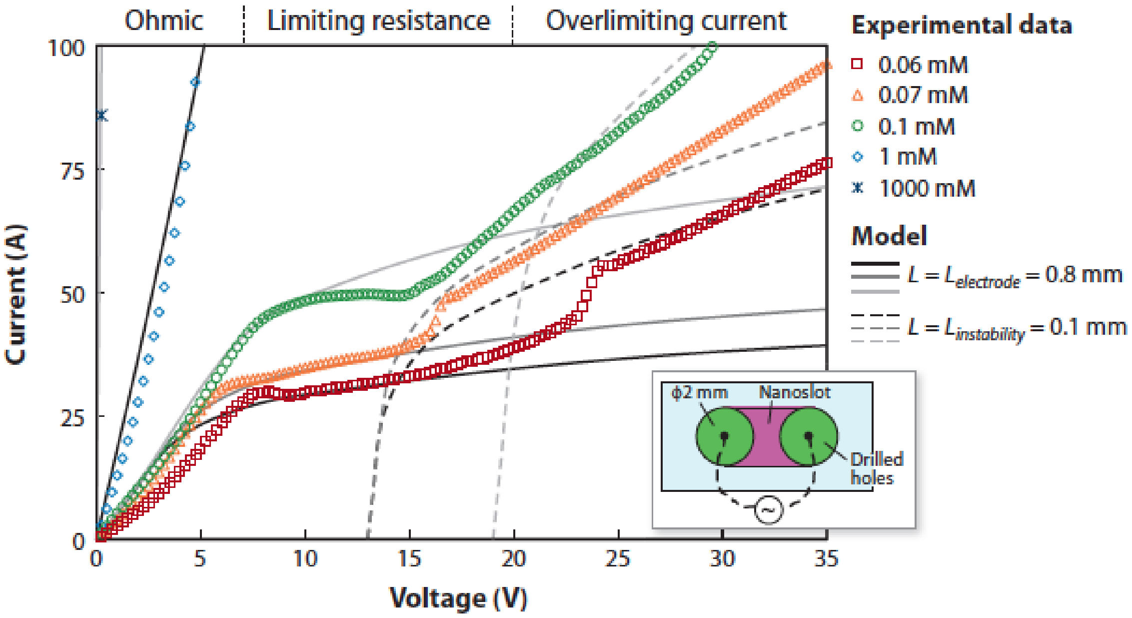

Figure 1.5. Current-voltage characteristics of a nanoslot (inset) for varying ionic strengths. Figure and caption taken from Yossifon *et al.* (2009)

One of the most interesting aspects of ion exchange membranes which is still not fully explained theoretically is overlimiting current (OLC), a behaviour that was known decades ago (Frilette, 1957). The setup of the system is shown in fig. 1.4: an ion selective nano-porous membrane is placed in, say, a symmetric 1 : 1 electrolyte bath and an electric field E is applied to the system. At low voltages the current voltage curve has an Ohmic behaviour and this is called the underlimiting regime. However as the voltage increases the applied electric field causes the counter-ions to move into the membrane and the co-ions away from it until the concentration of counter-ions there drops to nearly zero. The co-ions also drop to almost zero in order to keep electroneutrality in the reservoirs thus creating a depletion region on one side of the membrane which prevents the flow of the current: this is when the system is in the limiting regime. However it has been observed experimentally that for sufficiently high voltages the current exceeds the classical limit derived theoretically by Levich (1962) and the current voltage curve enters a second linear region called the overlimiting region (see figure 1.5).

There is a considerable amount of literature aimed at understanding the mechanisms that lead to OLC. Manzanares *et al.* (1993), for instance, considered the one-dimensional, time-dependent, non equilibrium problem of a system with a membrane and two reservoirs. They conducted a numerical study and found that in the depletion side, the classical electroneutrality assumption breaks down: there is in fact a space charge layer which allows current to flow. The ion concentrations in this layer are small but the fluxes are constant throughout the system which means that there must be an increase in the electric field: it is this space charge region that allows the flow of currents that exceed the limiting current. Ben & Chang (2002) analysed a similar system and used matched asymptotic expansions from the extended polarised region to the membrane to smooth out a singularity that arises when electroneutrality is assumed. They also derived an expression for the flux beyond the limiting current.

Yossifon *et al.* (2009) conducted numerical simulations for a slightly different geometry: a nanochannel with axisymmetric micro-reservoirs on both sides. They also concluded that the presence of OLC is due to space charge and to field-focusing effects: as all the current tries to flow from the bulk into the nano slot a space charge region forms at the depletion side. The existence of depletion and enrichment regions was confirmed by Wang *et al.* (2009) who conducted a full 2D numerical study which included hydrodynamic effects. Moreover, they found that the behaviour of the ion concentrations in the longitudinal direction corresponds to findings from one dimensional studies.

Other mechanisms were found to have a role in the formation of OLC: Rubinstein & Zaltzman (2000) first predicted the existence of a microvortex instability at an ion selective membrane. This was later verified experimentally and thought to be connected to OLC (Rubinstein *et al.*, 2008). There are many more studies of this microvortex instability which are not included here as they are not relevant to the work presented in this thesis. The reader is referred to a review on the effect of microhydrodynamics on nanofluidic flow by Chang *et al.* (2012).

Yet another mechanism was proposed by Andersen *et al.* (2012) who suggested that OLC is due to current induced membrane discharge. They proposed a model which included the transport of water ions through the membrane, the water self-ionisation reaction and the reaction of the membrane with the water. According to this model the membrane surface groups react with the water which leads to loss of selectivity of the membrane and hence allows the passage of currents higher than the limiting current. In this model no space charge appears at the depletion side.

In this thesis asymptotic and numerical methods are developed to study the problem of OLC in an anion selective membrane and this will be presented in section §3.

1.2. Bipolar membranes

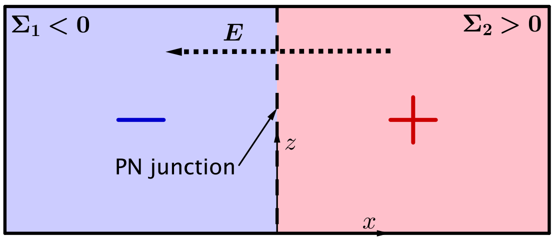

Figure 1.6. Schematic of a bipolar membrane.

Field enhanced water dissociation is a curious phenomenon that occurs in bipolar membranes under reverse bias. The setup of the system is shown in fig.1.6: a bipolar membrane (BM) is formed by joining a negatively charged membrane to a positively charged membrane. The BM is held in an electrolyte bath with water and a salt. An electric field is applied across the membrane which causes the salt ions to deplete at the junction and the water to dissociate into H^+ and OH^- ions.

Mafe & Ramirez (1997) considered the steady state problem with a model that assumed ion depletion in the electric double layer and a smooth ion concentration variation across the whole membrane. They proposed two mechanisms for field enhanced water dissociation: the second Wien effect according to which the water dissociation rate depends on the electric field and the chemical reaction model which takes into account the reaction of water with the surface groups of the membrane. Both mechanisms are modelled by an Arrhenius dependence:

$$k_d = A \exp\left(-\frac{E_a}{RT}\right) \tag{1.1}$$

where k_d is the dissociation rate, A is the dissociation rate before the electric field is applied, R is the molar gas constant, T is the absolute temperature and E_a is the activation energy which takes different forms depending on the model.

Cheng & Chang (2011) did experiments with bipolar membranes with an applied electric field that is first increased then decreased. Their results show that the IV curve (current against potential) has a hysteretic behaviour (figure 1.7) which implies that the problem is time dependent.

These findings have motivated Conroy *et al.* (2012) to use a transient model. They

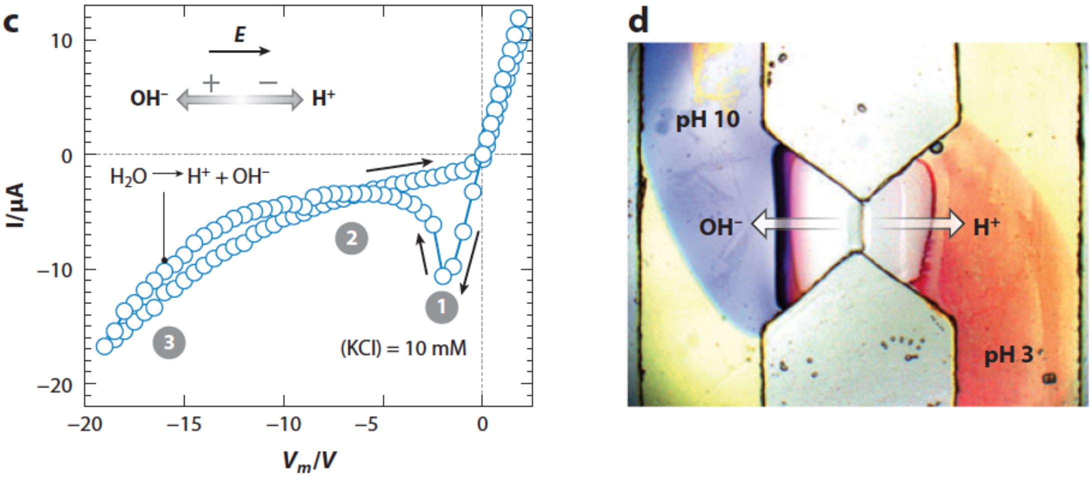

Figure 1.7. (c) I-V curve measured by Cheng & Chang (2011) in the reverse bias region showing large overlimiting current and hysteresis. The spike at $-2V$ during the backward scan is due to residual ions from water splitting in the bipolar membrane. Equilibration to the limiting current at $-5V$ occurs after the depletion of residual ions. The numbers 1, 2, and 3 represent the hysteresis, saturation, and water-splitting regimes, respectively. (d) Image of pH-sensitive dye across the bipolar membrane showing ejection of H^+ and OH^- ions. Figure taken from Slouka *et al.* (2014).

use a linearised Arrhenius dependence for the water dissociation rate and their results confirm the hysteretic behaviour of the IV curve and the water splitting predicted by the experiments.

This analysis is repeated in section §4 of this work. New results are also presented: a second salt is added to the system (§4.2) and a non-linear Arrhenius dependence is used to model the water dissociation rate (§4.3).

2. Mathematical formulation

2.1. Governing equations

In this section we provide the mathematical formulation for the fluid flow and the ionic transport in a porous membrane (Conroy *et al.*, 2012). An electric field $\mathbf{E}$ is applied to the system which is irrotational hence it is expressed it in terms of the voltage potential $\mathbf{E} = -\nabla\phi$. The membrane is considered to be porous so Darcy's law applies for the bulk fluid flow:

$$\nabla P = -\frac{\mu}{\Pi}\mathbf{u} + \rho^e \mathbf{E} \tag{2.1}$$

$$\nabla \cdot \mathbf{u} = 0 \tag{2.2}$$

where $\mathbf{u} = (u, 0, w)$ is the filtration rate, P is the pressure, μ is the viscosity, Π is the permeability and ρ^e is the charge density defined by:

$$\rho^e = F \sum_i z_i C_i$$

where C_i is the ionic concentration of species i, z_i is the valency, $F = N_A e$ is the Faraday constant, e is the charge of an electron and N_A is the Avogadro number.
The transport of ionic concentrations is governed by the Nernst-Planck equations which are derived from the mass conservation for each species i (Chang & Yeo, 2010):

$$n\frac{\partial C_i}{\partial t} + \mathbf{u} \cdot \nabla C_i = \omega_i k_B T \nabla \cdot \left(z_i \frac{e}{k_B T} C_i \nabla \phi + \nabla C_i \right) + R_i \tag{2.3}$$

where n is the porosity, k_B is Boltzmann's constant, T is the absolute temperature, ω_i the ion mobility and R_i is the generation rate of the species. The first two terms on the right hand side represent contributions to the flux due to electromigration and diffusion. The mobility ω_i represents how easily a charged particle in a solution can move when an electric field $\mathbf{E}$ acts on it and it is related to the ionic diffusion coefficient through the

Stokes-Einstein relation (Chang & Yeo, 2010):

$$\omega_i = \frac{D_i}{k_b T N_A}$$

The voltage potential is described by the Poisson equation:

$$\epsilon_0 \epsilon \nabla^2 \phi = \rho^e + F\Sigma \tag{2.4}$$

where ϵ_0 is the free space permittivity, ϵ is the relative permittivity and Σ is the charge of the membrane.

The equations are non-dimensionalised with the following scalings (Conroy *et al.*, 2012):

$$x = Lx', \qquad z = Hz', \qquad (u, w) = \frac{\Pi|\Sigma| k_B T F}{\mu e L}(u', \delta w'), \tag{2.5}$$

$$\phi = \phi_c \phi', \qquad t = \frac{nL^2}{k_B T \omega} t', \qquad P = \frac{|\Sigma| k_B T F}{e} P', \tag{2.6}$$

where ϕ_c is the maximum potential, L is the half-length of the domain, H is the domain depth and $\delta = H/L \ll 1$ is a small parameter. For simplicity all dashes are dropped. The dimensionless continuity equations and Darcy's law take the following form:

$$\frac{\partial u}{\partial x} + \frac{\partial w}{\partial z} = 0 \tag{2.7}$$

$$\frac{\partial P}{\partial x} = -u - \psi \rho^e \frac{\partial \phi}{\partial x} \tag{2.8}$$

$$\frac{\partial P}{\partial z} = -\delta w - \psi \rho^e \frac{\partial \phi}{\partial z} \tag{2.9}$$

where $\psi = \phi_c e / k_B T$ represents the dimensionless strength of the electric field. The dimensionless Nernst-Planck equations are:

$$\begin{aligned}\frac{\partial C_i}{\partial t} + Pe\left(u\frac{\partial C_i}{\partial x} + w\frac{\partial C_i}{\partial z}\right) =& \alpha_i \frac{\partial}{\partial x}\left(\psi C_i \frac{\partial \phi}{\partial x} + \frac{\partial C_i}{\partial x}\right) \\ & \delta^2 \alpha_i \frac{\partial}{\partial z}\left(\psi C_i \frac{\partial \phi}{\partial z} + \frac{\partial C_i}{\partial z}\right) + DaR\end{aligned} \tag{2.10}$$

The following dimensionless groups emerge:

$$\alpha_i = \frac{\omega_i}{\omega_1}, \qquad Pe = \frac{\Pi F|\Sigma|}{\mu e \omega}, \qquad Da = \frac{L k_a C_a \epsilon_r}{k_B T \omega |\Sigma|} \tag{2.11}$$

where Pe is the Peclet number which represents the ratio between convection and diffusion of ions and the Damkholer number Da is the ratio of water dissociation to ion diffusion (the latter will be discussed more in depth in §4). The Poisson equation for the voltage becomes:

$$\frac{\partial^2 \phi}{\partial x^2} + \delta^2 \frac{\partial^2 \phi}{\partial z^2} = -\chi^2 \rho^e - \chi^2 \bar{\Sigma}, \tag{2.12}$$

$$\rho^e = \sum_i C_i \tag{2.13}$$

where $\chi = FL^2|\Sigma|e/\psi\epsilon\epsilon_0 k_B T$ is the inverse Debye length and $\bar{\Sigma}$ is the dimensionless membrane charge.
We assume that the membrane is long and this i.e. $\delta \ll 1$ and derive a one dimensional system. Hydrodynamic effects are ignored by setting $Pe \ll 1$ which is consistent with the assumption of a constant water concentration and has been done in previous work. This leads to the following system:

$$\frac{\partial^2 \phi}{\partial x^2} = -\chi^2(\rho^e + \bar{\Sigma}) \tag{2.14}$$

$$\frac{\partial C_i}{\partial t} = \alpha_i \frac{\partial}{\partial x}\left(\psi C_i \frac{\partial \phi}{\partial x} + \frac{\partial C_i}{\partial x}\right) + Da R_0 \tag{2.15}$$

This system of equations will be analysed in the case of an anion selective membrane (§3) and in the case of a bipolar membrane (§4). The boundary conditions will be defined for each case in the next sections.

2.2. Numerical methods

The behaviour of the above system of equations (2.14-2.15) has been analysed using two time dependent, numerical codes. The first one was written in MATLAB specifically for this problem, the second one was based on PDECOL, a FORTRAN solver for PDEs (Madsen & Sincovec, 1979). Both codes rely on the method of lines, a numerical approach through which the spatial partial derivatives are replaced by algebraic approximations at each grid point (Schiesser, 2012). This reduces a system of m PDEs to a system of $m \times N$ ODEs in just one variable t, with N the number of grid points in the spatial variable x. The spatial discretisation in the MATLAB code is performed using second order, finite difference formulae. The spatial discretisation in the PDECOL solver is based on a finite element routine where the domain is subdivided by an equally spaced grid of N points and the solution is approximated by a cubic spline in each interval. Once the system of PDEs is transformed into a time-dependant system of ODEs, the latter needs to be solved with the help of an implicit numerical procedure. The main disadvantage of an implicit scheme is that the code needs to solve the matrix equation at every step. However this is counteracted by the advantage offered by the ability to choose a relatively large time step which would not otherwise be possible when solving for stiff systems. The time integration is performed by using the stiff ODE solver ode15s in MATLAB while in PDECOL it is performed using a technique based on Gear's method. The results from the two numerical schemes were in perfect agreement with each other but the MATLAB code was soon abandoned in favour of PDECOL due to the higher efficiency of the latter.

3. Overlimiting current (OLC) in an anion selective membrane

3.1. Guoy-Chapman equilibrium theory and Levich's expression for OLC

In this chapter we consider a binary monovalent electrolyte on an anion membrane of charge σ placed at $|x| < L_{men}$ between two reservoirs, where L_{mem} is half the length of the membrane. The ion concentrations are C^+ for the positive ions and C^- for the negative ions. The governing equations (2.14-2.15) take the following form:

$$\frac{\partial^2 \phi}{\partial x^2} = -\chi^2 (C^+ - C^- + \Sigma) \tag{3.1}$$

$$\frac{\partial C^\pm}{\partial t} = \frac{\partial}{\partial x}\left(\frac{\partial C^\pm}{\partial x} \pm C^\pm \frac{\partial \phi}{\partial x}\right) \tag{3.2}$$

where Σ is the surface charge of the membrane:

$$\Sigma = \begin{cases} \sigma, & \text{for } |x| < L_{mem} \\ 0, & \text{for } |x| > L_{mem} \end{cases}$$

In the numerical scheme the step function in Σ is approximated by a tanh function. The boundary conditions are: $C^\pm(\pm L) = C_0$, $\phi'(-L) = -I$, $\phi(L) = 0$ where L is the half length of the domain in the x direction, C_0 is the bulk concentration and I is the total current through the system.

We begin by considering a system in electrical equilibrium and we look at the classical Guoy-Chapman theory (Chang *et al.*, 2012). We assume that ion transport is in equilibrium and so there is no ionic flux and the ionic transport equations become:

$$\frac{\partial C^\pm}{\partial x} \pm C^\pm \frac{\partial \phi}{\partial x} = 0 \tag{3.3}$$

and so the concentrations are given by a Boltzmann distribution that depends on the local electric potential ϕ:

$$C\pm = C_0 e^{\mp\phi} \tag{3.4}$$

The above expression means that the net charge in the membrane is given by $C^+ - C^- = -2C_0 \sinh\phi$. The charge of the membrane σ must balance the net charge of the mobile ions in order to preserve electroneutrality which leads to the expression for the Donnan potential in the membrane:

$$\phi_d = \sinh^{-1}\left(\frac{-\sigma}{2C_0}\right) \tag{3.5}$$

Next we consider the system with a forcing i.e. the electric field $\mathbf{E}$: after a transient stage the system reaches a steady state. Levich (1962) first observed that after equilibration counterions will have moved into the membrane causing their concentration to drop on one side of the membrane. The concentration of co-ions will also drop there to preserve electroneutrality thus creating a depletion region. The total concentration of ions in the bulk $C = C^+ + C^-$ decreases linearly from the reservoir to the boundary:

$$C = 2C_0 - J(x + L) \tag{3.6}$$

where J is the total flux. Assuming that the total concentrations of ions C drops to zero in the depletion region we get the following expression for the limiting current:

$$J_{lim} = \frac{2C_0}{L - L_{mem}} \tag{3.7}$$

where L_{mem} is half the length of the membrane. It has been found in experiments that for high enough voltage the current in the system goes above this limit: there have been many theories on the reason behind this but none of them has fully explained this overlimiting behaviour.

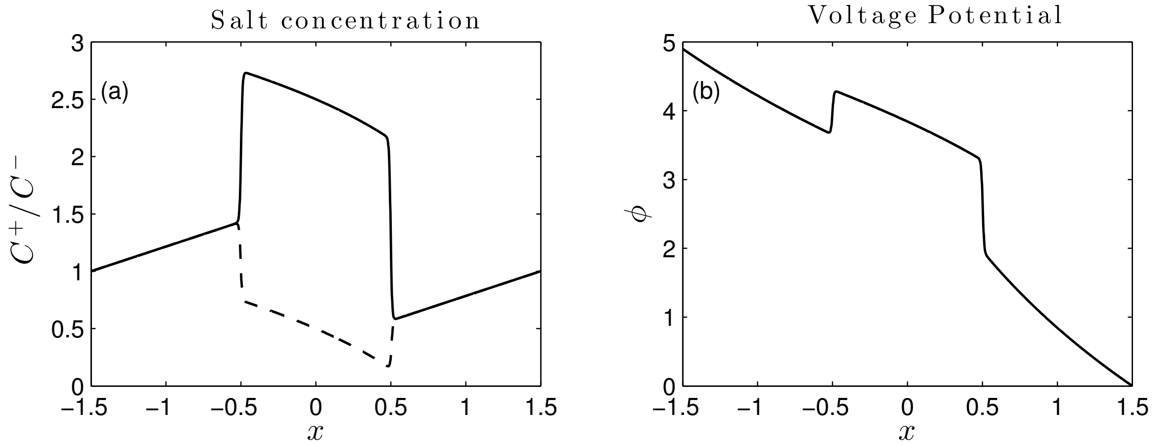

Figure 3.1. Concentration profiles for $t = \infty$ in the limiting current regime (a) Salt ion concentration profiles (solid line - C^+, dashed line - C^-). (b) Voltage potential. Boundary condition for the voltage potential: $\phi'(-L) = -1.5$. $\sigma = 2$.

3.2. Numerical results for the transient problem

Manzanares *et al.* (1993) performed transient simulations of the problem described above and found that for large enough voltages a space charge region forms on the depletion side and allows current above the limit to flow. In this section a numerical scheme is used to reproduce results by Manzanares *et al.* (1993), this is useful as a reliable numerical method is required to produce the results that are then compared to asymptotics.

Our computations are performed for $L = 1.5$, $L_{men} = 0.5$, $C_0 = 1$, $\sigma = 2$ and $\chi = 10^3$. Figures 3.1 and 3.2 exhibit the solutions at $t = \infty$ for the limiting current case and overlimiting current case respectively. We see from figure 3.1 that the solution reaches a steady state with both the ion concentrations and the potential varying almost linearly in the three regions and we later show that in this regime the electroneutral assumption leads to an analytical solution that gives reasonable agreement with the full numerical solution.

We see from figure 3.2 that for overlimiting currents a depletion region forms at the interface between the reservoir and the membrane on the anodic side. Fig. 3.3 depicts the depletion region and the space charge in that region where $\rho = -(C^+ - C^- + \Sigma)$. This space charge is responsible for overlimiting current according to Manzanares *et al.* (1993).

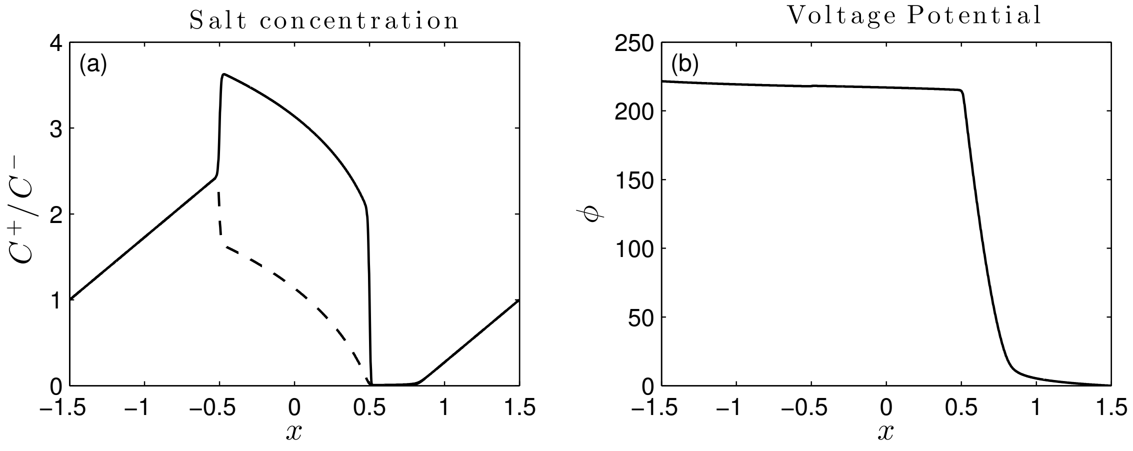

Figure 3.2. Overlimiting current. (a) Salt ion concentration profiles (solid line - C^-, dashed line - C^+). (b) Voltage potential. Boundary condition for the voltage potential: $\phi'(-L) = -6$.

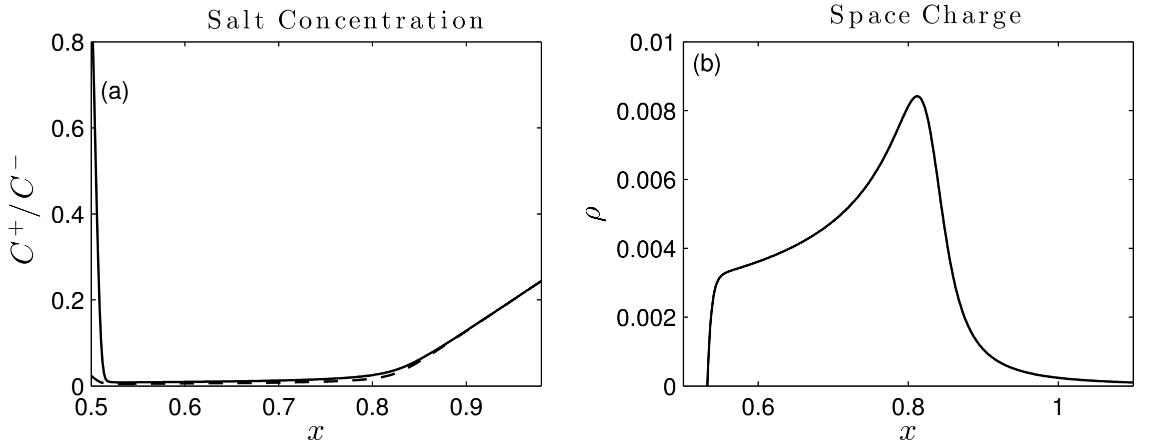

Figure 3.3. (a) Salt ion concentration profiles at depletion side, (solid line - C^-, dashed line - C^+). (b) Space charge layer at depletion layer. Boundary condition for the voltage potential: $\phi'(-L) = -6$.

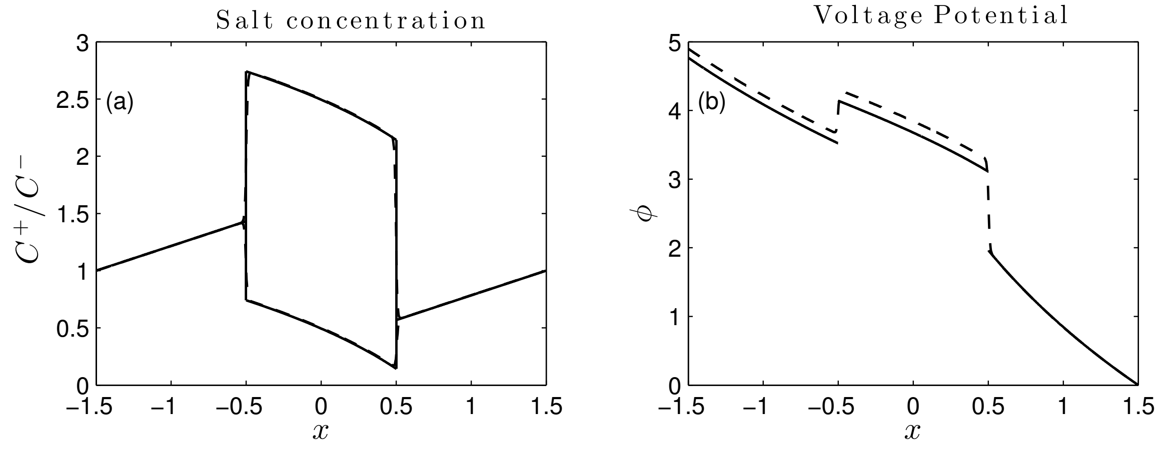

Figure 3.4. (a) Salt ion concentration profiles and (b) voltage potential. Solid line - analytic solution, dashed line - numerical solution. Boundary condition for the voltage potential: $\phi'(-L) = -1.5$. $\sigma = 2$.

3.3. Analytical solution for the case with currents below the limiting current

In this section we present an analytical solution of the steady state for the full membrane and reservoirs system in the underlimiting current regime and with $\chi \gg 1$. Such a solution was previously found by Andersen & Bruus (2012) using the expression for the Donnan potential given in eq.3.5 to determine the matching conditions between the membrane and the reservoirs. Here we present an analytical solution calculated using a different set of matching conditions which are based on mathematical arguments without assuming electroneutrality in the membrane.

For simplicity, let us define two constants a and b as the sum $a = J^+ - J^-$ and difference $b = J^+ + J^-$ of the two fluxes $J^\pm$. The solution in the region $-L \leq x < -L_{mem}$ will be denoted by a subscript 1, that in the region $|x| < L_{mem}$ by a subscript 2 and a subscript 3 for $L_{mem} < x \leq L$. Electroneutrality in the reservoirs is assumed as the current is below the limiting current. The governing equations (3.2) become:

$$C^+ - C^- + \Sigma = 0 \tag{3.8}$$

$$2\frac{\partial C^-}{\partial x} - \Sigma\frac{\partial \phi}{\partial x} = -b \tag{3.9}$$

$$(2C^- - \Sigma)\frac{\partial \phi}{\partial x} = -a \tag{3.10}$$

In regions 1 and 2 there is no membrane charge ($\Sigma = 0$) and so the solution in the region $x < -L_{mem}$ is given by:

$$C_1^{\pm} = C_0 - \frac{b}{2}(x + L) \tag{3.11}$$

$$\phi_1 = \frac{a}{b}\ln(C_0 - \frac{b}{2}(x + L)) + A \tag{3.12}$$

where A is a constant and in the region $x > L_{mem}$:

$$C_3^{\pm} = C_0 - \frac{b}{2}(x - L) \tag{3.13}$$

$$\phi_3 = \frac{a}{b}\ln(C_0 - \frac{b}{2}(x - L)) - \frac{a}{b}\ln(C_0) \tag{3.14}$$

The solution inside the membrane $|x| < L_{mem}$ is more complex:

$$C_2^- = -\frac{a\sigma}{2b}\left(\mathrm{W}(d\exp\eta x) + 1\right) + \frac{\sigma}{2} \tag{3.15}$$

where $\eta = b^2/\sigma a$ and d is an integration constant to be found. W is the Lambert W function (Corless *et al.*, 1996) that satisfies:

$$\mathrm{W}(z)\exp\left(\mathrm{W}(z)\right) = z$$

In order to find ϕ in this region we need to solve the following ODE:

$$\frac{\partial \phi}{\partial x} = \frac{a}{(\sigma - 2C_2^-)} = \frac{b}{\sigma(\mathrm{W} + 1)} \tag{3.16}$$

From numerics we know that for $\sigma = 2$, η is small enough so we approximate $\mathrm{W}(d\exp\eta x)$ with a Taylor expansion (Corless *et al.*, 1996):

$$\begin{aligned} \mathrm{W}(d\exp\eta x) \approx \mathrm{W}(d(1 + \eta x + \eta^2 x^2)) &= \sum_{n=1}^{\infty} \frac{(-n)^{n-1}}{n!}(d(1 + \eta x + \eta^2 x^2))^n \\ &= a_0 + a_1\eta x + a_2\eta^2 x^2 + O(\eta^3 x^3) \end{aligned} \tag{3.17}$$

where a_0, a_1 and a_2 have the following form:

$$
\begin{aligned}
a_0 &= \sum_{n=1}^{\infty} \frac{(-n)^{n-1}}{n!} d^n; \\
a_1 &= \sum_{n=1}^{\infty} \frac{(-1)^{n-1} n^n}{n!} d^n; \\
a_2 &= d + \sum_{n=2}^{\infty} \frac{(-n)^{n-1}}{n!} \left(\binom{n}{n-2} + \binom{n}{n-1} \right) d^n;
\end{aligned}
$$

ϕ is found by substituting the expression from eq. (3.17) for W into (3.16):

$$\frac{\partial \phi_2}{\partial x} = \frac{a}{(\sigma - 2C_2^-)} = \frac{b}{\sigma(a_0 + a_1 \eta x + a_2 \eta^2 x^2 + 1)}$$

$$\phi_2 = \frac{b}{\sigma \eta \sqrt{a_2} \sqrt{a_0 + 1 - a_1^2/4a_2}} \arctan \frac{\sqrt{a_2}\eta x + a_1/2\sqrt{a_2}}{\sqrt{a_0 + 1 - a_1^2/4a_2}} + B \tag{3.18}$$

where B is a constant. We find a by adding the two equations for $C^{\pm}$ (eq.3.8-3.10) to get $\phi'(-L) = -I = -a/2C_0$. Integrating the two equations for $C^{\pm}$ (eq.3.8-3.10) and subtracting the resulting equations one from the other, we get one constraint for b and d:

$$\int_{-L}^{L} (C^+ - C^-) \frac{\partial \phi}{\partial x} \mathrm{d}x = -2Lb$$

which leads to the following relation:

$$
\begin{aligned}
&\int_{-L_{mem}-\alpha}^{-L_{mem}+\alpha} (C^+ - C^-) \frac{\partial \phi}{\partial x} \mathrm{d}x + \int_{L_{mem}-\alpha}^{L_{mem}+\alpha} (C^+ - C^-) \frac{\partial \phi}{\partial x} \mathrm{d}x \\
&- \left[\frac{b}{\eta \sqrt{a_2} \sqrt{a_0 + 1 - a_1^2/4a_2}} \arctan \frac{\sqrt{a_2}\eta x + a_1/2\sqrt{a_2}}{\sqrt{a_0 + 1 - a_1^2/4a_2}} \right]_{-L_{mem}}^{L_{mem}} = -2Lb
\end{aligned} \tag{3.19}
$$

where $\alpha > 0$ is a small parameter.
$C^{\pm}$ and ϕ have a jump at $x = \pm L_{mem}$ so the first integral on the left hand side of equation (3.19) is approximated by:

$$\begin{aligned}-\sigma(\phi_2(-L_{mem}+\alpha)-\phi_1(-L_{mem}-\alpha))\int_{-L_{mem}-\alpha}^{-L_{mem}+\alpha} H(x)L_{mem}\mathrm{d}x = \\ -\sigma(\phi_2(-L_{mem}+\alpha)-\phi_1(-L_{mem}-\alpha))/2\end{aligned} \tag{3.20}$$

Similarly, the second integral on the left hand side of equation (3.19) becomes:

$$\begin{aligned}-\sigma(\phi_3(L_{mem}+\alpha)-\phi_2(L_{mem}-\alpha))\int_{L_{mem}-\alpha}^{L_{mem}+\alpha} H(x)L_{mem}(x)\mathrm{d}x = \\ -\sigma(\phi_3(L_{mem}+\alpha)-\phi_2(L_{mem}-\alpha))/2\end{aligned} \tag{3.21}$$

In order to use (3.20) and (3.21) we need to find the two constants A and B in (3.12) and (3.18). B is found by adding the two equations for $C^{\pm}$ (eq. 3.8-3.10) and integrating over the jump at $x = L_{mem}$:

$$\left[C^{+}+C^{-}\right]_{L_{mem}-\alpha}^{L_{mem}+\alpha} + \int_{L_{mem}-\alpha}^{L_{mem}+\alpha}(C^{+}-C^{-})\frac{\partial\phi}{\partial x}\mathrm{d}x = -\cancelto{0}{\int_{L_{mem}-\alpha}^{L_{mem}+\alpha} b\,\mathrm{d}x} \tag{3.22}$$

which leads to:

$$2C_3^{\pm}(L_{mem}+\alpha) - 2C_2^{-}(L_{mem}-\alpha) + \sigma - \sigma(-\frac{1}{2})B = 0 \tag{3.23}$$

A is found in a similar way by integrating the sum of the two equations for $C^{\pm}$ over the jump at $x = -L_{mem}$.
From Manzanares *et al.* (1993) we have the second constraint for b and d:

$$\frac{a-b}{a+b} = \frac{\int_{-L}^{L} C^{-}\mathrm{d}x}{\int_{-L}^{L} C^{+}\mathrm{d}x} \tag{3.24}$$

which leads to the following relation:

$$\frac{a-b}{a+b} = \frac{2a_0L_{mem} + 2a_2\eta^2L_{mem}^3/3 + 2L_{mem} - 2bL_{mem}/a - 4bC_0/a\sigma}{2a_0L_{mem} + 2a_2\eta^2L_{mem}^3/3 + 2L_{mem} + 2bL_{mem}/a - 4bC_0/a\sigma} \tag{3.25}$$

The system of two equations (3.19) and (3.25) is solved numerically to find constants b and d. Figure 3.4 shows reasonable agreement between the analytical solution and the numerical solution for large times found in the previous section. The analytical solution presented here was compared with the one in Andersen & Bruus (2012) and the latter gave a more accurate agreement with the transient numerical solution.

3.4. Summary of research

We analysed a system with an anion exchange membrane, two reservoirs and a monovalent electrolyte. We first presented the classical Guoy-Chapman equilibrium theory and derived Levich's expression for the limiting current. We then solved the system numerically for the underlimiting and the overlimiting current regimes to compare with previous results by Manzanares *et al.* (1993). Similarly to their work, we found that the electroneutrality assumption is not valid at the depletion side of the membrane and a space charge region forms to allow the passage of current.

Next, we derived an analytical solution for the steady state in the underlimiting current regime: we assumed electroneutrality and this gave a solution that had reasonable agreement with the full numerical solution. Instead of using the Donnan potential as was done by Andersen & Bruus (2012), we evaluated the jumps at the membrane/reservoir interfaces and used an integral constraint for the matching conditions which is an alternative way of solving the system. We succeeded in finding an analytical solution that has good agreement with the numerical solution.

4. Water dissociation in a bipolar membrane

We analyse the bipolar membrane system and reproduce the numerical results by Conroy *et al.* (2012) in section §4.1. Sections §4.2 and §4.3 illustrate numerical solutions of modified versions of this problem.

Conroy *et al.* (2012) considered two membranes with charges Σ_1 $(x < 0)$ and Σ_2 $(x > 0)$ respectively, joined at $x = 0$ to form a bipolar membrane which is held in a bath with a symmetric electrolyte C_b^+, C_b^- such that their valencies are $z_+ = -z_- = 1$. Water of concentration C_a is also added to the system; when an electric field $\mathbf{E}$ is applied across the membrane, the water splits into positive and negative ions C_a^+ and C_a^-. The governing equations (2.1-2.4) take the following form:

$$\nabla P = -\frac{\mu}{\Pi}\mathbf{u} + \rho^e \mathbf{E} \tag{4.1}$$

$$\nabla \cdot \mathbf{u} = 0 \tag{4.2}$$

$$\rho^e = F(C_a^+ - C_a^- + C_b^+ - C_b^-) \tag{4.3}$$

$$n\frac{\partial C_a^\pm}{\partial t} + \mathbf{u} \cdot \nabla C_a^\pm = \omega_a^\pm k_B T \nabla \cdot \left(\pm \frac{e}{k_B T} C_a^\pm \nabla \phi + \nabla C_a^\pm \right) + (m_f C_a - m_r C_a^+ C_a^-) \tag{4.4}$$

$$n\frac{\partial C_b^\pm}{\partial t} + \mathbf{u} \cdot \nabla C_b^\pm = \omega_b^+ k_B T \nabla \cdot \left(\pm \frac{e}{k_B T} C_b^\pm \nabla \phi + \nabla C_b^\pm \right) \tag{4.5}$$

$$\epsilon_0 \epsilon \nabla^2 \phi = \rho^e - F(\Sigma_1 H(-x) + \Sigma_2 H(x)) \tag{4.6}$$

The last term in eq. (4.4) is the reaction term where m_f and m_r are the dissociation and association rates of water ions: m_r is a constant while m_f is a linearised Arrhenius

term that depends on the electric field according to the second Wien effect theory: $m_f = k_a(1 + \epsilon_r(e/k_B T)|\phi_x|)$, with constants k_a and ϵ_r.
The above equations are non dimensionalised, the membrane is assumed to be long and thin and hydrodynamic effects are ignored as in chapter §2.2. ϕ' is the perturbation potential such that $\phi = \phi' + \beta(t)x$, with $\beta(t)$ the applied electric field.

$$\frac{\partial^2 \phi'}{\partial x^2} = -\chi^2(C_a^+ - C_a^- + C_b^+ - C_b^- + \Sigma_1 H(-x) + \Sigma_2 H(x)) \tag{4.7}$$

$$\frac{\partial C_a^\pm}{\partial t} = \alpha_a^\pm \frac{\partial}{\partial x}\left(\pm\psi C_a^\pm \left(\frac{\partial \phi'}{\partial x} + \beta(t)\right) + \frac{\partial C_a^\pm}{\partial x}\right) + DaR_0 \tag{4.8}$$

$$\frac{\partial C_b^\pm}{\partial t} = \alpha_b^\pm \frac{\partial}{\partial x}\left(\pm\psi C_b^\pm \left(\frac{\partial \phi'}{\partial x} + \beta(t)\right) + \frac{\partial C_b^\pm}{\partial x}\right) \tag{4.9}$$

The reaction term is given by:

$$R_0 = mK_0 - C_a^+ C_a^- = m\left(\epsilon\psi|\phi'_x + \beta| + 1\right) - C_a^+ C_a^- \tag{4.10}$$

where m is a constant related to the initial concentration of water ions when they are set to the equilibrium value.
The boundary conditions are $\partial C_{a,b}^\pm/\partial x(\pm L, t) = 0$ and $\phi(\pm L, t) = \pm\beta$, where L is the half length of the domain in the x direction.
The initial conditions are $C_a^\pm = \sqrt{m}$, $C_b^+ = |\Sigma_1|H(-x)$ and $C_b^- = |\Sigma_2|H(x)$, so that the salt maintains electroneutrality with the membrane.
Ion fluxes are defined as $J_{a,b}^\pm/\alpha_{a,b}^\pm = \pm\psi C_{a,b}^\pm\,(\phi'_x + \beta(t)) + \partial C_{a,b}^\pm/\partial x$ to express the current $I = -(J_a^+ - J_a^- + J_b^+ - J_b^-)$.

4.1. Water and one salt

In this section we repeat the numerical analysis in Conroy *et al.* (2012). In the experiments by Cheng & Chang (2011) the electric field depends on time and it is first increased and then decreased. In order to model this, the applied electric potential is given by a ramp function that depends on time:

$$\beta(t) = \begin{cases} 2t/t_{fin}, & \text{for } 0 \leq t \leq t_{fin}/2 \\ 2(1 - 1/t_{fin}), & \text{for } t_{fin}/2 < t \leq t_{fin} \end{cases}$$

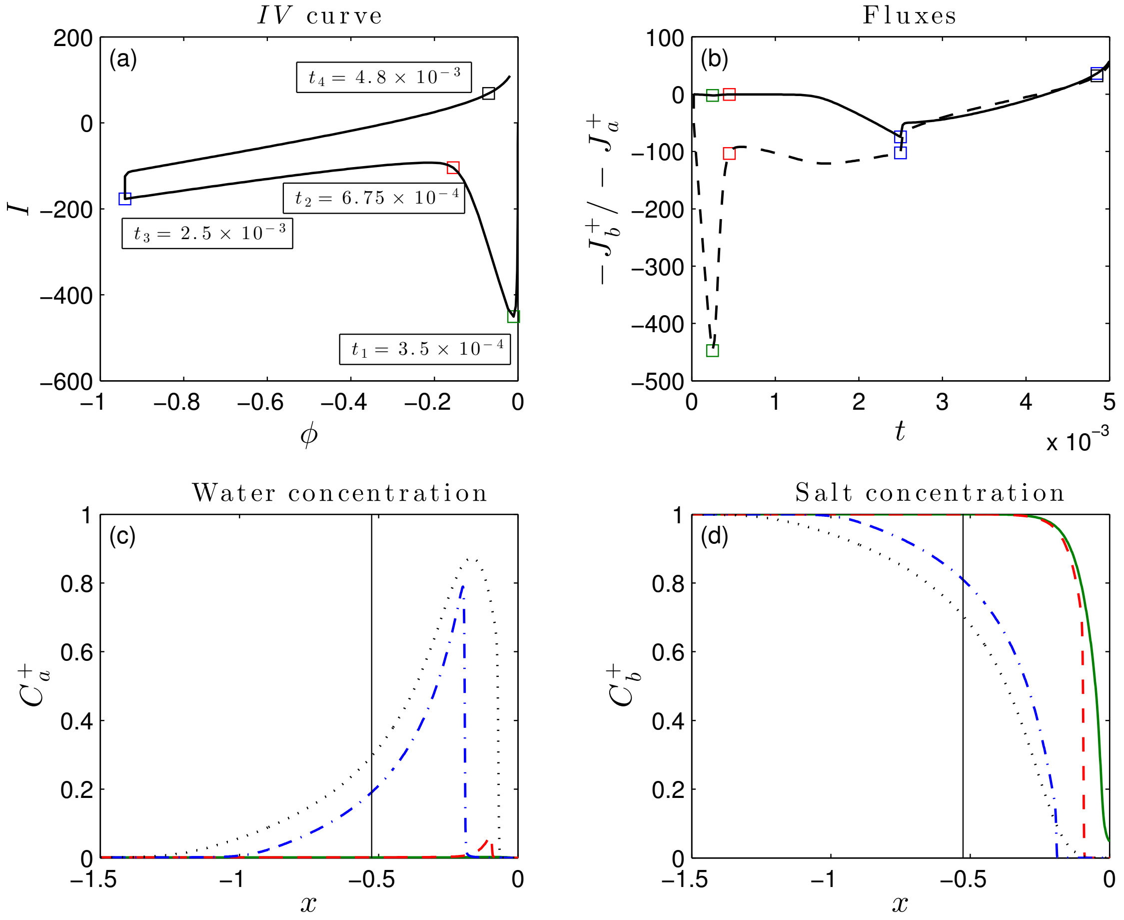

Figure 4.1. Top panels: current against potential and ion fluxes $-J_b^+$ (dashed line) and $-J_a^+$ (solid line) against time at measuring point $x = -0.5255$. Bottom panels: salt and water ion concentrations in the left membrane at times t_1 (solid line), t_2 (dashed line), t_3 (dash-dot line) and t_4 (dotted line). The vertical solid line corresponds to the measuring point $x = -0.5255$. Final time $t_{fin} = 5 \times 10^{-3}$, $\alpha_a^+ = 3$, $\alpha_a^- = 2$, $\alpha_b^{\pm} = 1$, $m = 10^{-6}$, $\psi = 5 \times 10^3$, $Da = 1 \times 10^6$, $\epsilon = 1 \times 10^{-2}$, $\chi = 10$.

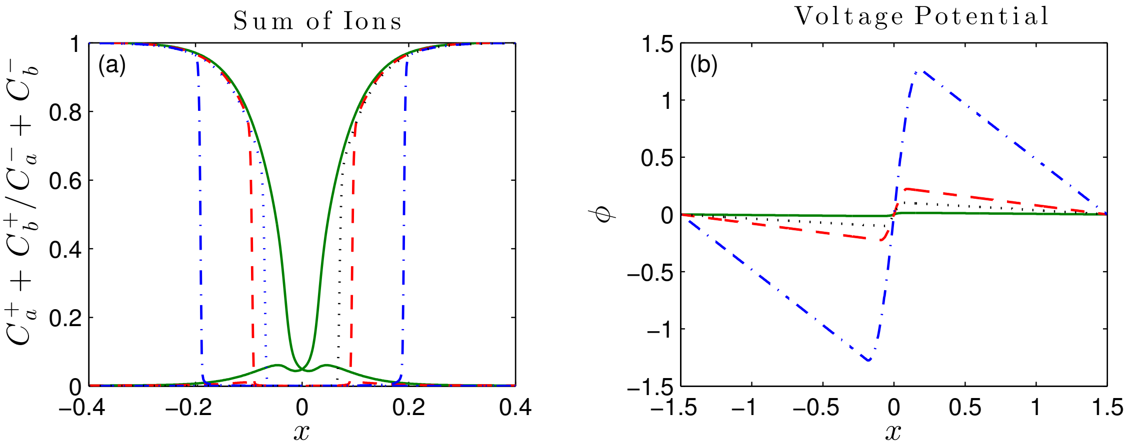

Figure 4.2. (a) Sum of salt and water ion concentrations close to the junction and (b) voltage potential at times t_1 (solid line), t_2 (dashed line), t_3 (dash-dot line), t_4 (dotted line).

Figure 4.1 shows the solution for the salt and water ion concentrations in the left membrane at four different times, the IV curve (a plot of the current versus potential) and the ionic fluxes. We clearly see the hysteresis of the IV curve in figure 4.1a where voltage and current are measured at $x = -0.5255$ (the measuring point is emphasised by the vertical solid line in figures 4.1c,d): as the voltage is swept from zero to negative values, the current intensity increases linearly until time t_1 when it starts dropping and then at time t_2 the current intensity starts increasing again; at time t_3 the applied electric field $\beta(t)$ starts decreasing and so does the current intensity but without following the same path as for increasing $\beta(t)$.
Figures 4.1b,c give the water and salt positive ion concentrations C_a^+ and C_b^+ at times $t_1 = 3.5 \times 10^{-4}$, $t_2 = 6.75 \times 10^{-4}$, $t_3 = 2.5 \times 10^{-3}$ and $t_4 = 4.8 \times 10^{-3}$ to highlight how the various ion fluxes contribute to the current I. As the electric field is switched on, the salt ions start moving away from the junction. At first, they are sufficiently close and the current is mainly due to $\beta(t)$. At time t_1 the ion depletion region at the junction is large enough to increase the potential difference ϕ' which starts dissociating water at t_2. The concentration of positive water ions C_a^+ increases in the left membrane as it tries to replace the positive salt ions in order to maintain electroneutrality with the membrane. When $\beta(t)$ is reversed at t_3 the ion depletion region and thus the voltage potential difference shrink. As $\beta(t)$ is decreased to zero, a depletion region is still present so ϕ_x' does not go to zero at t_{fin} and the IV curve does not follow the same path when $\beta(t)$ is reversed.

Previously Conroy *et al.* (2012) thought that when $\beta(t)$ is reversed the salt has already been swept away from the measuring point and that the current is only due to the water ions. From figure 4.1d we see that at t_3 both the positive salt and positive water ions are at the measuring point. Hence, the current I at a measuring point in the left membrane is given by both the positive ion fluxes J_a^+ and J_b^+ (figure 4.1b).Figure 4.2 shows the sum of the ions in both membrane and the voltage ϕ at the corresponding times. This is to highlight the formation of the depletion region and how it increases the potential drop across that region.

We have successfully repeated the numerical analysis presented in Conroy *et al.* (2012) and have gained a deeper understanding of the physical mechanisms responsible for the hysteresis of the IV curve. In the next sections we build upon this analysis to investigate the system further.

4.2. Two salts

In this section new results are presented: the behaviour of the system with two salts is analysed numerically. The aim was to find an IV curve with two minima instead of one, with each minimum corresponding to a salt being washed out of the system. This was based on the incorrect assumption that the minimum in the IV curve corresponds to the salt being flushed past the measuring point. It turns out that in the two salts case the IV curve is qualitatively the same as in the one salt case. This is due to the fact that the minimum in the IV curve happens at the time when the ion depletion region is wide enough to increase the potential drop ϕ' across the junction and not when the salt has gone past the measuring point.

In this case, eq. (4.7) becomes:

$$\frac{\partial^2 \phi'}{\partial x^2} = -\chi^2 (C_a^+ - C_a^- + C_b^+ - C_b^- + C_c^+ - C_c^- + \Sigma) \tag{4.11}$$

where $C_c^\pm$ are the positive and negative ions of the additional salt. The Nerst-Planck equations for the additional salt are as follows:

$$\frac{\partial C_c^\pm}{\partial t} = \alpha_c^\pm \frac{\partial}{\partial x} \left(\pm \psi C_c^\pm \left(\frac{\partial \phi'}{\partial x} + \beta(t) \right) + \frac{\partial C_c^\pm}{\partial x} \right) \tag{4.12}$$

The boundary conditions are the same as for the one salt case with the addition of $\partial C_c^\pm / \partial x(\pm L, t) = 0$. The initial conditions are:

$$C_b^+ = |\Sigma_b^+| H(-x)$$

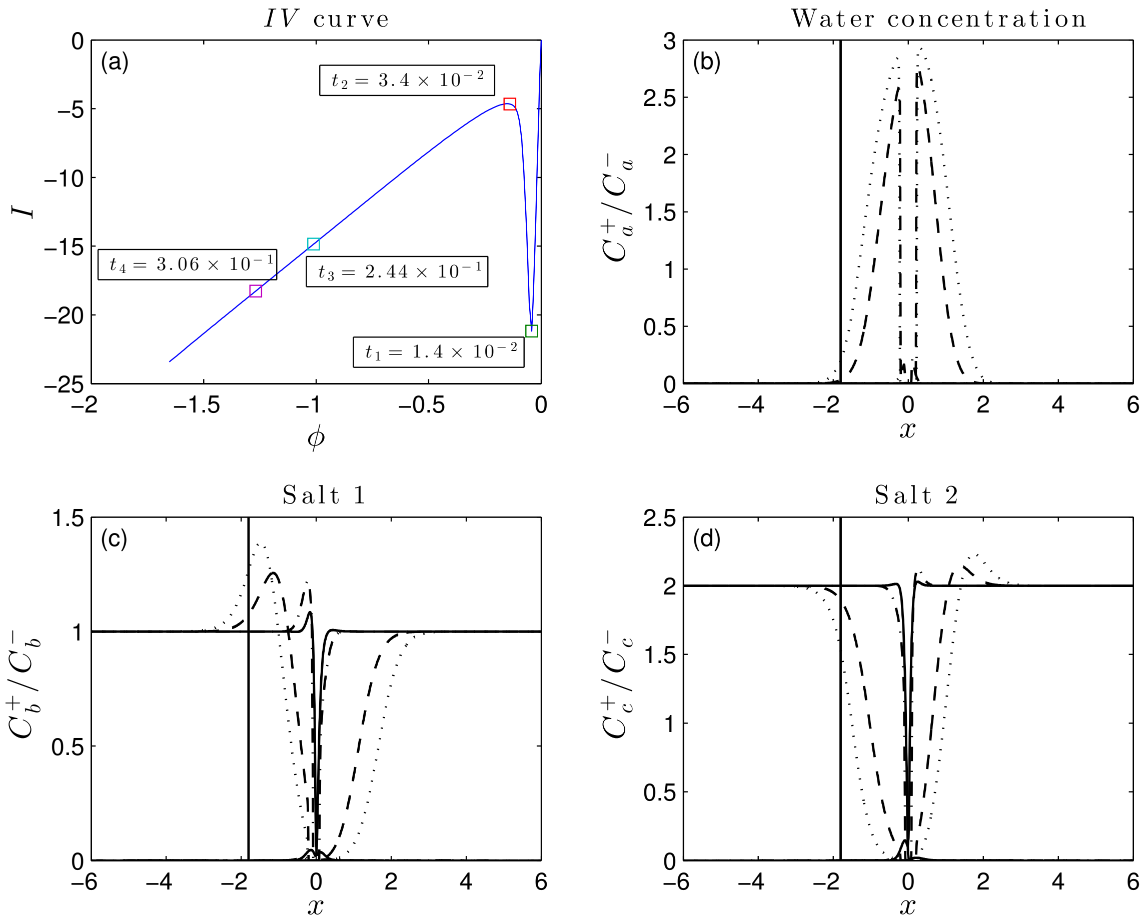

Figure 4.3. Top left panel: current against voltage at measuring point $x = -1.8021$. The other three panels show ion concentrations at times t_1 (solid line), t_2 (dashed line), t_3 (dash-dot line) and t_4 (dotted line). The vertical line corresponds to the measuring point $x = -1.8021$. Applied electric potential $\beta(t) = t$, $\alpha_a^+ = 1$, $\alpha_a^- = 0.5$, $\alpha_b^\pm = 1$, $\alpha_c^+ = 5$, $\alpha_c^- = 0.5$, $m = 10^{-6}$, $\psi = 5 \times 10^2$, $Da = 1 \times 10^5$, $\epsilon = 1 \times 10^{-1}$, $\chi = 5$.

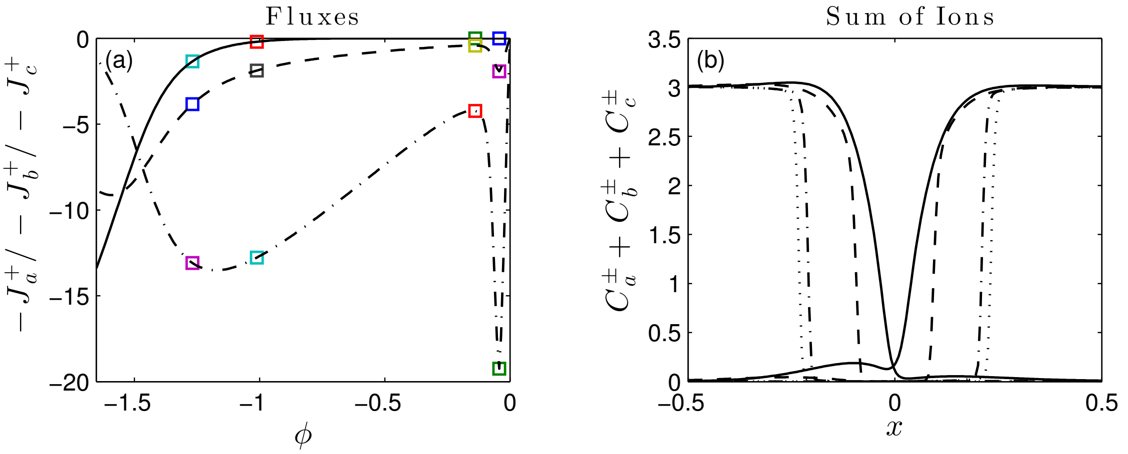

Figure 4.4. Left panel: ion fluxes $-J_b^+$ (dashed line), $-J_a^+$ (solid line) and $-J_c^+$ (dot-dashed line) against potential at measuring point $x = -1.8021$. Right panel: sum of salt 1, salt 2 and water ion concentrations close to the junction at times t_1 (solid line), t_2 (dashed line), t_3 (dash-dot line) and t_4 (dotted line). As before, the vertical line corresponds to the measuring point $x = -1.8021$. Same parameters as figure 4.3.

$$C_b^- = |\Sigma_b^-| H(x)$$

$$C_c^+ = |\Sigma_c^+| H(-x)$$

$$C_c^- = |\Sigma_c^-| H(x)$$

with $|\Sigma_b^+| + |\Sigma_c^+| = |\Sigma_1|$ and $|\Sigma_b^-| + |\Sigma_c^-| = |\Sigma_2|$ for electro-neutrality.
The current is given by $I = -(J_a^+ - J_a^- + J_b^+ - J_b^- + J_c^+ - J_c^-)$.
Figures 4.3 and 4.4 illustrate the behaviour of the system for $|\Sigma_b^\pm| = 1$ and $|\Sigma_c^\pm| = 2$ so $|\Sigma_{1,2}| = 3$ with mobilities $\alpha_a^+ = 1$, $\alpha_a^- = 0.5$, $\alpha_b^\pm = 1$, $\alpha_c^+ = 5$ and $\alpha_c^- = 0.5$. Initially, the ions of both salts are in equilibrium with the surface charges of the membrane as in §4.1. As the applied potential $\beta(t)$ is switched on, the ions start moving away from the junction. Since the mobility of salt ion C_c^+ is five times higher than the mobility of salt ion C_b^+, the former propagates away from the junction faster than the latter. However, the salt ion C_b^+ tries to preserve electroneutrality with the membrane, which is why it develops peaks (figure 4.3c). At the same time, the ion depletion region at the junction grows bigger which causes the water to split. Both positive salt ions and the positive water ion try to balance the membrane surface charges (figure 4.4b).
The current I at measuring point $x = -1.8021$ is given by the fluxes $-J_a^+$, $-J_b^+$ and $-J_c^+$. The sum of these fluxes gives a linear increase in the current intensity from time

t_2 to t_{fin} in a similar way to the case with just one salt in §4.1. Unfortunately the IV curve gives no indication of when the various salts are swept past the measuring point as previously hoped.

4.3. Reaction term

Onsager (1934) established that the dissociation rate for weak electrolytes depends on the applied electric field intensity - this phenomenon is referred to in the literature as the second Wien effect. In the case of bipolar membranes the dissociation rate can be modelled by the Arrhenius dependence given in (1.1) with the activation energy E_a given by the applied electric field intensity (Mafe & Ramirez, 1997). Conroy *et al.* (2012) use a linearised Arrhenius term (4.10). The aim of this section is to investigate the consequences of including a nonlinear Arrhenius term in the model:

$$R_{exp} = mK_{exp} - C_a^+ C_a^- = m \exp(\epsilon\psi|\phi_x' + \beta|) - C_a^+ C_a^- \tag{4.13}$$

K_{exp} can be approximated by K_0 for $\epsilon = 10^{-4}$ since $K_{exp} = K_0 + O(10^{-1})$ in this case. For this value of ϵ the IV curve does not have a current spike because the Wien effect is too weak.

When $\epsilon = 10^{-3}$ for K_{exp} and $\epsilon = 10^{-1}$ for K_0, $\max_{x\in(-L,L)} K_{exp}$ and $\max_{x\in(-L,L)} K_0$ are of the same order of magnitude. A plot comparing the solutions for these two cases is shown in fig. 4.5. We see that salt and water ions propagate to approximately the same distance for the two solutions but the IV curve has a different behaviour in each case.

This result is interesting as the experimentally measured IV curve is nonlinear (fig.1.7) which suggests that the dissociation rate in the model should indeed depend exponentially on the electric field intensity.

4.4. Summary of research

We analysed a system with a bipolar membrane, water and a salt under the effect of an electric field. We first considered the system where only one salt is present and reproduced the results by Conroy *et al.* (2012). As before, we found the IV curve to have a hysteretic behaviour. The initial spike in the current intensity is due to the applied electric field, its subsequent decrease is due to the appearance of a depletion region at the junction. As the salt ions move away from the junction they are replaced by the dissociating water ions in an attempt to maintain electroneutrality. As the applied

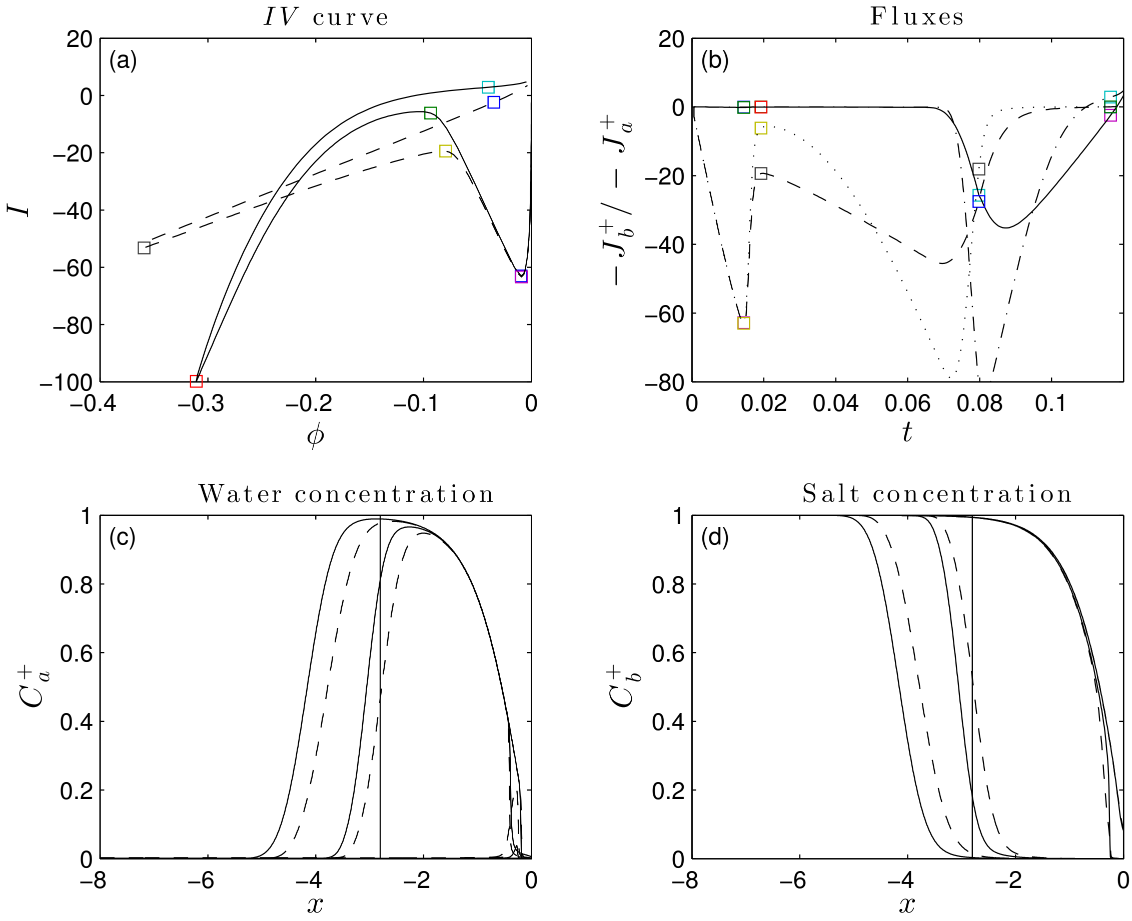

Figure 4.5. Comparison between solutions when reaction term is of the form R_0 (dashed line) and R_{exp} (solid line). $\epsilon = 10^{-1}$ for the case with R_0 and $\epsilon = 10^{-3}$ for the case with R_{exp}. Top panels: IV curve and positive ion fluxes evaluated at point $x = -2.8026$. Figure (b): $-J_a^+$ (R_0 - solid line, R_{exp} - dash-dot line), $-J_b^+$ (R_0 - dashed line, R_{exp} - dotted line). Bottom panels: salt and water ions concentrations evaluated at times $t_1 = 1.44 \times 10^{-2}$, $t_2 = 1.92 \times 10^{-2}$, $t_3 = 7.98 \times 10^{-2}$ and $t_4 = 1.1164 \times 10^{-1}$. Applied electric potential $\beta(t) = t \;\; (0 \leq t \leq 2t_f/3), \quad \beta(t) = 2(t_f - t) \;\; (2t_f/3 < t \leq t_f)$ with $t_f = 0.12$. $\alpha_a^+ = 1$, $\alpha_a^- = 0.5$, $\alpha_b^\pm = 1$, $m = 10^{-6}$, $\psi = 5 \times 10^3$, $Da = 1 \times 10^5$.

electric field is decreased so is the depletion junction which is still present even when the electric field has dropped to zero. Contrary to what was thought before, the initial spike in the current does not correspond to the salt being swept past the measuring point.

We looked at the behaviour of this same system with the presence of an extra salt and found the qualitative behaviour of the IV curve unchanged. This is because when the salt ions with the higher mobility are swept away from the junction, the second salt ions and the water ions move in its place to balance the membrane and preserve electroneutrality.

Finally we considered a non linearised Arrhenius term in the model and the numerically calculated IV curve exhibited a nonlinear behaviour that was similar to the IV curve found experimentally.

5. Concluding remarks

We have presented a mathematical model for the ionic transport through a porous membrane under the effects of an electric field. We assumed the length of the system to be much larger than the depth and hence derived a one dimensional model. The Peclet number which represents the ratio between convection and diffusion of ions is taken to be small which allows us to ignore hydrodynamic effects. The resulting system of equations is solved numerically using PDECOL, a FORTRAN PDE solver that relies on a finite element scheme for spatial discretisation and a routine based on Gear's method for the time integration.

We have analysed the behaviour of a binary monovalent electrolyte placed in a system made up of an anion membrane and two reservoirs. We compute the full time dependant solution and find that at large times the profiles of the salt concentrations and of the voltage potential reach a steady state. In the underlimiting current regime both the ion concentrations and the voltage potential vary almost linearly in the three regions. We assume electroneutrality in the reservoirs and derive an analytical solution for the system which is in excellent agreement with the full numerical solution at large times. In the overlimiting current regime our numerical solution confirms the existence of the space charge region that forms at the anodic side of the membrane.

We proceed to analyse the system in which an anion and a cation membranes are joined together to form a p-n junction and are held in an electrolyte bath with water and a salt. We compute the full numerical solution and reproduce the results found by Conroy *et al.* (2012). The IV curve has the same hysteretic behaviour as the one found in experiments by Cheng & Chang (2011) and we show that the initial dip in the current is due to the applied electric field rather than to the salt being swept past the measuring point as was previously thought.

We then presented original results in which we investigated the behaviour of the system with the addition of a second salt of higher mobility. Its ions appear to be swept away from the junction faster, with the first salt and the water ions moving in its place to balance the charge of the membrane and preserve electroneutrality. This leads to an IV curve with the same qualitative behaviour as in the one salt case.

Finally we considered a non linearised Arrhenius dependence to express the reaction term which led to a nonlinear behaviour of the IV curve. This curve was qualitatively more similar to the IV curve found experimentally than the one found by Conroy *et al.* (2012). This similarity is encouraging and suggests that nonlinear phenomena play an important role and that using the full nonlinear Arrhenius term leads to a more accurate description of the system.

Part II.

Interfacial flows under the effects of electric fields

6. Introduction

Thin liquid films appear in a wide variety of scenarios ranging from large scale geophysical flows, such as gravity driven currents (Huppert, 2006), to small scale microfluidic devices, such as lab-on-chip technology (Toner & Irimia, 2005). These flows are encountered in physical systems like lava flows (Balmforth & Craster, 2000) and ice sheets (Baral *et al.*, 2001) and are also relevant in biological systems, such as in the study of liquid linings of pulmonary airways (Grotberg, 1994). The understanding of the dynamics of thin film flows is of crucial importance for many industrial applications such as polymer patterning at the micro and nano scale (Nie & Kumacheva, 2008), nanofluidic technology (Eijkel & Berg, 2005) and lab-on-chip devices that are able to perform specific blood analyses using small samples of fluid (SooHoo & Walker, 2009). The applications and main features of thin film flows are summarised in the review by Craster & Matar (2009).

In this part of the thesis, we consider thin film flows under the effect of electric forces. These can destabilise the free surface, in the case of a single fluid, or the fluid-fluid interface, in the case of two fluids, and lead to rupture of the film or to the creation of interesting patterns. The fluids can be perfect dielectrics, where no free charge is present or leaky dielectrics, where the charge accumulates at the interface to ensure current conservation when there is a jump in conductivities. The fluid motion of film flows under the effect of electric fields is governed by the Navier-Stokes equations and when the fluid is a leaky dielectric we need to include an equation for the conservation of current based on Ohmic conductivity. Magnetic effects are ignored since under static conditions magnetic and electric fields are independent of each other (Feynman *et al.*, 1979). The coupling between the electric field and the fluid flow only occurs at the interface where there is a discontinuity in electric permittivities and conductivities. When the fluids are perfect dielectrics the electric stress is balanced by a combination of interfacial tension and the changes of interfacial shape. For leaky dielectrics the interfacial conditions are different: the free charge at the surface modifies the electric field and viscous stresses balance the tangential components of the field that act on the charge. Such a treatment of electrohydrodynamics first emerged in a review by Melcher & Taylor (1969). One of the earliest works that deals with such systems by Melcher & Smith (1969) investigated

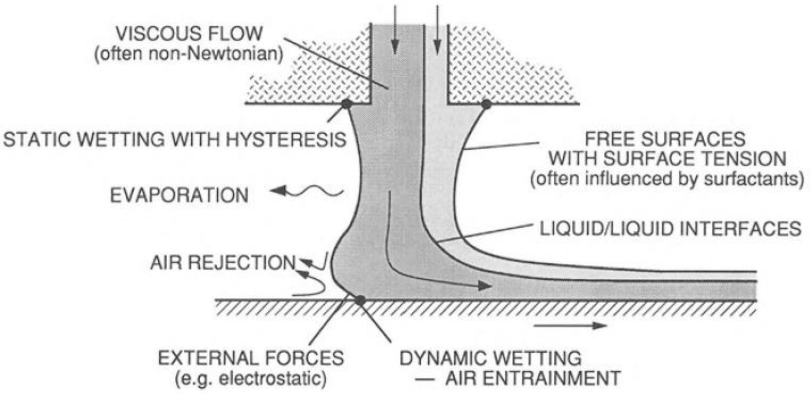

Figure 6.1. Schematic of a liquid film coating process and the physical mechanisms involved. Figure taken from Schweizer & Kistler (2012).

the behaviour of a plane interface between two fluids stressed by initially perpendicular electric fields which led to the conclusion that the presence of even a small amount of surface charge brings down the value of the critical voltage required for instability compared to the case with no surface charge. Saville (1997) summarised the model proposed by Melcher & Taylor (1969) and gave a review on the effects of electric fields on interfacial dynamics for fluid drops, cylinders and suspensions.

The following chapters are aimed at analysing the behaviour of the free surface of an electrified fluid sheet under the influence of a tangential electric field (§8) and the effect of a transverse electric field on the interface between two fluids in a channel (§9 & §10). In the next two sections we give an overview on previous work on these two problems.

6.1. Effects of a tangential electric field on a fluid sheet

Free liquid films arise in a variety of physical situations and industrial applications. One of the central phenomena in thin film dynamics is the rupturing process which occurs in many colloid systems such as coalescence of emulsions (Kumar *et al.*, 2002; Marrucci, 1969), biological membranes (Knutton, 1979) and soap films (Sheludko, 1967). In industrial systems rupture occurs in atomisation by film formation (Lefebvre, 1988) and coating processes (Ramkrishnan & Kumar, 2013; Schweizer & Kistler, 2012; Weinstein & Ruschak, 2004). To achieve the latter, it is important to maintain the thin film at a constant thickness and to prevent rupture in order to deposit a uniform liquid layer on the surface that needs to be coated (see Figure 6.1 for a schematic of a hypothetical coating process). Erneux & Davis (1993) investigated the nonlinear stability to symmetric disturbances of a free film using a one dimensional long-wave model and found that van der Waals forces are necessary for rupture. Vaynblat *et al.* (2001) extended the problem to two dimensions and found similarity solutions for a line rupture and a point rupture. This problem was further extended to three dimensions by Miksis & Ida (1998*a*,*b*).

The introduction of a tangential electric field has interesting effects on the behaviour of free surfaces of thin films such as the suppression of instability and the increase in speed of capillary waves (Melcher & Schwarz, 1968). There have been several studies on this topic, in particular Tilley *et al.* (2001) considered a non-conducting, inviscid fluid sheet and found that the electric field delays rupture but does not prevent it. They derived nonlinear long wave evolution equations with the electric field entering as a non-local term and constructed travelling waves. Savettaseranee *et al.* (2003) considered the same problem but for a viscous fluid and with the inclusion of van der Waals forces. Rupturing solutions were found to be surface tension dominated with similarity scalings consistent with Vaynblat *et al.* (2001). Papageorgiou & Vanden-Broeck (2004*b*) constructed symmetric travelling waves for the same system as the one analysed by Tilley *et al.* (2001) and recovered their results in the long wave limit. The full model derived by Papageorgiou & Vanden-Broeck (2004*b*) however made no assumptions regarding the size of wave amplitudes and lengths. They found that a tangential electric field smoothes out otherwise steep waves and for certain values of relative electric permittivity stronger electric fields lead to an increase in wave speed. Similar results were found for the case of antisymmetric waves (Papageorgiou & Vanden-Broeck, 2004*a*). The studies by Zubarev (2004); Zubarev & Kochurin (2013); Zubarev & Zubareva (2010) also considered interfacial waves using analytical tools and found that waves of small but finite amplitude can propagate without shape distortion along the interface between two non-conducting fluids in the direction of the electric field.

Papageorgiou & Petropoulos (2004) considered a model similar to the one analysed by Savettaseranee *et al.* (2003) but ignored van der Waals forces and instead looked at the effect of including a surface charge. They established through a linear analysis that the effect of the electric field is no longer stabilising when the liquid sheet has finite conductivity. These results were confirmed by the work of Ozen *et al.* (2006) in which numerical simulations show that the sheet structure is that of drops connected by long thinning necks and that rupture is possible at asymptotically large times. Both Papageorgiou & Petropoulos (2004) and Ozen *et al.* (2006) made the assumption of fast charge relaxation times which led to a simplification of the charge equation.

Grandison *et al.* (2007) extended the work by (Papageorgiou & Vanden-Broeck, 2004*a*,*b*) by considering the dynamics of a fluid sheet surrounded by a second fluid. In the limit where the second fluid has zero density they recovered the results in Papageorgiou & Vanden-Broeck (2004*a*,*b*). Through linear theory they found that the surrounding fluid reduces the steepness of both symmetric and antisymmetric nonlinear waves and can act to stabilise the KelvinHelmholtz instability even in the absence of surface tension. There are several more studies that consider the interface between two fluids under the effects of a tangential electric field and this is used to suppress the Rayleigh-Taylor instability (see Barannyk *et al.* (2012) for a nonlinear study and Cimpeanu *et al.* (2014) for a direct numerical simulation). A related study by Hunt *et al.* (2014) considers a film hanging from a dielectric slab and shows that the electric field is able to suppress the gravitational instability. This agrees with the study by Barannyk *et al.* (2015*b*) which considers the same problem as in Barannyk *et al.* (2012) but also analyses the wall touch-up that occurs when the electric field is weak or absent for which a similarity solution of the second kind is found. Liu *et al.* (2016) conducted a linear stability analysis for the behaviour of a viscous electrified sheet surrounded by compressible gas streams under the effect of a transverse electric field; they found that an electrified sheet is more unstable than a non electrified one.

In the present study we consider a system similar to the one examined by Ozen *et al.* (2006) and take the ratio of fluid to electric time scales to be of $O(1)$ and nonlinear coupled evolution equations are derived for the thickness of the sheet, the horizontal fluid velocity and the surface charge. We find that without the assumption of fast charge relaxation times the interface can rupture at finite times.

6.2. Effects of a transverse electric field on the interface between two fluids

Multilayer flows under the effect of electric fields have a huge range of applications such as in micro engineering and point of care diagnostics technology (see Gubala *et al.* (2011) and Figure 6.2). In recent years there has been growing interest in the miniaturisation of electronic tools and much research has gone into finding appropriate techniques to pattern polymers. Details on the applications and techniques of polymer patterning can be found in the review by Nie & Kumacheva (2008). One such technique exploits the electrohydrodynamic instabilities of a system to induce ordered patterns and it was first explored in two experimental papers contemporary to each other (see Chou & Zhuang (1999); Schaffer *et al.* (2000) and Figure 6.3). Since then, electrohydrodynamic instabil-

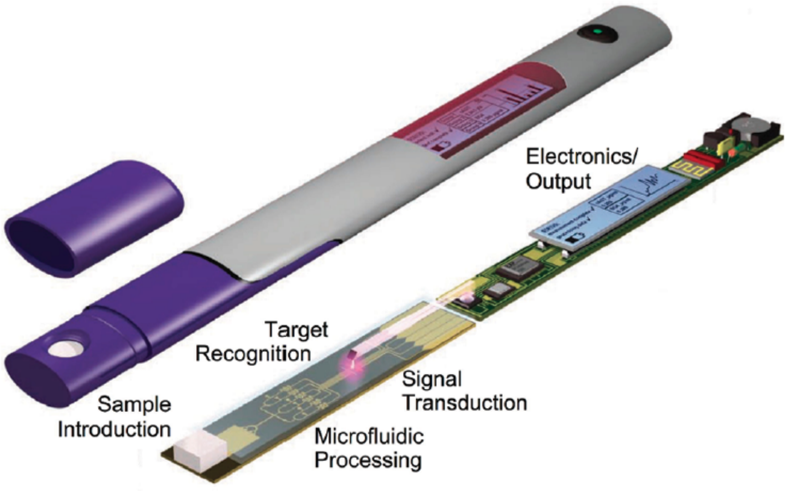

Figure 6.2. Schematic of an idealised point of care diagnostics device. Figure taken from Gubala *et al.* (2011).

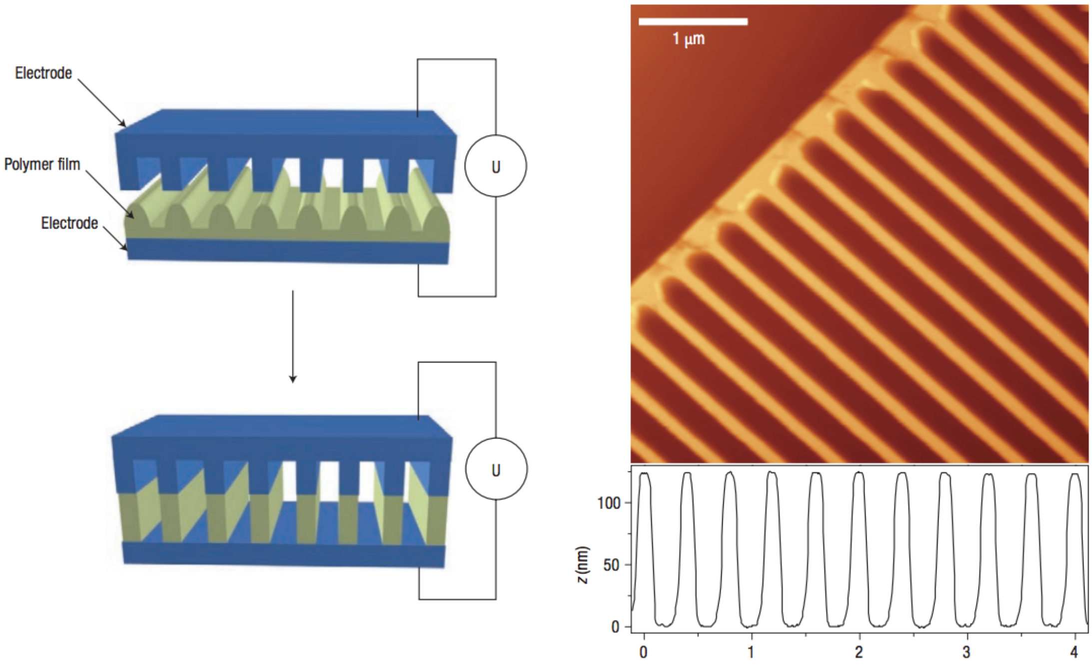

Figure 6.3. Schematic representation of electrically induced pattern transfer and an image of the topographic pattern produced. Figure taken from Schaffer *et al.* (2000).

ity induced structures have been the focus of much research due to the simplicity and the low cost of this patterning method, details of which can be found in the review by Wu & Russell (2009). Linear stability analyses have been conducted using both the perfect dielectric (Schaffer *et al.*, 2001) and the leaky dielectric (Pease & Russell, 2002) models. Both predict experimental data reasonably well, with the leaky dielectric decreasing pillar spacing and increasing their rate of formation.

Linear stability analyses and full numerical simulations have been done for a variety of similar setups. Li *et al.* (2007) considered the linear stability of the interface between two conducting fluids bounded by two flat electrodes and found that the electric field has a destabilising effect for perfect dielectrics and either a stabilising or destabilising effect for leaky dielectrics with either Couette or Poiseuille base flows. Craster & Matar (2005) conducted full numerical simulations for an equivalent system with no base flow and showed that initially small perturbations developed into spatially periodic columnar structures. Maehlmann & Papageorgiou (2011) found that including a Couette type flow in such a system caused the interface to evolve into fingerlike structures that were driven away from the centre line due to the presence of background flow. In this study we combine these setups and look at a pressure driven two layer flow between one flat and one sinusoidal electrode.

There has been some recent work on flow of fluids over surface topography in a setup similar to the one in this thesis, mostly involving a fluid-air interface. Many previous studies considered gravity-driven flow of a single layer of fluid over topography (Tseluiko & Blyth, 2009; Tseluiko *et al.*, 2013, 2008*a*,*b*). Tseluiko *et al.* (2008*b*) looked at steady solutions for the gravity-driven flow of a single layer of electrified viscous fluid over steps, trenches and mounds and showed that the presence of an electric field can alter some of the interfacial features. Luo & Pozrikidis (2006) considered the interface between two viscous fluids flowing between one flat boundary and one with periodic steps for a gravity-driven flow and with a sinusoidal lower wall and found the interfacial features to be in phase with the topography. Pollak & Aksel (2013*b*) conducted an experimental study of the stability of gravity-driven flow over sinusoidal topography. They observed the formation of eddies and found values of the viscosity and Reynolds numbers that are necessary for the eddies to form. A similar experimental study was conducted by Schorner *et al.* (2015): they examined 5 different topographies and found that the linear stability of the system is unaffected by the shape of the lower boundary.

There are a few studies for flows over topography without an incline: Lenz & Kumar (2007) considered a geometry similar to the one analysed by Luo & Pozrikidis (2006) but with flow over a flat plane. They analysed the steady states of the system and found that the step causes the formation or a capillary ridge at the interface. Yang *et al.* (2013*a*,*b*) modelled the evolution of the fluid-air interface with a flat electrode on the bottom and a sinusoidally-patterned electrode on the top and found that the interface deformation is consistent with the shape of the wavy electrode. Ramkrishnan & Kumar (2014) investigated the fluid-air interface in the flow between a patterned and a flat electrode with both perfect and leaky dielectric materials considered. They found that in the case of a perfect dielectric a small amplitude sinusoidal pattern leads to an interface shape that mimics the electrode pattern. Karapetsas & Bontozoglou (2015) carried out 2D numerical calculations for a Newtonian fluid and a viscoelastic polymeric fluid under a patterned mask to find that perturbations grow until they reach the top electrode and viscoelasticity affects their wavelength.

In the present study, we consider pressure-driven two-layer flows through channels of variable cross-section that are additionally influenced by the presence of electric fields arising from imposing a constant voltage potential across the channel walls. Sufficiently strong electric fields can destabilise the flow and lead to nonlinear free surface patterns that can be useful in applications (e.g. micro-lithography). Our model closely follows the one described by Craster & Matar (2005) but with the addition of a constant flow rate and corrugated boundaries. Such a setup is motivated by applications in bioanalytical devices, many of which introduce fluid into a reactor by using a pressure driven flow (Erickson & Li, 2004). We include electrode topography to explore the possibility for mixing and cell trapping which are key features of many microfluidic devices for cellomics (Yi *et al.*, 2006). The reader is referred to the two reviews by Khandurina & Guttman (2002) and Andersson & van den Berg (2003) for details on bioanalytical devices.

7. Mathematical formulation

7.1. Governing equations

In this chapter we give the mathematical formulation for the pressure driven flow of two films of viscous fluid that are sandwiched between two electrodes. The electrodes can be either flat and parallel to the undisturbed interface or corrugated with the shape of the bottom given by $z(x)$ and the top one by $\beta(x)$ (figure 7.1). The fluids are taken to be Newtonian and incompressible and the electric fields are governed by the electrostatic approximation of Maxwell's equations. Fluid 1 is placed in the region $0 \leq y \leq \beta(x)H$ and fluid 2 in $-z(x)H \leq y \leq 0$ with the undisturbed interface at $y = 0$. The electrodes are kept at a constant voltage $V_1 = 0$ at the top and $V_2 = \tilde{V}_b$ at the bottom. A leaky dielectric model (Saville, 1997) is considered: the charge $q(x,t)$ is accumulated on the interface $h(x,t)$ and the electric field only plays a role at the interface because the bulk is assumed to be electroneutral and conduction along the interface is neglected.

Here we give the general governing equations for fluid 1 (upper) and fluid 2 (lower), that have viscosities $\mu_{1,2}$, densities $\rho_{1,2}$, dielectric constants $\epsilon_{1,2}$ and conductivities $\sigma_{1,2}$. The velocity in fluid i is $\mathbf{u}_i = (u_i, v_i, 0)$ where u_i and v_i are the velocity components in the x and the y direction respectively; P_i is the pressure in fluid i and Q is the overall flow rate. Due to the small scale of the film thickness gravity can be neglected. For the present, we do not include intermolecular forces into the problem.

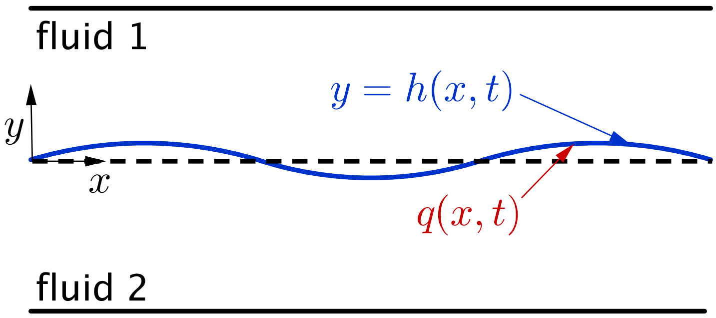

Figure 7.1. Setup of the system.

The fluid flow is governed by the Navier-Stokes equations and the continuity equation:

$$\rho_i(\mathbf{u}_{it} + \mathbf{u}_i \cdot \nabla \mathbf{u}_i) = -\nabla P_i + \mu_i \nabla^2 \mathbf{u}_i, \qquad i = 1, 2; \tag{7.1}$$

$$\nabla \cdot \mathbf{u}_i = 0, \qquad i = 1, 2. \tag{7.2}$$

The above equations are subject to interfacial conditions such as continuity of the fluid velocity at the interface:

$$[\mathbf{u} \cdot \mathbf{n}] = [\mathbf{u} \cdot \mathbf{t}] = 0, \tag{7.3}$$

where $\mathbf{n} = (-h_x, 1)/\sqrt{1 + h_x^2}$ is the outward pointing normal vector and $\mathbf{t} = (1, h_x)/\sqrt{1 + h_x^2}$ is the tangent vector. The stress tensor $\mathbf{T}$ has a fluid part $\mathbf{T}^{\mathbf{F}}$ and an electrical part $\mathbf{T}^{\mathbf{E}}$:

$$\mathbf{T} = \mathbf{T}^{\mathbf{F}} + \mathbf{T}^{\mathbf{E}}, \tag{7.4}$$

where

$$\mathbf{T}^{\mathbf{F}} = -p\mathbf{I} + \mu(\nabla \mathbf{u} + \nabla \mathbf{u}^T), \qquad \mathbf{T}^{\mathbf{E}} = \epsilon_i \left(\mathbf{E}\mathbf{E} - \frac{1}{2} |\mathbf{E}|^2 \mathbf{I} \right). \tag{7.5}$$

The jumps in the normal and tangential stresses are given by:

$$[\mathbf{n} \cdot \mathbf{T} \cdot \mathbf{n}] = \gamma \kappa, \qquad \left[\mathbf{t} \cdot \mathbf{T}^{\mathbf{F}} \cdot \mathbf{n}\right] = q\mathbf{E} \cdot \mathbf{t}, \tag{7.6}$$

where κ is the curvature and γ is the surface tension. The expression for the tangential stress balance follows from Gauss' law where q is the interfacial charge and $\mathbf{E}$ is the electric field. In addition, we have no slip and no penetration at both boundaries $y = -z(x)H$ and $y = \beta(x)H$.

The electric field $\mathbf{E}_i$ is irrotational, hence it can be expressed using a voltage potential which is governed by a Laplacian:

$$\nabla^2 V_i = 0, \tag{7.7}$$

where $\mathbf{E}_i = -\nabla V_i$. The voltage potential is continuous across the interface as is its tangential part. The jump in the normal direction is given by Gauss' law:

$$[V_i] = 0, \qquad [\mathbf{t} \cdot \mathbf{E}] = 0, \qquad [\epsilon \mathbf{E} \cdot \mathbf{n}] = -q. \tag{7.8}$$

The voltages are kept constant at the boundaries: $V_1 = 0$ at $y = \beta(x)H$ and $V_2 = \tilde{V}_b$ at $y = -z(x)H$.
The interfacial charge is governed by the following conservation equation:

$$q_t + \mathbf{u} \cdot \nabla q - q\mathbf{n} \cdot (\mathbf{n} \cdot \nabla)\mathbf{u} = -\sigma_1 \mathbf{E}_1 \cdot \mathbf{n} + \sigma_2 \mathbf{E}_2 \cdot \mathbf{n}. \tag{7.9}$$

To complete the system we need an overall flow rate condition and the kinematic condition:

$$\int_h^{\beta H} u_1 dy + \int_{-Hz}^{h} u_2 dy = Q, \qquad v_i = h_t + u_i h_x. \tag{7.10}$$

In the following sections this set of nonlinear equations plus boundary conditions is non-dimensionalised and asymptotic methods are used to derive and evolution equation for the interface location $h(x,t)$ and for the charge $q(x,t)$ when it is present. In section §7.2 focuses on the behaviour of the interface between a viscous electrified fluid and a conducting medium while section §7.3 analyses the interface between two fluids that flow between two electrodes.

7.2. Evolution equation for a single liquid sheet

In this section we derive the evolution equations for a viscous, conducting, liquid sheet surrounded by a conducting medium with an electric field $\mathbf{E}$ applied parallel to the undisturbed interfaces (figure 7.2). The sheet is symmetric about the x-axis and it is assumed that all perturbations are also symmetric so it is enough to consider the top half of the sheet.

7.2.1. Dimensionless equations

We take the governing equations from section §7.1 with the upper fluid 1 replaced by a conducting medium. Since there is no flow outside the layer of fluid, the subscripts in the fluid equations are dropped. The equations are non-dimensionalised using the following scales:

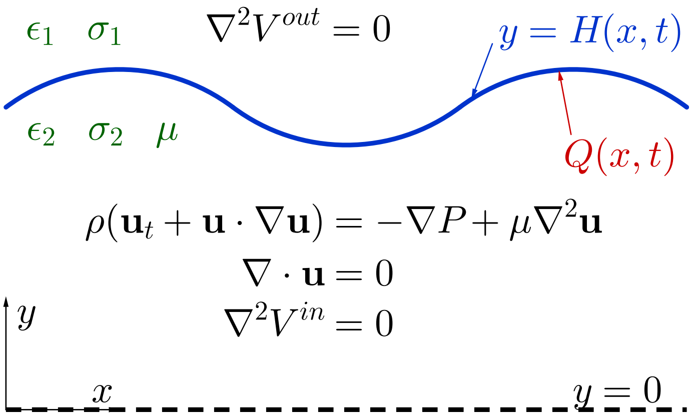

Figure 7.2. Setup of the system and governing equations.

$$\begin{aligned} x &= Lx', & y &= dy', & (u,v) &= U(u',\delta v'), & V &= V_b V', \\ h &= dh', & t &= \frac{L}{U}t', & P &= \rho U^2 P', & q &= \frac{\epsilon_1 V_0}{L} q', \end{aligned} \tag{7.11}$$

where $\delta = d/L \ll 1$ is a small parameter.

For simplicity all dashes are dropped and the non-dimensional equations take the following form:

$$u_t + uu_x + vu_y = - P_x + \frac{1}{\mathrm{Re}}\left(u_{xx} + \frac{1}{\delta^2}u_{yy}\right), \tag{7.12}$$

$$\delta^2(v_t + uv_x + vv_y) = - P_y + \frac{\delta^2}{\mathrm{Re}}\left(v_{xx} + \frac{1}{\delta^2}v_{yy}\right), \tag{7.13}$$

$$u_x + v_y = 0, \tag{7.14}$$

$$\delta^2 V_{ixx} + V_{iyy} = 0, \qquad i = 1, 2. \tag{7.15}$$

where Re is the Reynolds number. These equations are solved together with interfacial conditions such as the non-dimensional normal and tangential stress balances:

$$\begin{aligned} -p + \frac{2}{\mathrm{Re}(1+\delta^2 h_x^2)} \big(u_x(\delta^2 h_x^2 - 1) - h_x(u_y + \delta^2 v_x) \big) + \\ + \frac{\mathrm{E_b}}{1+\delta^2 h_x^2} \left[\epsilon_i \frac{1-\delta^2 h_x^2}{2} \left(\frac{V_y^2}{\delta^2} - V_x^2 \right) - 2h_x(\epsilon_i V_x V_y) \right] = \\ = \frac{\delta}{\mathrm{Re\ Ca}} \frac{h_{xx}}{(1+\delta^2 h_x^2)^{\frac{3}{2}}}, \end{aligned} \tag{7.16}$$

$$2\delta^2 h_x(v_y - u_x) + (1-\delta^2 h_x^2)(u_y + \delta^2 v_x) = \mathrm{Re\ E_b}\ \delta q(V_{2x} + V_{2y}h_x)\sqrt{1+\delta^2 h_x^2}, \tag{7.17}$$

and the kinematic condition and the symmetry conditions about $y = 0$:

$$v = h_t + uh_x, \qquad u_y(x,0,t) = v(x,0,t) = V_y(x,0,t) = 0. \tag{7.18}$$

The tangential component of the electric field is continuous and the jump in its normal component is given by Gauss' law:

$$[V_x + h_x V_y]_1^2 = 0. \tag{7.19}$$

$$\epsilon_p(\delta^2 h_x V_{2x} - V_{2y}) - (\delta^2 h_x V_{1x} - V_{1y}) = -\delta q\sqrt{1+\delta^2 h_x^2}. \tag{7.20}$$

The dimensionless charge conservation equation takes the following form:

$$\begin{aligned} q_t - \delta^2 \frac{h_t hx}{1+\delta^2 h_x^2} q_x + \frac{1}{\sqrt{1+\delta^2 h_x^2}} \left(\frac{u+\delta^2 v h_x}{\sqrt{1+\delta^2 h_x^2}} \right)_x q + \delta^2 h_{xx} \frac{v - uh_x}{(1+\delta^2 h_x^2)^2} q = \\ - \frac{T}{\sqrt{1+\delta^2 h_x^2}} \left[\frac{V_{2y}}{\delta} - \delta h_x V_{2x} - \sigma_R \left(\frac{V_{1y}}{\delta} - \delta h_x V_{1x} \right) \right]. \end{aligned} \tag{7.21}$$

We combine the expression for the tangential stress balance (7.17) and Gauss' law (7.20) to get:

$$\begin{aligned} 2\delta^2 h_x(v_y - u_x) + (1-\delta^2 h_x^2)(u_y + \delta^2 v_x) = \\ \mathrm{Re\ E_b}\ (V_{2x} + V_{2y}h_x)[\epsilon_p(\delta^2 h_x V_{2x} - V_{2y}) - (\delta^2 h_x V_{1x} - V_{1y}). \end{aligned} \tag{7.22}$$

The advantage of scaling is that seven non-dimensional parameters emerge:

$$\mathrm{Re} = \frac{\rho U L}{\mu}, \qquad \mathrm{Ca} = \frac{\mu U}{\gamma}, \qquad \mathrm{E_b} = \frac{V_b^2 \epsilon_1}{L^2 \rho U^2},$$

$$\epsilon_p = \frac{\epsilon_2}{\epsilon_1}, \qquad \sigma_R = \frac{\sigma_2}{\sigma_1}, \qquad T = \frac{L\sigma_1}{U\epsilon_1}, \qquad \delta = \frac{d}{L},$$

where Re is the Reynolds number, Ca is the capillary number, $\mathrm{E_b}$ is the electric Weber number which expresses the ratio of electric to capillary forces, ϵ_p and σ_R which give the ratios of electrical permittivities and conductivities respectively, T is the ratio of fluid to electric time scales and δ is the aspect ratio. We can explore the properties of the system in distinguished limits where different pieces of physics dominate.

7.2.2. Long-wave asymptotics

We assume that the wavelength of interfacial disturbances is long compared to the thickness of the sheet and we take the aspect ratio to be very small: $\delta \ll 1$. We introduce the following asymptotic expansions:

$$u = u_0 + \delta u_1 + \delta^2 u_2 + ...,$$

$$v = v_0 + \delta v_1 + \delta^2 v_2 + ...,$$

$$P = P_0 + \delta P_1 + ...,$$

$$h = H_0 + \delta H_1 + ...,$$

$$q = \delta q_1 + ...$$

Substituting these into the Navier-Stokes equations (7.12-7.14) and using symmetry conditions gives the vertical and horizontal fluid velocities to leading order:

$$u_0 = C(x,t), \qquad v_0 = -yC_x. \tag{7.23}$$

Similarly we can find u_1 and v_1 which are set to zero without loss of generality. Laplace's equation is solved for the voltage $V_{1,2}$ along with the symmetry condition.The voltage can be expressed as the sum of undisturbed plus disturbed part:

$$V_i = \frac{x}{2} + \delta \bar{V}_i$$

where the undisturbed part represents the applied electric field. We note that in the region where $y \sim \delta^{-1}$, we need to introduce an outer variable $Y = \delta y$ in order to solve equation (7.15) to find the voltage in the outer layer. The details are in the appendix and it is found that this outer solution is equal to zero and we do not have to worry about it.
Solving equation (7.15) in the inner layer where $y \sim 1$ gives:

$$V_1 = \frac{x}{2} + \delta V_{11}(x,t) + \delta^2 (A(x,t) + yB(x,t)) + O(\delta^3), \tag{7.24}$$

$$V_2 = \frac{x}{2} + \delta V_{21}(x,t) + \delta^2 V_{22}(x,t) + O(\delta^3). \tag{7.25}$$

$$\tag{7.26}$$

The continuity of tangential electric field (7.19) is used to match V_1 and V_2 at the boundary to get:

$$V_{21}(x,t) = V_{11}(x,t),$$

$$V_{22x} = A_x + yB_x + H_{0x}B, \quad \Rightarrow V_{22} = A + BH_0.$$

The charge conservation equation (7.21) at leading order becomes:

$$q_{1t} + C_x q_1 = T\left(\sigma_R B + \frac{H_{0x}}{2}(1-\sigma_R)\right), \tag{7.27}$$

and using Gauss' law (7.20) we find B:

$$B = \frac{1-\epsilon_p}{2} H_{0x} - q_1. \tag{7.28}$$

In order to include surface tension and electrical effects, the following scalings are considered:

$$\mathrm{E_b} \sim 1, \qquad \mathrm{Ca} = \Sigma/\delta.$$

Physically this means that viscous forces are large compared to capillary forces which are of the same order of magnitude as electrical stresses. If we take a different scaling for the electric Weber number the system is not affected by the electric field and this is the simplest scaling to include it.

At $O(1)$ the normal stress equation and the y-momentum equation take the form:

$$-P_0 - \frac{2}{\mathrm{Re}} C_x = \frac{\Sigma}{\mathrm{Re}} H_{0xx}, \qquad P_0 = P_0(x,t). \tag{7.29}$$

Equation (7.22) at order δ^2 gives:

$$-4H_{0x}C_x - yC_{xx} + u_{2y} = -\frac{\mathrm{Re}\,\mathrm{E_b}}{2} q_1. \tag{7.30}$$

Taking the x-momentum equation (7.12) at order δ^2 and then integrating in y gives:

$$u_{2y} = y\mathrm{Re}\left[C_t + CC_x + P_{0x}\right] - yC_{xx}. \tag{7.31}$$

Combining equations (7.29-7.31) and (7.27) and using the kinematic condition at $y = H_0$ we get three coupled evolution equations for $H_0(x,t)$, $C(x,t)$ and $q_1(x,t)$ (we drop the 0's and 1's for convenience):

$$H_t + (CH)_x = 0, \tag{7.32}$$

$$C_t + CC_x = \frac{\Sigma}{\mathrm{Re}} H_{xxx} + \frac{4}{\mathrm{Re}} \frac{(HC_x)_x}{H} - \frac{\mathrm{E_b}}{2H} q, \tag{7.33}$$

$$q_t + C_x q = -\frac{T\sigma_R}{2}\left(\tilde{\sigma}_R H_x + 2q\right), \tag{7.34}$$

where $\tilde{\sigma}_R = (\epsilon_p \sigma_R - 1)/\sigma_R$.

In this study we have assumed that the relaxation time is slow i.e. $T \sim 1$. This system has been analysed previously by Ozen *et al.* (2006) with the assumption of fast relaxation time $T \gg 1$. However, T may become small in case of rupture and so their $T \gg 1$ assumption can break down.

Taking the limit $T \gg 1$ the evolution equations from Ozen *et al.* (2006) for $H(x,t)$ and $C(x,t)$ are recovered:

$$H_t + (CH)_x = 0, \tag{7.35}$$

$$C_t + CC_x = \frac{\Sigma}{\mathrm{Re}} H_{xxx} + \frac{4}{\mathrm{Re}} \frac{(HC_x)_x}{H} + \frac{\mathrm{E_b} H_x}{4H}\left(\frac{\epsilon_p \sigma_R - 1}{\sigma_R}\right). \tag{7.36}$$

7.3. Evolution equations for two layer flow between electrodes

In this section we derive the evolution equations for the interface between two viscous fluids that are placed between two electrodes which when flat are parallel to the undisturbed interface (figure 7.3). The electrodes may have a corrugation: the shape of the top one is given by the function $\beta(x)$ and the shape of the bottom one is given by the function $z(x)$ (β and z are constants in the case of flat boundaries). The flow in the channel is driven by a pressure gradient and the overall flow rate through the channel is constant. The fluids are placed in the regions $0 \leq y \leq \beta H$ (fluid 1) and $-Hz \leq y \leq 0$ (fluid 2) and the undisturbed interface lies at $y = 0$. The electrodes have constant voltage potentials $V_1 = 0$ at the top and $V_2 = V_b$ at the bottom. The interface location is given by $h(x,t)$ and the interfacial tension is given by the constant γ.

7.3.1. Dimensionless equations

The equations are non-dimensionalised using the following scales:

$$(x,y) = d(x',y'), \qquad (u,v) = U(u',v'), \qquad t = \frac{d}{U}t',$$
$$V = V_b V', \qquad q = \frac{\epsilon_0 V_b}{d}q', \qquad P = \frac{\mu_1 U}{d}P'.$$

Similarly to the previous section, a system of nonlinear equations emerge. For simplicity all dashes are dropped and the non-dimensional equations take the following form:

$$\mathrm{Re}(u_{it} + u_i u_{ix} + v_i u_{iy}) = -P_{ix} + m_i(u_{ixx} + u_{iyy}), \tag{7.37}$$

$$\mathrm{Re}(v_{it} + u_i v_{ix} + v_i v_{iy}) = -P_{iy} + m_i(v_{ixx} + v_{iyy}), \tag{7.38}$$

$$u_{ix} + v_{ix} = 0, \tag{7.39}$$

$$V_{ixx} + V_{iyy} = 0. \tag{7.40}$$

with associated conditions at the interface, namely jump conditions for the normal

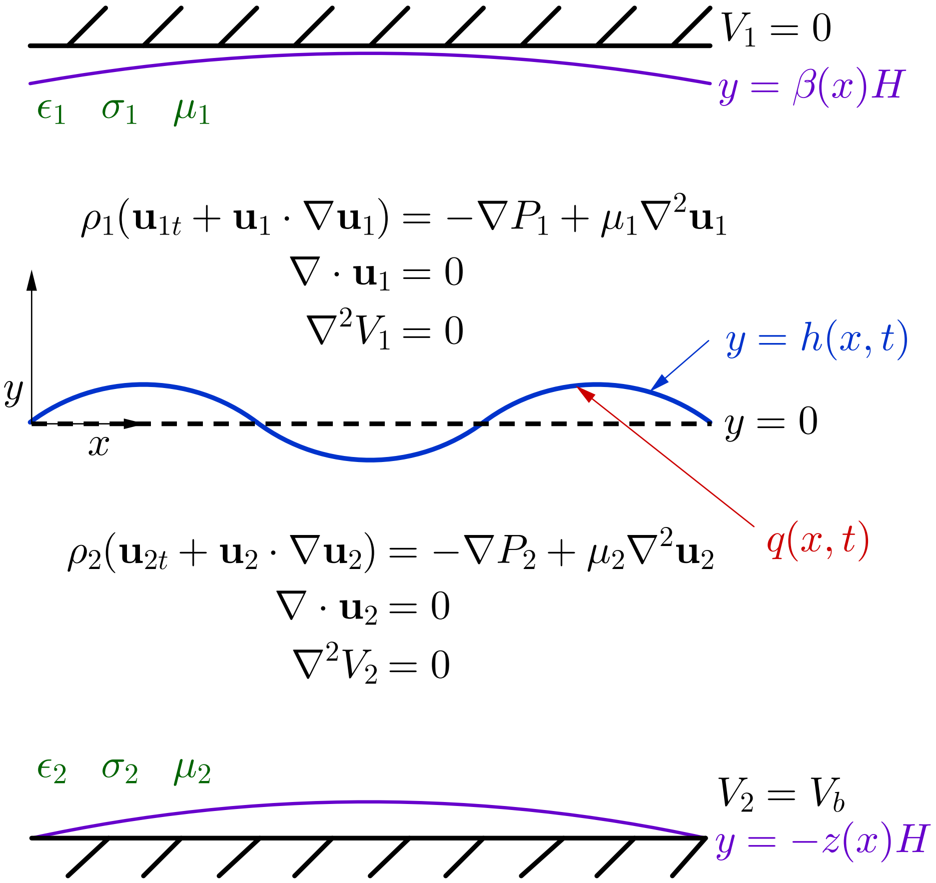

Figure 7.3. Setup of the system and governing equations.

and tangential stresses:

$$\Big[-P_i + \frac{2}{1+h_x^2}\left[m_i v_{iy}(1-h_x^2) - m_i h_x(u_{iy}+v_{ix})\right] + \\ +\bar{\epsilon}_i \frac{1-h_x^2}{2(1+h_x^2)}(V_{iy}^2 - V_{ix}^2) - \frac{2\bar{\epsilon}_i h_x}{1+h_x^2} V_{ix} V_{iy}\Big] = \frac{h_{xx}}{Ca(1+h_x^2)^{3/2}}. \tag{7.41}$$

$$\left[4h_x m_i v_{iy} + (1-h_x^2)(m_i u_{iy} + m_i v_{ix})\right] = q(V_{1x} + h_x V_{1y})\sqrt{1+h_x^2}. \tag{7.42}$$

The jump in the normal direction of the electric field is given by:

$$[h_x \bar{\epsilon}_i V_{ix} - \bar{\epsilon}_i V_{iy}] = q\sqrt{1+h_x^2}. \tag{7.43}$$

The overall flow rate condition and the kinematic condition take the following form:

$$\int_h^\beta u_1 dy + \int_{-z}^h u_2 dy = \tilde{Q}, \qquad v_i = h_t + u_i h_x. \tag{7.44}$$

where $\tilde{Q}$ is the dimensionless overall flow rate.
The system is completed with the boundary conditions and continuity across the interface for the velocity:

$$u_1 = 0 \quad \text{at} \quad y = \beta, \qquad u_2 = 0 \quad \text{at} \quad y = -z \quad \text{and} \quad [u_i] = 0, \tag{7.45}$$

and the boundary conditions and continuity condition across the interface for the voltage:

$$V_1 = 0 \quad \text{at} \quad y = \beta, \qquad V_2 = 1 \quad \text{at} \quad y = -z \quad \text{and} \quad [V_i] = 0. \tag{7.46}$$

In the process of non-dimensionalisation the following dimensionless parameters emerge:

$$\mathrm{Re} = \frac{U\rho_1 H}{\mu_1} = \frac{\epsilon_0 V_b^2 \rho_1 d}{\mu_1^2}, \qquad \mathrm{Ca} = \frac{U\mu_1}{\sigma_i},$$

$$m_i = \frac{\mu_i}{\mu_1}, \qquad \bar{\epsilon}_i = \frac{\epsilon_i}{\epsilon_0}, \qquad S_i = \frac{\sigma_i H}{U\epsilon_0},$$

where Re is the Reynolds number, Ca is the capillary number, m_i and r_i which give the ratios of viscosities and densities respectively and $\bar{\epsilon}_i$ and S_i which give the ratios of electrical permittivities and conductivities respectively.

7.3.2. Base flow

For the case of both electrodes being flat (β and z are constants in this case) we isolate the base flow by considering an undisturbed interface $h = 0$ and setting $v_i = 0$ in order to get the base flow horizontal velocities:

$$\bar{u}_1 = \frac{\bar{P}_{1x}}{2m_1}(y^2 - \beta^2) + a_1(y - \beta), \tag{7.47}$$

$$\bar{u}_2 = \frac{\bar{P}_{2x}}{2m_2}(y^2 - z^2) + a_2(y + z). \tag{7.48}$$

We conclude from the normal stress balance that the pressure gradient is constant and we denote it by $\bar{P}_x$. The constants $\bar{P}_x$, a_1 and a_2 can be determined using the tangential stress balance (7.42), the continuity of velocities across the interface and the boundary conditions (7.45) (see appendix for details).
In the case of corrugated electrodes the undisturbed interface is no longer flat so we do not isolate the base flow and set $\bar{u}_{1,2} = 0$.

7.3.3. Long-wave asymptotics

Similarly to section §7.2.2 we assume that the wavelength of interfacial disturbances λ is long compared to the channel height d and we take $\delta = d/\lambda \ll 1$. The fluid velocities and the pressures are written as the sum of the steady part and a disturbance and we make the following change of variables (for convenience, the hats on the t's and x's will henceforth be dropped):

$$\begin{gathered} u_i = \bar{u}_i + \tilde{u}_i, \qquad v_i = \delta \tilde{v}_i, \qquad x = \frac{\hat{x}}{\delta}, \qquad t = \frac{\hat{t}}{\delta}, \\ P_i = \bar{P}_i + \frac{\tilde{P}_i}{\delta}, \qquad V_i = \tilde{V}_i, \qquad q = \delta^{\alpha}\tilde{q}. \end{gathered} \tag{7.49}$$

The scaling for the vertical velocities v_i follows from the continuity equations while the one for the pressures is required for pressure driven flow at leading order. The order of magnitude of the charge q is left undetermined for now and will depend on the size

of the electric permittivities $\bar{\epsilon}_i$ and the conductivities S_i.
In non-dimensional terms the momentum equations and continuity equation become:

$$\delta Re(\tilde{u}_{it} + \bar{u}_i\tilde{u}_{ix} + \tilde{u}_i\bar{u}_{ix} + \tilde{v}_i\bar{u}_{iy} + \tilde{v}_i\tilde{u}_{iy}) = -\tilde{P}_{ix} + m_i(\delta^2\tilde{u}_{ixx} + \tilde{u}_{iyy}), \tag{7.50}$$

$$\delta^2 Re(\tilde{v}_{it} + \bar{u}_i\tilde{v}_{ix} + \tilde{u}_i\tilde{v}_{ix} + \tilde{v}_i\tilde{v}_{iy}) = -\frac{\tilde{P}_{iy}}{\delta} + m_i(\delta^3\tilde{v}_{ixx} + \delta\tilde{v}_{iyy}), \tag{7.51}$$

$$\tilde{u}_{ix} + \tilde{v}_{iy} = 0. \tag{7.52}$$

Laplace's equation for the voltages:

$$\tilde{V}_{iyy} + \delta^2\tilde{V}_{ixx} = 0. \tag{7.53}$$

Normal stress balance:

$$\begin{aligned}\Bigg[&-\bar{P}_i - \frac{\tilde{P}_i}{\delta} + \frac{2\delta}{1+\delta^2h_x^2}\left[m_i\tilde{v}_{iy}(1-\delta^2h_x^2) - m_ih_x(\bar{u}_{iy} + \tilde{u}_{iy} + \delta^2\tilde{v}_{ix})\right] + \\ &+\bar{\epsilon}_i\frac{1-\delta^2h_x^2}{2(1+\delta^2h_x^2)}\left(\tilde{V}_{iy}^2 - \delta^2\tilde{V}_{ix}^2\right) - \frac{2\bar{\epsilon}_ih_x\delta^2}{1+\delta^2h_x^2}\tilde{V}_{ix}(\tilde{V}_{iy})\Bigg] = \frac{\delta^2h_{xx}}{Ca(1+\delta^2h_x^2)^{3/2}}.\end{aligned} \tag{7.54}$$

Tangential stress balance:

$$\begin{aligned}&[4\delta^2m_ih_x\tilde{v}_{iy} + (1-\delta^2h_x^2)(m_i\bar{u}_{iy} + m_i\tilde{u}_{iy} + \delta^2m_i\tilde{v}_{ix})] = \\ &\qquad\qquad \delta^{\alpha+1}\tilde{q}(\tilde{V}_{1x} + h_x(\tilde{V}_{1y}))\sqrt{1+\delta^2h_x^2}.\end{aligned} \tag{7.55}$$

Gauss' law:

$$[\bar{\epsilon}_i\delta h_x\tilde{V}_{ix} - \bar{\epsilon}_i\tilde{V}_{iy}] = \delta^\alpha\tilde{q}\sqrt{1+\delta^2h_x^2}. \tag{7.56}$$

Overall flow rate condition:

$$\int_h^\beta(\bar{u}_1 + \tilde{u}_1)dy + \int_{-z}^h(\bar{u}_2 + \tilde{u}_2)dy = \tilde{Q}. \tag{7.57}$$

Kinematic condition:

$$h_{it} + (\bar{u}_i + \tilde{u}_i)h_{ix} - \tilde{v}_i = 0. \tag{7.58}$$

Interfacial charge conservation equation:

$$\begin{aligned} \delta^\alpha \tilde{q}_t + \delta^\alpha(\bar{u}_i + \tilde{u}_i)\tilde{q}_x + \frac{\delta h_x \tilde{q}}{1+\delta^2 h_x^2}(-\delta^2 h_x \tilde{u}_{ix} + \bar{u}_{iy} + \tilde{u}_{iy}) - \\ - \frac{\tilde{q}}{1+\delta^2 h_x^2}(-\delta^{\alpha+2} h_x \tilde{v}_{ix} + \delta^\alpha \tilde{v}_{iy}) = \\ = S_1(-\delta^2 h_x \tilde{V}_{1x} + \tilde{V}_{1y}) - S_2(-\delta^2 h_x \tilde{V}_{2x} + \tilde{V}_{2y}). \end{aligned} \tag{7.59}$$

In section §7.3.4 we consider the case when the electrical permittivity is of order one which implies that $\alpha = 0$ and $Ca \sim \delta^2$ in order for the effects of the charge and surface tension to be included. The case of large electrical permittivity ($\bar{\epsilon}_i \sim 1/\delta$) is discussed in section §7.3.5 and this time we have $\alpha = -1$ and $Ca \sim \delta^3$. These are the simplest scalings that include the effects of the electric field and of the surface tension on the system. We can distinguish the two cases, case A: moderate permittivity (§7.3.4) and case B: large permittivity (§7.3.5). In both cases we will expand the solutions in powers of δ:

$$(\tilde{u}_i, \tilde{v}_i, \tilde{P}_i, \tilde{V}_i, \tilde{q}_i) = (u_i^{(0)}, v_i^{(0)}, p_i^{(0)}, V_i^{(0)}, q_i^{(0)}) + \delta(u_i^{(1)}, v_i^{(1)}, p_i^{(1)}, V_i^{(1)}, q_i^{(1)}) + O(\delta^2).$$

Due to the small scale of the film thickness, we assume that the Reynolds number is small ($Re \sim \delta$) and so the kinematic condition (7.58) can be written in integral form using the continuity equation (7.52) (cf. Papaefthymiou *et al.* (2013)) :

$$h_t + \left(\int_{-z}^{h} \bar{u}_2 dy + \int_{-z}^{h} \tilde{u}_2^{(0)} + \delta \tilde{u}_2^{(1)} dy \right)_x = 0. \tag{7.60}$$

We take the electrical conductivities to be small ($S_{1,2} \sim \delta$) to include the effects of charge evolution and rewrite the interfacial charge concentration equation (7.59) as follows:

$$\tilde{q}_t^{(0)} + \left((\bar{u}_1 + u_1^{(0)})|_{y=h} q^{(0)} \right)_x = S_1 V_{1y}^{(0)} - S_2 V_{2y}^{(0)}. \tag{7.61}$$

Now we need to determine $u_i^{(0)}$, $u_i^{(1)}$ and $V_i^{(0)}$ by considering equations (7.52-7.57) at

$O(1)$ and $O(\delta)$ along with the boundary conditions (7.45-7.46).

7.3.4. Case A: moderate permittivity

This case corresponds to $\bar{\epsilon}_i \sim 1$ and $Ca \sim \delta^2$ i.e. moderate permittivity and high surface tension.
At $O(1)$ equations (7.50-7.53) become:

$$m_i u_{iyy}^{(0)} = p_{ix}^{(0)}, \tag{7.62}$$

$$p_{iy}^{(0)} = 0, \tag{7.63}$$

$$u_{ix}^{(0)} + v_{iy}^{(0)} = 0, \tag{7.64}$$

$$V_{iyy}^{(0)} = 0. \tag{7.65}$$

The interfacial conditions (7.54-7.56) and the continuity of velocity across the interface to be evaluated at $y = h(x,t)$ are:

$$[p_i^{(0)}] = 0, \tag{7.66}$$

$$[m_i u_{iy}^{(0)}] = 0, \tag{7.67}$$

$$q^{(0)} = [-\bar{\epsilon}_i V_{iy}^{(0)}], \tag{7.68}$$

$$[u_i^{(0)}] = 0. \tag{7.69}$$

The flow rate (7.57) condition is:

$$\int_h^\beta (\bar{u}_1 + u_1^{(0)}) dy + \int_{-z}^h (\bar{u}_2 + u_2^{(0)}) dy = \tilde{Q}. \tag{7.70}$$

At $O(\delta)$ equations (7.50-7.52) become:

$$m_i u_{iyy}^{(1)} = p_{ix}^{(1)}, \tag{7.71}$$

$$p_{iy}^{(1)} = 0, \tag{7.72}$$

$$u_{ix}^{(1)} + v_{iy}^{(1)} = 0. \tag{7.73}$$

The interfacial conditions (7.54-7.55) and the continuity of velocity across the interface to be evaluated at $y = h(x,t)$ are:

$$[-p_i^{(1)} + \bar{\epsilon}_i \frac{(V_{iy}^{(0)})^2}{2}] = h_{xx}, \tag{7.74}$$

$$[m_i u_{iy}^{(1)}] = q^{(0)} \left(V_{1x}^{(0)} + h_x \tilde{V}_{1y}^{(0)} \right), \tag{7.75}$$

$$[u_i^{(1)}] = 0. \tag{7.76}$$

The flow rate (7.57) condition is:

$$\int_h^\beta u_1^{(1)} dy + \int_{-z}^h u_2^{(1)} dy = 0. \tag{7.77}$$

We find the horizontal velocities and the voltage potential at $O(1)$:

$$u_1^{(0)} = \frac{p_x^{(0)}}{2m_1}(y^2 - \beta^2) + e_1(x,t)(y - \beta), \tag{7.78}$$

$$u_2^{(0)} = \frac{p_x^{(0)}}{2m_2}(y^2 - z^2) + e_2(x,t)(y + z), \tag{7.79}$$

$$V_1^{(0)} = d_1(x,t)(y - \beta), \tag{7.80}$$

$$V_2^{(0)} = d_2(x,t)(y + z) + V_b. \tag{7.81}$$

The horizontal velocities at $O(\delta)$ are given by the following expressions:

$$u_1^{(1)} = \frac{p_{1x}^{(1)}}{2m_1}(y^2 - \beta^2) + f_1(x,t)(y - \beta), \tag{7.82}$$

$$u_2^{(1)} = \frac{p_{2x}^{(1)}}{2m_2}(y^2 - z^2) + f_2(x,t)(y + z). \tag{7.83}$$

The functions $D_3(x,t)$, $D_4(x,t)$, $p_x^{(0)}$, $p_{ix}^{(1)}$, $d_i(x,t)$, $e_i(x,t)$ and $f_i(x,t)$, $i = 1, 2$ depend on the parameters in the problem, on the interface $h(x,t)$ and on the charge concentration $q^{(0)}$ (see appendix for derivations).

We can now substitute the velocities and voltages into (7.60-7.61) and write down the two coupled nonlinear evolution equations:

$$h_t + \left\{ \frac{D_3}{6m_2} \left[D_4(\bar{P}_x + p_x^{(0)} + \delta p_{2x}^{(1)}) + 3m_2(a_2 + e_2 + \delta f_2) \right] \right\}_x = 0, \tag{7.84}$$

$$q_t^{(0)} + \left\{ (h-\beta) \left[(\bar{P}_x + p_x^{(0)}) \frac{(h+\beta)}{2m_1} + a_1 + e_1 \right] q^{(0)} \right\}_x = S_1 d_1 - S_2 d_2. \tag{7.85}$$

For large conductivities ($S_i \sim 1/\delta$) the evolution equation for the charge (7.85) simplifies and we can write $q^{(0)}(x,t)$ as a function of $h(x,t)$:

$$q^{(0)} = \frac{\bar{\epsilon}_1 - \bar{\epsilon}_2 R}{R(h+1) - (h-\beta)}. \tag{7.86}$$

where $R = S_1/S_2$. This limit is useful for validating our numerical results and this can be done by comparing the numerical solutions of the full system of equations (7.60-7.61) with the numerical solutions the equation (7.84) with $q^{(0)}$ given by the above expression (7.86).

7.3.5. Case B: large permittivity

This case corresponds to $\bar{\epsilon}_i \sim 1/\delta$ and $Ca \sim \delta^3$ i.e. large permittivity and very high surface tension. At $O(1)$ equations (7.50-7.53) become:

$$m_i u_{iyy}^{(0)} = p_{ix}^{(0)} \tag{7.87}$$

$$p_{iy}^{(0)} = 0 \tag{7.88}$$

$$u_{ix}^{(0)} + v_{iy}^{(0)} = 0 \tag{7.89}$$

$$V_{iyy}^{(0)} = 0 \tag{7.90}$$

The interfacial conditions (7.54-7.56) and the continuity of velocity across the interface to be evaluated at $y = h(x,t)$ are:

$$[-p_i^{(0)} + \bar{\epsilon}_i \frac{(V_{iy}^{(0)})^2}{2}] = h_{xx} \tag{7.91}$$

$$[m_i u_{iy}^{(0)}] = q^{(0)} \left(V_{1x}^{(0)} + h_x \tilde{V}_{1y}^{(0)} \right) \tag{7.92}$$

$$q^{(0)} = [-\bar{\epsilon}_i V_{iy}^{(0)}] \tag{7.93}$$

$$[u_i^{(0)}] = 0 \tag{7.94}$$

The flow rate (7.57) condition is:

$$\int_h^\beta (\bar{u}_1 + u_1^{(0)}) dy + \int_{-z}^h (\bar{u}_2 + u_2^{(0)}) dy = \tilde{Q}. \tag{7.95}$$

The horizontal velocities are given by the following expressions:

$$u_1^{(0)} = \frac{p_{1x}^{(1)}}{2m_1}(y^2 - \beta^2) + f_1(x,t)(y - \beta) \tag{7.96}$$

$$u_2^{(0)} = \frac{p_{2x}^{(1)}}{2m_2}(y^2 - z^2) + f_2(x,t)(y + z) \tag{7.97}$$

where $f_{1,2}$ are the same as in section §7.3.4 and $p_{ix}^{(0)}$, $i = 1, 2$ are given in the appendix. The voltages are the same as in section §7.3.4.
Substituting the velocities and voltages into (7.60-7.61) leads to the following evolution equations:

$$h_t + \left\{ \frac{D_3}{6m_2} \left[D_4(\bar{P}_x + p_{2x}^{(0)}) + 3m_2(a_2 + f_2) \right] \right\}_x = 0 \tag{7.98}$$

$$q_t^{(0)} + \left\{ (h - \beta) \left[(\bar{P}_x + p_{1x}^{(0)}) \frac{(h + \beta)}{2m_1} + a_1 + f_1 \right] q^{(0)} \right\}_x = S_1 d_1 - S_2 d_2 \tag{7.99}$$

If we switch off the flow in equations (7.98-7.99) and consider the case when both boundaries are flat, we recover the case analysed by Craster & Matar (2005).

$$h_t + \left\{ \frac{D_3}{6m_2} \left(D_4 p_{2x}^{(0)} + 3m_2 f_2 \right) \right\}_x = 0$$

$$q_t^{(0)} + \left\{ (h-\beta) \left(p_{1x}^{(0)} \frac{(h+\beta)}{2m_1} + f_1 \right) q^{(0)} \right\}_x = S_1 d_1 - S_2 d_2 \tag{7.100}$$

where

$$\begin{aligned} p_{1x}^{(0)} &= p_{2x}^{(0)} + h_{xxx} + \epsilon_1 d_{1x} d_1 - \epsilon_2 d_{2x} d_2 \\ p_{2x}^{(0)} &= \frac{-E_6(h_{xxx} + \epsilon_1 d_{1x} d_1 - \epsilon_2 d_{2x} d_2) - E_8 q^{(0)}}{E_6 + E_7} \end{aligned} \tag{7.101}$$

This is then ideal to answer the question whether flow affects pattern formation.

7.4. Numerical methods

The behaviour of the system of equations for the single sheet problem and the system of equations for the two layer flow problem described in this chapter has been analysed using two time dependent, numerical codes written in FORTRAN. Both codes rely on the method of lines, a numerical approach described in §2.2 which reduces a system of m PDEs to a system of $m \times N$ ODEs in just one variable t, through a spatial discretisation with N the number of grid points in x. The first code we used is PDECOL which relies on a finite element technique for the spatial discretisation and Gear's method for the time integration, a description of this solver was given in §2.2.

The second numerical scheme performs the time integration using DASSL, an ordinary differential equations solver (Petzold, 1982). The spatial discretisation is based on a spectral method in which differentiation is performed in spectral space and the change from real space to spectral space is done by using Fast Fourier Transforms. The resulting system of ODEs is solved by using DASSL which approximates derivatives using the k^{th} order backward differentiation formula where $1 \leq k \leq 5$; the order k and the time step size are chosen at every step. The resulting equation is solved using Newton's method. The results from the two numerical schemes were in perfect agreement with each other but PDECOL was abandoned in the second half of this chapter in favour of the code based on DASSL due to the higher efficiency of the latter.

8. Rupture of electrified viscous liquid sheets under the effect of a horizontal electric field

8.1. Evolution equations and linear stability

In this chapter we present results for a thin, electrified liquid film under the effect of an electric field parallel to the undisturbed interfaces. The setup of the system is as in Figure 7.2 and the evolution equations for the interface $H(x,t)$, the horizontal fluid velocity $C(x,t)$ and the interfacial charge concentration $q(x,t)$ are as follows:

$$H_t + (CH)_x = 0, \tag{8.1}$$

$$C_t + CC_x = \frac{\Sigma}{\mathrm{Re}} H_{xxx} + \frac{4}{\mathrm{Re}} \frac{(HC_x)_x}{H} - \frac{\mathrm{E_b}}{2H} q, \tag{8.2}$$

$$q_t + C_x q = -\frac{T\sigma_R}{2} \left(\tilde{\sigma}_R H_x + 2q \right), \tag{8.3}$$

where $\tilde{\sigma}_R = (\epsilon_p \sigma_R - 1)/\sigma_R$ and $T = L\sigma_1/U\epsilon_1$.

We look for solutions proportional to $\exp(ikx + st)$ to get a dispersion relation for the growth rate s and the wavenumber k:

$$s\left(s + \frac{4k^2}{Re}\right)(s + \bar{T}) + k^2 (s + \bar{T}) W_f k^2 - \frac{1}{4} k^2 \bar{T} E_b \sigma_R \tilde{\sigma}_R = 0, \tag{8.4}$$

where $\bar{T} = T\sigma_R$ and $W_f = \Sigma/Re$. This is a cubic in s and we can then extract useful information regarding the stability of the system.

For instance, the critical wavenumber k_c, where k_c is given by:

$$k_c = \sqrt{\frac{\tilde{\sigma} E_b}{4W_f}}.$$

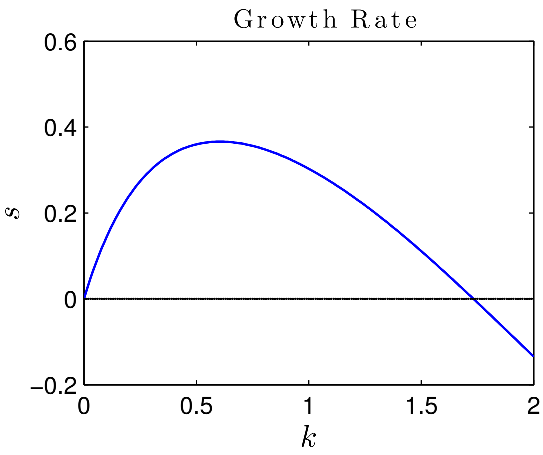

Figure 8.1. Growth rate s against wavenumber k with $Re = 1$, $\tilde{\sigma}_R = 3$, $W_f = 1$, $E_b = 4$, $\bar{T} = 1$.

Unstable modes exist below k_c if $\tilde{\sigma} > 0$ and this is in agreement with a previous stability analysis for the same system but with fast charge relaxation times analysed by Papageorgiou & Petropoulos (2004) and Ozen *et al.* (2006). Figure 8.1 shows the growth rate s against the wavenumber k for a typical set of parameters and we see that a band of instability is present.

8.2. Numerical results

The system of equations (7.32-7.34) is solved in time using the two numerical schemes described in §7.4. The nonlinear evolution equations (7.32-7.34) are solved numerically subject to the following initial conditions:

$$H(x,0) = 1 + h_0\cos(x), \qquad C(x,0) = c_0\sin(x), \qquad q(x,0) = q_0\sin(x),$$

and we choose a periodic interval $-\pi \leq x \leq \pi$.

Figure 8.2 gives the profiles of the interface height, the horizontal fluid velocity and the charge at time $t = 8.1015$ for the parameters examined in figure 8.1. As predicted by the linear stability analysis, initially small disturbances grow and, as it appears from figure 8.2.d, the sheet approaches rupture at two points in finite time. The charge and the horizontal fluid velocity become locally unbounded at these points and increase rapidly. This is different behaviour to the case with fast charge relaxation times analysed by

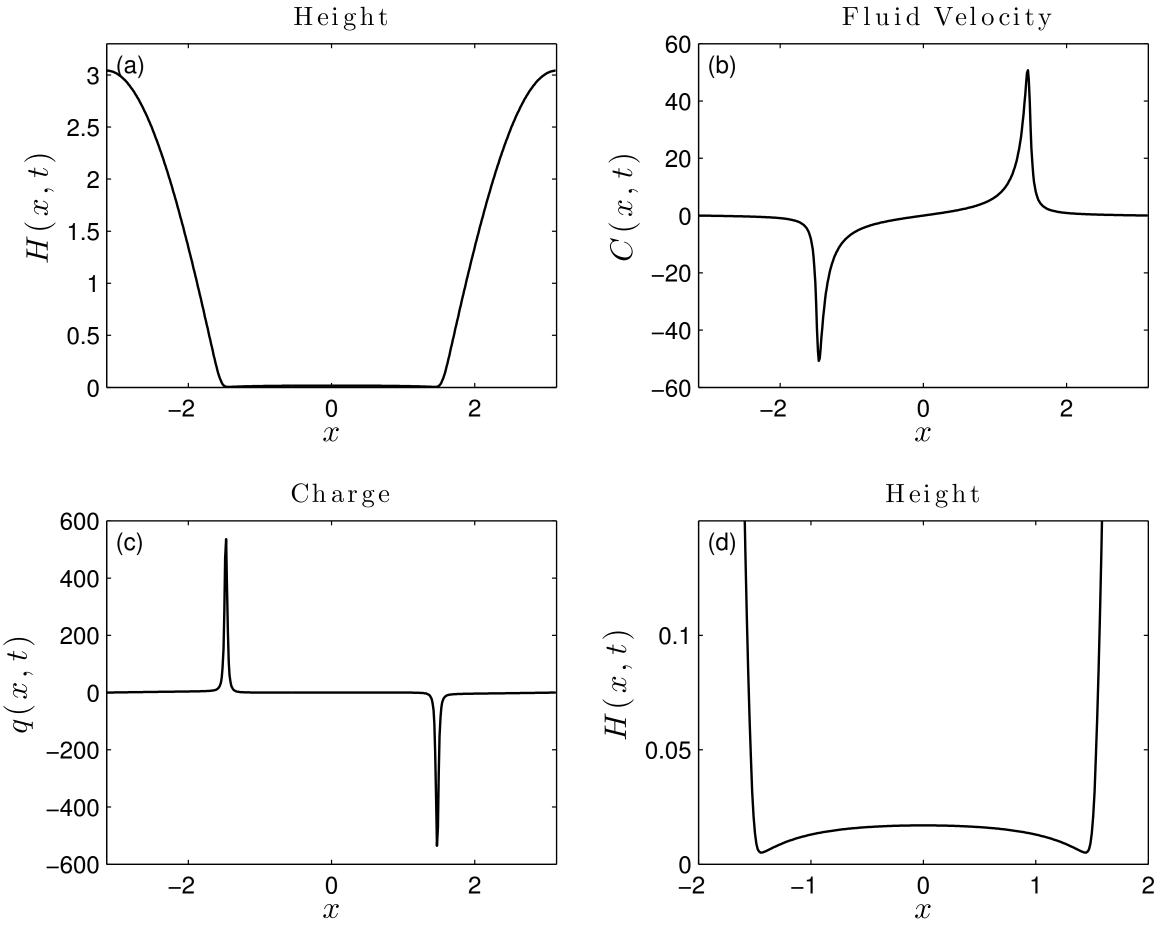

Figure 8.2. Solutions for (7.32-7.34) at $t = 8.1015$. Parameters: $Re = 1$, $\tilde{\sigma}_R = 3$, $W_f = 1$, $E_b = 4$, $\bar{T} = 1$ and $c_0 = h_0 = q_0 = 0.2$.

Ozen *et al.* (2006) where rupture can only occur at asymptotically large times.

8.3. Self-similar solution

Given the apparent rupture in finite time found numerically we attempt to find a similarity solution near rupture. Assuming that the interface $h(x,t)$ goes to zero at $x = x_{rup}$ at a finite time t_{rup}, we look for self-similar solutions for $\tau = t - t_s \ll 1$ by considering

$$H = \tau^{\alpha}\bar{H}(\xi); \qquad C = \tau^{\beta}\bar{C}(\xi); \qquad q = \tau^{\gamma}\bar{Q}(\xi);$$

Balancing terms in the evolution equations we find that close to rupture the surface tension term is small compared to the other terms in equation (8.2) and the terms on the right hand side of equation (8.3) are small compared to the ones on the left hand side. We determine analytically the following scalings:

$$C \sim \tau^{-1/2},$$
$$x \sim \tau^{1/2},$$
$$\frac{q}{H} \sim \tau^{-3/2}.$$

Guided by this we seek a similarity solution of the form:

$$H = \tau^{\alpha}\bar{H}(\xi); \qquad C = \tau^{-1/2}\bar{C}(\xi); \qquad q = \tau^{\alpha-3/2}\bar{Q}(\xi); \tag{8.5}$$

where $\xi = (x - x_{rup})/\tau^{1/2}$. The parameter α cannot be determined by our scaling analysis as this is a similarity solution of the second kind (Kindal & Atkinson, 1997). Substituting the ansatz (8.5) into the evolution equations (8.1-8.3) and retaining leading order terms gives the following similarity equations:

$$\frac{1}{2}\xi\bar{H}' - \alpha\bar{H} + (\bar{H}\bar{C})' = 0, \tag{8.6}$$

$$\frac{1}{2}(\xi\bar{C})' + \frac{1}{2}(\bar{C}^2)' = \frac{4}{Re}\frac{(\bar{H}\bar{C}')'}{\bar{H}} - \frac{E_b}{2}\frac{\bar{Q}}{\bar{H}}, \tag{8.7}$$

$$\frac{1}{2}\xi\bar{Q}' - (\alpha - 3/2)\bar{Q} + \bar{Q}\bar{C}' = 0. \tag{8.8}$$

Now we attempt to gain insight from numerics to validate the scalings derived analytically and to determine the value of α. We attempt to approach the point of rupture as closely as possible by reducing the time step and doubling the number of points in

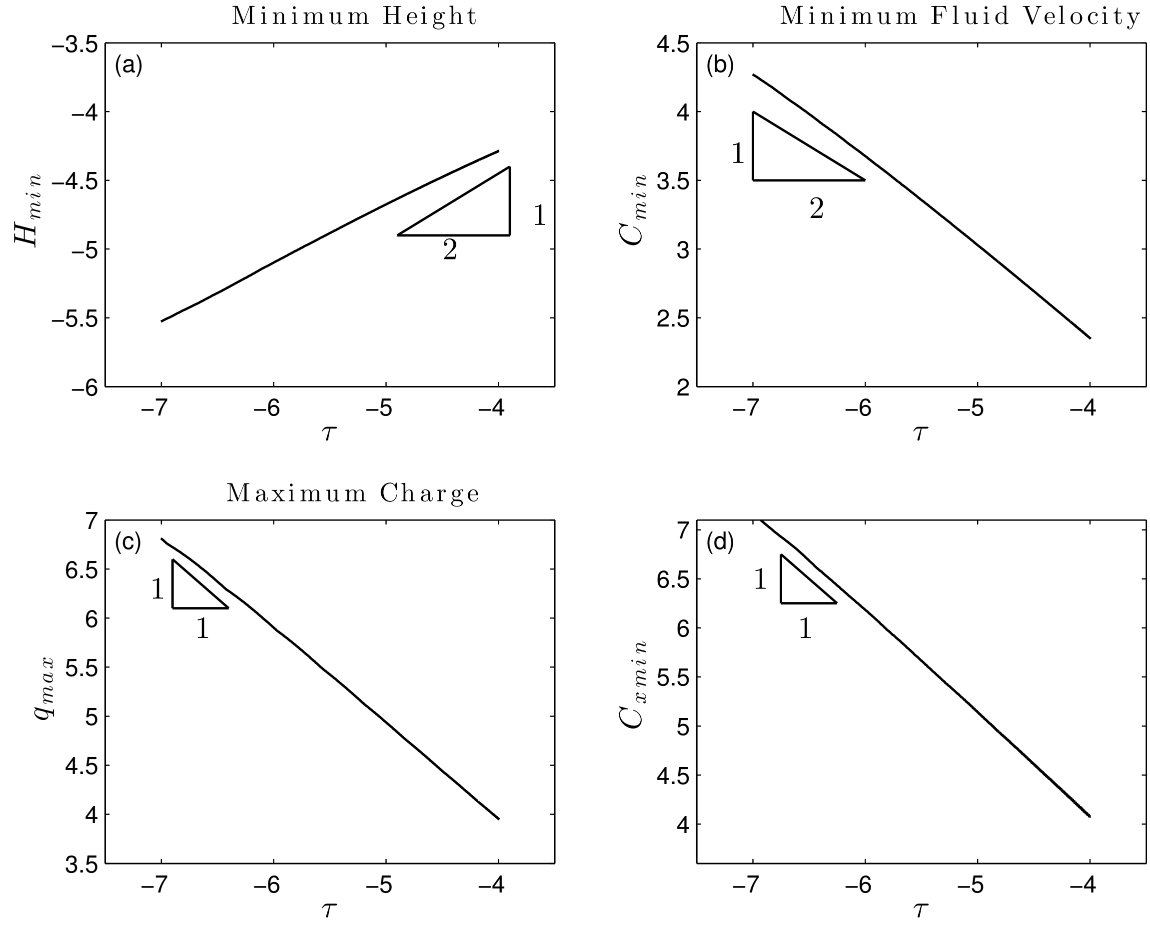

Figure 8.3. Log-log plots with $\tau = t_{rup} - t$ where $t_{rup} = 8.10323$.

space in our numerical scheme. We estimate the rupture time to be $t_{rup} = 8.10323$ and plot the minima and maxima of H, C, q and C_{xx} against $\tau = t_{rup} - t$ on a log-log plot. Figure 8.3.b confirms the scaling found previously for the fluid velocity C and combining it with figure 8.3.d also confirms the scaling for x. Figures 8.3.a,c confirm that the ratio of charge q to interfacial height H scales like $\tau^{-3/2}$ and they also suggest that the value of α is equal to $1/2$. By evaluating the slopes in figure 8.3 we find the following estimates for the scalings:

$$H_{min} \sim \tau^{0.4250},$$

$$C_{min} \sim \tau^{-0.6140},$$

$$q_{max} \sim \tau^{-0.9249},$$

$$C_{xmin} \sim \tau^{-0.9971},$$

$$C_{xxmin} \sim \tau^{-1.4474}.$$

Through the manipulation of C_{xmim} and C_{xxmim} we get $x \sim \tau^{0.4503}$ which is close to our estimation of the scaling of x from dimensional analysis. The above estimates also suggest that $H \sim \tau^{1/2}$ hence $\alpha = 1/2$. We now look at the behaviour in the far field for large ξ, here the solutions are quasi static so they must be independent of time:

$$H \sim \tau^{\alpha} \frac{(x - x_{rup})}{\tau^{1/2}} \qquad \Rightarrow \qquad \alpha = \frac{1}{2}$$

and this gives us further reassurance that $\alpha = 1/2$ is a reasonable estimate. We proceed to look at the far field behaviour of the horizontal fluid velocity and the charge:

$$C \sim \frac{1}{|\xi|} \qquad\qquad Q \sim \frac{1}{\xi^2}$$

These scalings are in agreement with the full numerical results presented in figure 8.2: the fluid velocity C decays away from the rupture points and the charge Q decays even faster. It is also possible to derive the above far field scalings from balancing terms in equations (8.6-8.8) when ξ is large.

Due to the singular nature of the problem there is a difficulty in an accurate calculation of numerical results close to rupture which might lead to inaccuracies in the estimation of scalings. We believe that a more robust numerical scheme is required in order to make a reasonable comparison between the full time dependant numerical solution and the solution of the similarity equations (8.6-8.8), but this is beyond the scope of this thesis.

8.4. Summary of research

We have examined the stability of the free surface of an electrified liquid sheet under the effect of a horizontal electric field. The ratio of fluid to electric time scales is taken to be of $O(1)$ and nonlinear coupled evolution equations are derived for the thickness of the sheet, the horizontal fluid velocity and the surface charge. A linear stability analysis suggests that instability can occur if $\epsilon_p \sigma_R > 1$ where ϵ_p is the ratio of dielectric permittivities and σ_R is the ratio of electric conductivities and this is in agreement with previous studies by Papageorgiou & Petropoulos (2004) and Ozen *et al.* (2006). These predictions are confirmed by solving the nonlinear evolution equations numerically using two different numerical schemes, one based on approximation by cubic splines, the other, based on spectral methods. The results show that initially small perturbations grow in time and may lead to rupture at two points, with the surface charge and horizontal fluid velocity becoming locally unbounded at these two points.

We seek a similarity solution for the behaviour of the system near rupture. We are faced with a similarity solution of the second kind where the exponents of two of the self-similar variables cannot be determined from dimensional analysis. We attempt to fix these two exponents using insight from numerics and comparing them with information we deduce from analysing the far field of the solutions. In order to make a reasonable comparison between the solution of the similarity equation and the full time dependant solution we would require for the latter to come much closer the the point of rupture. This would only be possible with a bespoke numerical scheme that is able to deal with the singular nature of the problem and the development of such a code is beyond the scope of this thesis. The reader is referred to Barannyk *et al.* (2015*b*) in which the authors find a similarity solution of the second kind similar to the one presented here but in the case of two fluids under the effect of a tangential electric field. They use a robust numerical scheme that allows them to find an accurate estimation for the rupture time.

9. Two layer flow of thin leaky dielectric films between electrodes

9.1. Evolution equations and linear stability

In this chapter we consider the behaviour of the interface between two leaky dielectric fluids flowing between two flat electrodes that are held at constant voltages. The setup of the system is shown in figure 7.3 with β and z are taken to be constants. We consider the two cases A and B and give a comparison between the two behaviours. The evolution equations for the case of moderate permittivity (case A) were derived in §7.3 and are given here again:

$$h_t + \left\{ \frac{D_3}{6m_2} \left[D_4(\bar{P}_x + p_x^{(0)} + \delta p_{2x}^{(1)}) + 3m_2(a_2 + e_2 + \delta f_2) \right] \right\}_x = 0, \tag{9.1}$$

$$q_t^{(0)} + \left\{ (h-\beta) \left[(\bar{P}_x + p_x^{(0)}) \frac{(h+\beta)}{2m_1} + a_1 + e_1 \right] q^{(0)} \right\}_x = S_1 d_1 - S_2 d_2. \tag{9.2}$$

The evolution equations for the case of large permittivity (case B) are:

$$h_t + \left\{ \frac{D_3}{6m_2} \left[D_4(\bar{P}_x + p_{2x}^{(0)}) + 3m_2(a_2 + f_2) \right] \right\}_x = 0 \tag{9.3}$$

$$q_t^{(0)} + \left\{ (h-\beta) \left[(\bar{P}_x + p_{1x}^{(0)}) \frac{(h+\beta)}{2m_1} + a_1 + f_1 \right] q^{(0)} \right\}_x = S_1 d_1 - S_2 d_2 \tag{9.4}$$

The evolution equations for the two cases A and B are linearised about the following steady state:

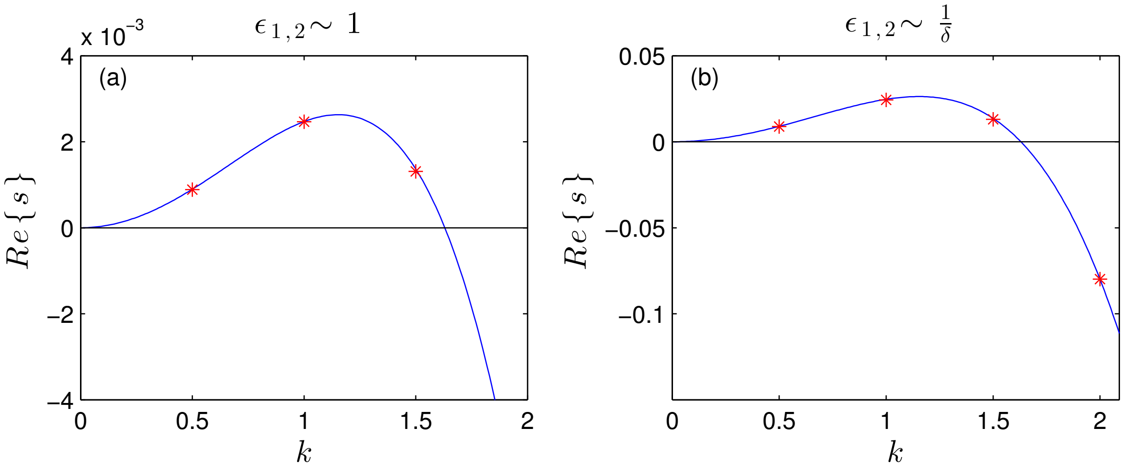

Figure 9.1. Linear stability for two cases: (a) case A: $\epsilon_{1,2} \sim 1$, $\alpha = 0$, $S_{1,2} \sim \delta$; (b) case B $\epsilon_{1,2} \sim \frac{1}{\delta}$, $\alpha = -1$. Dispersion curves compared to numerical predictions for the growth rate from the simulations of the full PDE system (stars). Parameters: $\beta = 0.55$, $z = 1$, $\bar{\epsilon}_1 = 1$, $\bar{\epsilon}_2 = 2$, $m_1 = 1$, $m_2 = 1$, $S_1 = 100$, $S_2 = 1000$.

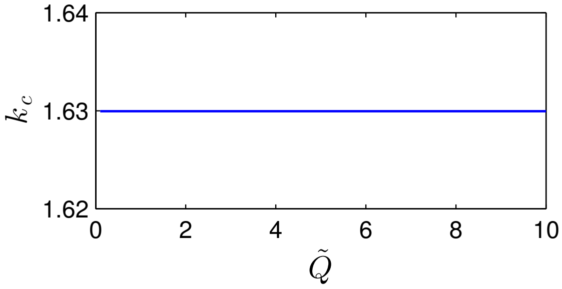

Figure 9.2. Neutral stability curve for case A when $\bar{\epsilon}_i \sim 1$, $\alpha = 0$ when the flux $\tilde{Q}$ is varied. All other parameters are the same as in figure 9.3.

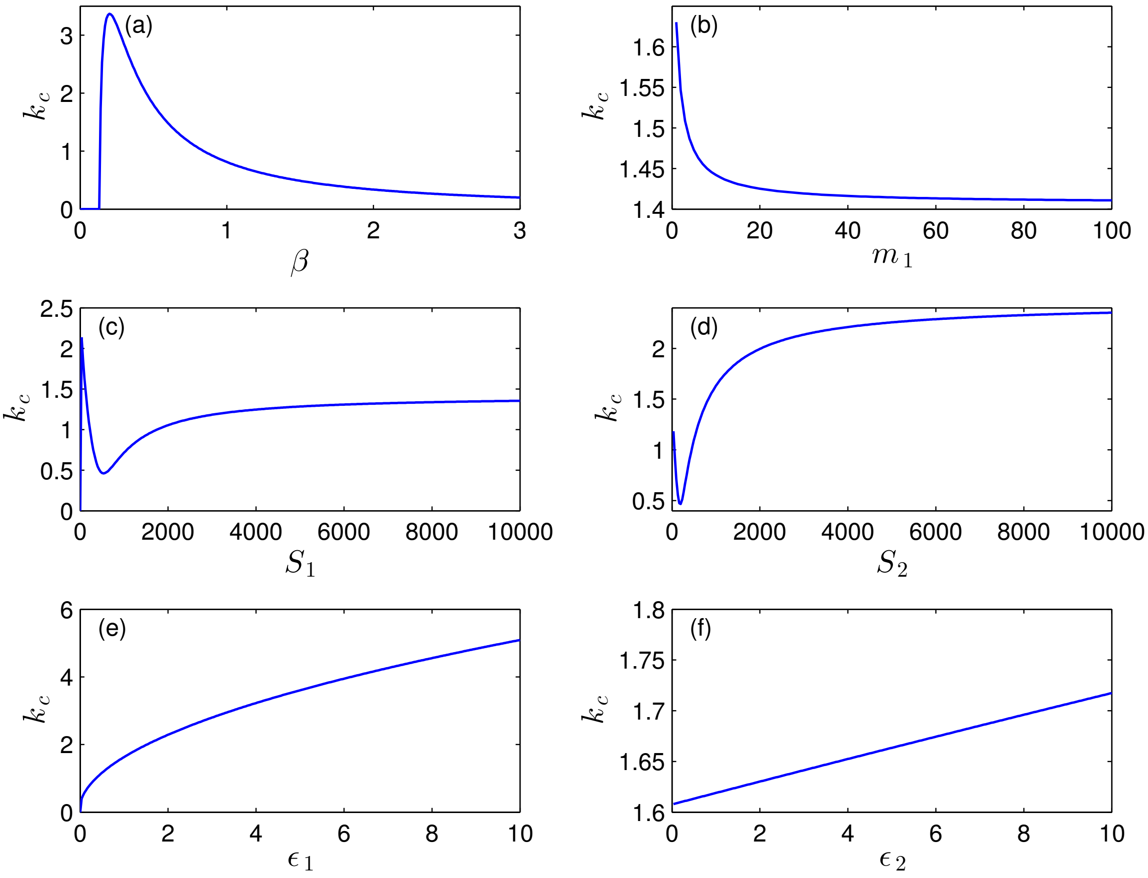

Figure 9.3. Neutral stability curves for case A when $\bar{\epsilon}_{1,2} \sim 1$, $\alpha = 0$. Variation of cutoff mode k_c as the physical parameters are changed. Parameters (except the one that is varied): $\beta = 0.55$, $z = 1$, $\bar{\epsilon}_1 = 1$, $\bar{\epsilon}_2 = 2$, $m_1 = 1$, $m_2 = 1$, $S_1 = 100$, $S_2 = 1000$, $\delta = 10^{-1}$.

$$(\bar{h},\bar{q}) = \left(0, \frac{S_2\bar{\epsilon}_1 - S_1\bar{\epsilon}_2}{S_1 + \beta S_2}\right) \tag{9.5}$$

We then look for solutions proportional to $\exp(ikx + st)$ to find a dispersion relation for the growth rate s and the wavenumber k. The algebra was done with the help of Maple.

Fig.9.1 shows the dispersion curve for the two cases A and B for typical values of the parameters: $\beta = 0.55$, $z = 1$, $\bar{\epsilon}_1 = 1$, $\bar{\epsilon}_2 = 2$, $m_1 = 1$, $m_2 = 1$, $S_1 = 100$, $S_2 = 1000$. In both cases there is a band of unstable modes and the maximum of the real part of the growth rate s is roughly an order of magnitude larger in case B compared to case A so we expect small initial disturbances to grow faster in the second case. The figure shows good agreement between values of the growth rate found analytically and numerically. This check provides reassurance that the analysis and the numerics are both correct. The growth rate is found from numerics in the following way: the equations are solved with the following initial condition for the height:

$$h(x,0) = h_0\cos(kx),$$

where h_0 is taken to be small. According to linear theory for early times the height takes the following form:

$$h(x,t) = e^{s_{num}t}h_0\cos(kx),$$

where s_{num} is the growth rate and we can find it through the following manipulation:

$$h(0,t) = e^{s_{num}t}h_0 \qquad \Rightarrow \qquad s_{num} = \frac{1}{t}\ln\left|\frac{h(0,t)}{h_0}\right|.$$

Since the solutions are in the form of travelling waves the values of $h(0,t)$ to use have to be at times t when the minimum of h goes through $x = 0$.

Unstable modes exist below a critical wavenumber k_c. Figure 9.3 shows how k_c depends on each physical parameter for the case A when $\bar{\epsilon}_{1,2} \sim 1$ with regions of instability below the curves. From figure 9.3.a we can see that there exists a value of the ratio of layer depths β for which the cutoff mode is highest and above this value k_c decreases with increasing β. Figure 9.3.b shows that as the viscosity ratio m_1 increases, the cutoff wavenumber decreases, which physically means that viscosity has a stabilising effect. We can see that the cutoff wavenumber increases with increasing conductivity (figures 9.3.c-d) and increasing permittivity ratios (figures 9.3.e-f) which means that electrical

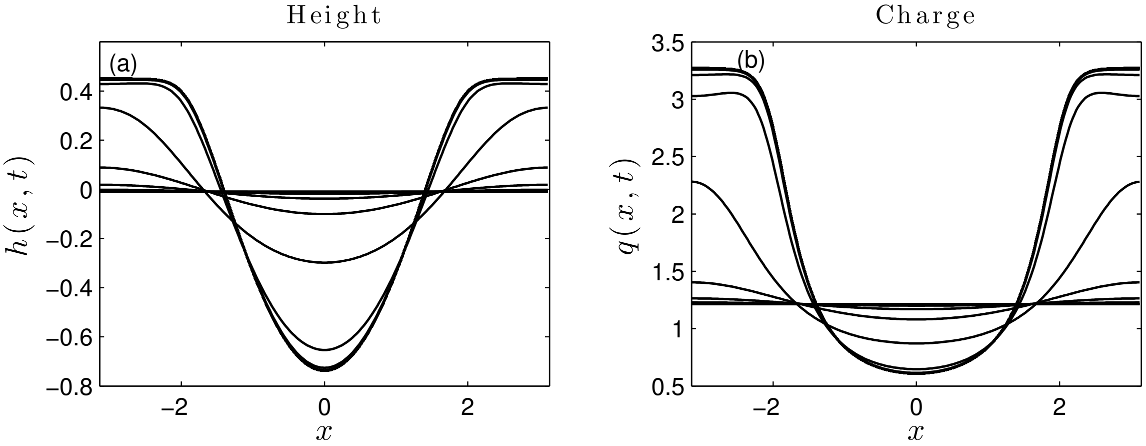

Figure 9.4. Solutions of (9.7-9.8) i.e. case A at $t = 0$ (solid line), $t = 340$ (dashed line), $t = 680$ (dot dashed line) and $t = 1000$ (dotted line). Parameters: $\beta = 0.5$, $z = 1$, $\bar{\epsilon}_1 = 1$, $\bar{\epsilon}_2 = 2$, $m_1 = 1$, $m_2 = 1$, $S_1 = 100$, $S_2 = 1000$. Parameters in the initial condition: $h_0 = q_0 = -0.01$, $k = 1$.

effects drive the instability. It can be seen from figure 9.2 that in the linear regime the effect of the flux $\tilde{Q}$ on stability is negligible.

9.2. Numerical results

The evolution equations (9.1-9.2) i.e. case A and (9.3-9.4) i.e. case B are solved using the numerical scheme that employs spectral methods described in chapter §7.4.
The equations are solved numerically subject to the following initial conditions:

$$\begin{aligned} h(x,0) &= h_0 \cos(kx), \\ q(x,0) &= \frac{S_2\bar{\epsilon}_1 - S_1\bar{\epsilon}_2}{S_1 + \beta S_2} + q_0 \cos(kx), \end{aligned} \tag{9.6}$$

and we choose a periodic interval $-\pi/k \le x \le \pi/k$.
To reassure ourselves of the validity of out model, we compute the solution of the zero flux case and compare it to the work by Craster & Matar (2005). The equations are a simplification of case B and are given by:

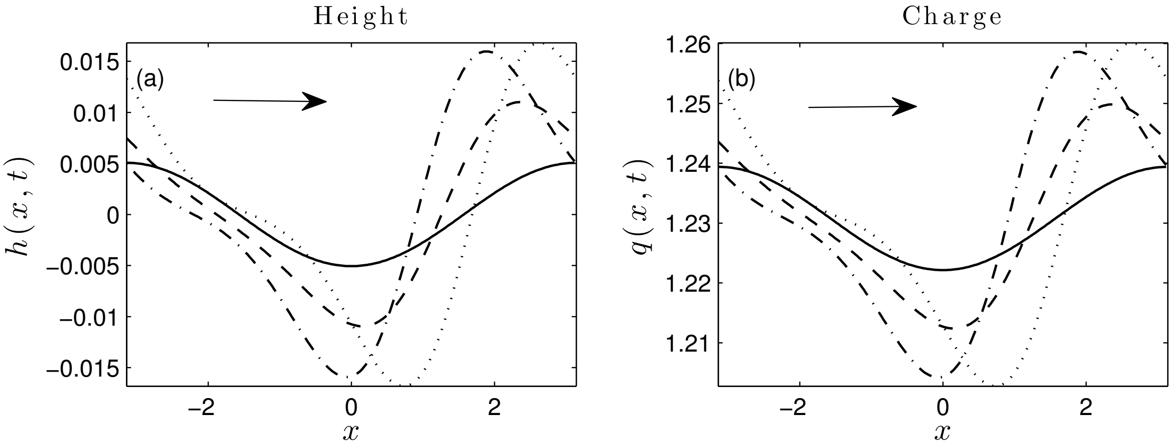

Figure 9.5. Solutions of (7.84-7.85) i.e. case A at $t = 0$ (solid line), $t = 340$ (dashed line), $t = 680$ (dot dashed line) and $t = 1000$ (dotted line). Parameters: $\beta = 0.55$, $z = 1$, $\bar{\epsilon}_1 = 1$, $\bar{\epsilon}_2 = 2$, $m_1 = 1$, $m_2 = 1$, $S_1 = 100$, $S_2 = 500$, $\delta = 10^{-1}$. Parameters in the initial condition: $h_0 = q_0 = -0.01$, $k = 1$.

$$h_t + \left\{ \frac{D_3}{6m_2} \left(D_4 p^{(0)}_{2x} + 3m_2 f_2 \right) \right\}_x = 0 \tag{9.7}$$

$$q^{(0)}_t + \left\{ (h-\beta) \left(p^{(0)}_{1x} \frac{(h+\beta)}{2m_1} + f_1 \right) q^{(0)} \right\}_x = S_1 d_1 - S_2 d_2 \tag{9.8}$$

Figure 9.4 gives the profiles of the interfacial height and the charge concentration for $t = 0 - 500$ in 100 equal steps. Our results are in perfect agreement with the previous work by Craster & Matar (2005).

We now proceed to compute the solutions to equations (9.1-9.2) and equations (9.3-9.4). The numerical solutions were compared with linear theory in order to validate the code and good agreement was found between the two (see section on linear stability §9.1). Figures 9.5 and 9.6 show the profiles of the height of interfacial deformation h and of the charge concentration q. The arrows show the direction of the flow. The solution is given by travelling waves whose amplitude grows in time and eventually appears to become constant. The waves have a constant speed that agrees with the speed found from linear theory ($v_p = -Im\{s\}/k$, where v_p is the phase velocity, s is the growth rate and k is the wavenumber). As predicted by our linear stability analysis, the amplitude of the waves grows much more in case B when $\bar{\epsilon}_i \sim 1/\delta$: this is due to the fact that electrical effects, which are destabilising, come in at a higher order than in case A when $\bar{\epsilon}_i \sim 1$.

Even though the solutions presented in figures 9.5 and 9.6 appear to be nonlinear travelling waves, closer analysis of the data establishes that they are in fact travelling time-periodic waves (such structures have been found in simpler weakly nonlinear model equations such as the Kuramoto-Sivashinsky equation - see for example Akrivis *et al.* (2011)). To accurately predict such dynamics we make use of the energy of the solution (the L^2-norm of h) defined as

$$E(t) = \int_{-\pi/k}^{\pi/k} h^2(x,t)\,dx, \tag{9.9}$$

and note that this is computed with spectral accuracy either using Parseval's theorem since the Fourier coefficients are known, or using trapezoidal quadrature which is spectrally accurate for periodic functions; we also calculate dE/dt in order to construct the phase planes presented below. Figure 9.7.a gives the evolution of $E(t)$ for case B with the same parameters as the ones used to compute the results in figure 9.6. We observe time periodic behaviour and approximately four periods of oscillation are included. Confirmation of the time periodicity of the solution is provided in the phase plane plot in figure 9.7.b: the two distinct loops correspond to the small and large amplitude superimposed oscillations of the two time signals. We can conclude that the dynamics of the system lead to the formation of periodic strips similar to the ones found by Craster & Matar (2005). However, due to the presence of flow, these strips move at a constant speed and they undergo time-periodic modulations of small amplitude and high frequency.

9.3. Effect of the flux

In this section the effect of the flux on the flow is examined. Figure 9.8 gives a comparison of the real and imaginary part of the growth rate s for three different values of the flux. The real parts are exactly the same in all three cases while the imaginary parts are different. It follows that in the linear regime different values of the flux $\tilde{Q}$ only affect the speed of the wave ($v_p = -Im\{s\}/k$, where v_p is the phase velocity). However, once nonlinear effects kick in, a higher flux leads to a smaller wave amplitude as can be seen from figures 9.9 and 9.10 where we compare the profiles of the numerical solutions for four different values of the flux $\tilde{Q}$ at large times.

Figure 9.9 shows the profiles of the interface and of the charge for different values of $\tilde{Q}$. When $\tilde{Q} = 0$ (dotted line) we get exactly the same patterns as were found by Craster & Matar (2005). For a small flux $\tilde{Q} = 0.1$ (dot-dashed line) the patterns are still present but they are slowly being swept down the channel with phase speed $v_p = 0.0886$ (see

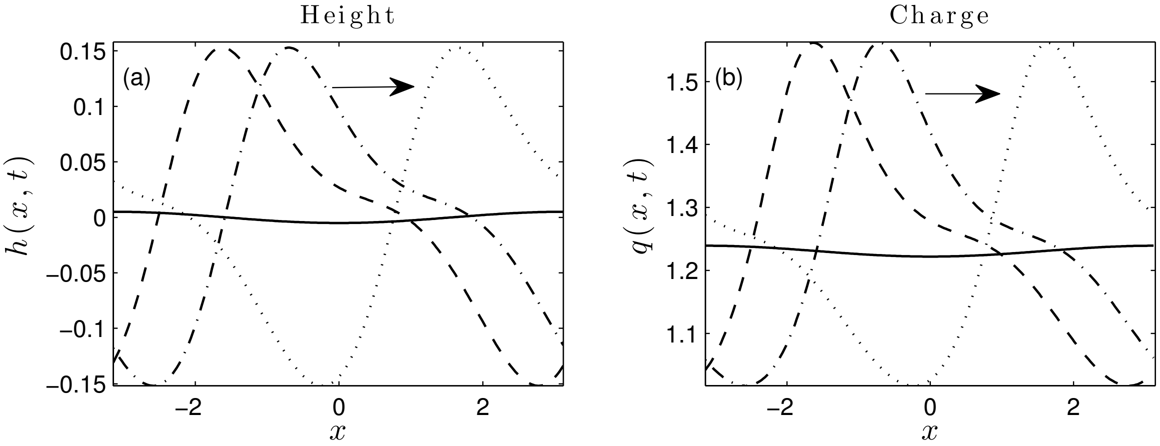

Figure 9.6. Solutions of (7.98-7.99) i.e. case B at $t = 0$ (solid line), $t = 340$ (dashed line), $t = 680$ (dot dashed line) and $t = 1000$ (dotted line). Parameters: $\beta = 0.55$, $z = 1$, $\bar{\epsilon}_1 = 1$, $\bar{\epsilon}_2 = 2$, $m_1 = 1$, $m_2 = 1$, $S_1 = 100$, $S_2 = 1000$, $\delta = 10^{-1}$. Parameters in the initial condition: $h_0 = q_0 = -0.01$, $k = 1$.

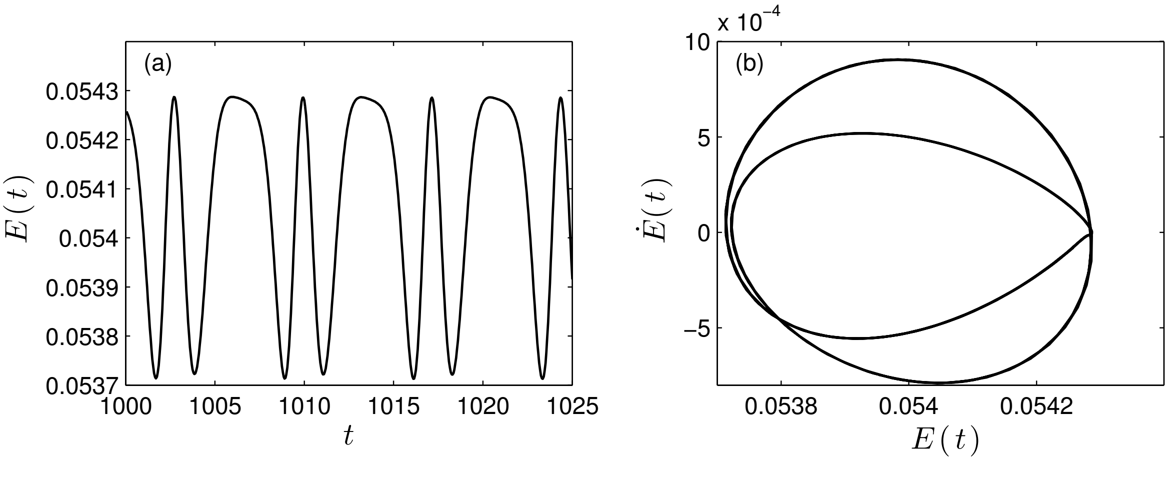

Figure 9.7. Energy $E(t)$ plotted as time is varied for case B with the same parameters as figure 9.6 (b) phase planes of the energy: E versus dE/dt.

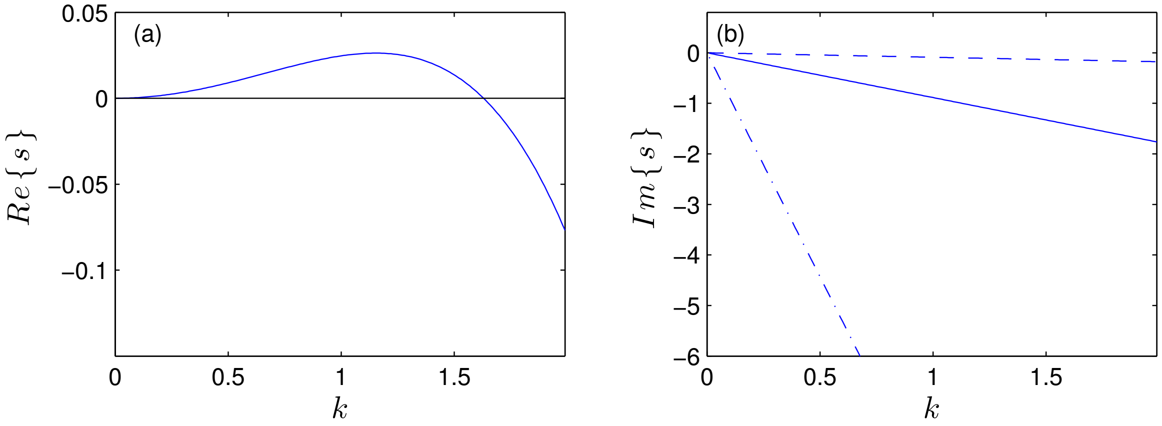

Figure 9.8. Linear stability three different fluxes: $\tilde{Q} = 0.1$ (dashed line), $\tilde{Q} = 1$ (solid line) and $\tilde{Q} = 10$ (dot dashed line). Parameters: $\beta = 0.55$, $z = 1$, $\bar{\epsilon}_1 = 1$, $\bar{\epsilon}_2 = 2$, $m_1 = 1$, $m_2 = 1$, $S_1 = 100$, $S_2 = 1000$.

fig.9.8b). For a larger flux $\tilde{Q} = 1$ (dashed line) the flow is strong enough to prevent the formation of large amplitude structures and for an even larger flux $\tilde{Q} = 10$ the flow is so strong that the interface stays nearly flat.

Figure 9.10 gives a comparison between the minima of the height for different values of the fluxes. We see that for early times the value of h_{min} is the same for any value of the flux as predicted by linear theory (see fig.9.8a). At later times nonlinear effects come into the system and it is found that the higher the flow the smaller the patterns. We conclude that higher fluxes tend to break electrically-induced patterns.

9.4. Summary of research

We have examined the flow of two fluids between two flat electrodes and the influence of the electric field on the fluid-fluid interface. Two coupled nonlinear evolution equations are derived for the moving interface and the interfacial charge. We have investigated the linear stability for the two cases of large and small electrical permittivity and for each case there exists a band of unstable wavenumbers. The maximum growth rate increases with increasing electrical permittivity but increasing the overall flow rate does not appear to influence the value of the critical wave number.

The evolution equations are solved using a numerical scheme based on spectral methods. The results show that initially small perturbations grow in time and the constant flux gives rise to waves that undergo time-periodic modulations and travel at constant speed.

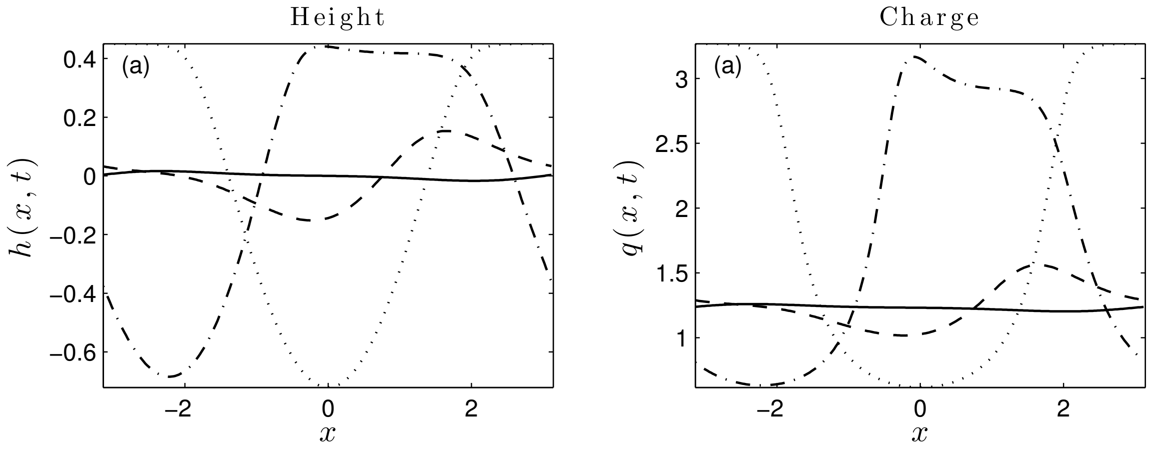

Figure 9.9. Solutions of (7.98-7.99) at $t = 1000$ for different values of the flux: $Q = 0$ (dotted line), $Q = 0.1$ (dot-dashed line), $Q = 1$ (dashed line) and $Q = 10$ (solid line). Parameters in the initial condition: $h_0 = q_0 = -0.01$, $k = 1$.

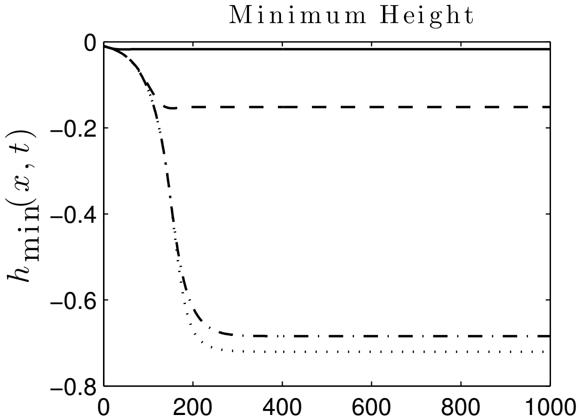

Figure 9.10. Minimum height for $\tilde{Q} = 0$ (dotted line), $\tilde{Q} = 0.1$ (dot-dashed line), $\tilde{Q} = 1$ (dashed line) and $\tilde{Q} = 10$ (solid line).

Good agreement is found between the linear stability analysis and numerical predictions for the growth rate.

Although the flux does not seem to influence the growth of perturbations in the linear regime, numerical results show that at later times larger wave amplitudes are associated with smaller fluxes. It is concluded that higher overall flow rates are more likely to "break" the electrically induced patterns found by Craster & Matar (2005) in the zero flow case.

10. Two layer flow of thin perfect dielectric films over one corrugated electrodes

10.1. Evolution equations

In this chapter we consider the behaviour of the interface between two perfect dielectric fluids flowing between two electrodes that are held at constant voltages. The top electrode is flat and parallel to the undisturbed interface while the bottom electrode has a corrugation given by the function $z(x)$. The setup of the system is shown in figure 7.3 with β taken to be constant. We consider the case of large permittivity (case B) and since the fluids are assumed to be perfect dielectrics we only have one evolution equation for the interfacial height:

$$h_t + \left\{ \frac{D_3}{6m_2} \left[D_4 p_{2x}^{(0)} + 3m_2 f_2 \right] \right\}_x = 0 \tag{10.1}$$

We proceed to determine the stability and the numerical solutions of the evolution equation of the interface. The initial condition used in our computations is

$$h(x,0) = h_0 \cos(kx), \tag{10.2}$$

with $h_0 = 0.01$ (or $h_0 = 0$ when stated) and different values of the wavenumber k. The initial condition (10.2) is $\frac{2\pi}{k}$-periodic and typically the evolution equation (10.1) is also solved on a periodic domain of length $2\pi/k$. We have also carried out computations on longer domains that are integer multiples of $2\pi/k$, in order to investigate the possibility of subharmonic instabilities. The numerical integration is carried out to large enough times to enable identification of the types of solutions that emerge. The flat lower boundary case is analysed first: a linear stability analysis is done and it is used to validate numerical results. The evolution equation is then solved numerically for the wavy boundary case and two different types of behaviour are found. We then attempt to classify these two types with the help of the linear stability analysis for the flat case and an analytical solution is found for one of the two types of solutions. Finally, we look at a system with a large amplitude sinusoidal electrode and analyse its stability with the help of Floquet theory. The results presented in this chapter have been submitted for publication and are currently under review (Dubrovina *et al.*, 2016).

10.2. Linear stability for flat boundaries

When the lower boundary is wavy, the base state is non-uniform and its stability is not amenable to a normal mode analysis - Floquet theory is used instead as detailed later in Section 10.8. To gain an understanding of the underlying instabilities present, in what follows we perform a linear stability analysis for a flat lower electrode placed at $y = -Z_c = 0.9$. In this case the evolution equation is linearised about the steady state $h \equiv 0$ and solutions proportional to $\exp(ikx + st)$ are sought leading to a dispersion relation for the growth rate s as a function of the wavenumber k. Figure 10.1 shows the real part of s (i.e. the growth rate - see panel (a)) and its imaginary part (i.e. the frequency - panel (b)), for a typical set of physical parameters with an imposed dimensionless voltage $V_b = 3$, a flow rate $\tilde{Q} = 0.1$, a unit channel height described by $\beta = 1$, relative permittivities $\bar{\epsilon}_1 = 1$ and $\bar{\epsilon}_2 = 5$, and equal viscosities so that $m_1 = m_2 = 1$ (in order to reduce the large set of parameters that characterises our problem, we proceed with equal viscosities throughout the rest of the chapter). The results show that the flow is long wave unstable with a finite band of unstable modes with short waves (large k) damped. In addition, the imaginary part of s is nonzero and in fact linear in k, hence linear waves are predicted to travel with a constant phase velocity. Hence we can expect that after nonlinear saturation the emerging structures will tend to travel in the direction of increasing x. The precise nature of the emerging coherent structures is undertaken next through detailed numerical computations.

10.3. Flat lower boundary: formation of travelling wave structures

We begin our numerical studies by considering the case when the lower electrode is flat and placed at $y = -Z_c$ ($Z_c > 0$ is a constant). Figure 10.2.a shows the interfacial deformation $h(x, t)$ at four consecutive relatively large times (ensuring transients have died out) for the case $Z_c = 0.9$ (the dimensionless channel thickness is 1.9 units) - the other parameters are the same as those of figure 10.1 so that the $k = 1$ mode (a

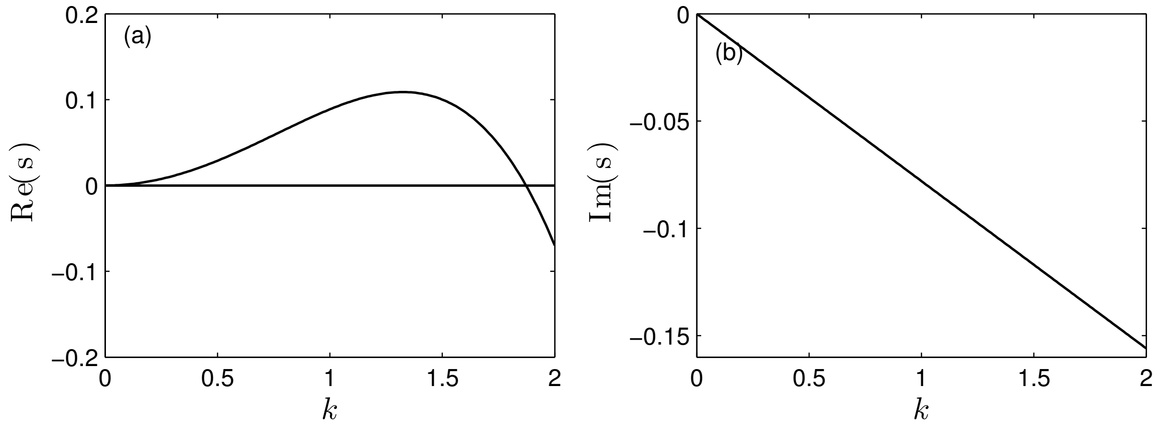

Figure 10.1. Linear growth rate for flat bottom walls at $y = -0.9$ and for an applied dimensionless voltage $V_b = 3$. Other parameters are the dimensionless flow rate $\tilde{Q} = 0.1$, $\beta = 1$ (i.e. the upper wall is at $y = 1$), dimensionless permittivities $\bar{\epsilon}_1 = 1$ and $\bar{\epsilon}_2 = 5$, and viscosity ratio $m_2 = 1$.

perturbation of wavelength 2π) is unstable. The solid curve corresponds to $t = 200$, the dashed curve to $t = 200.6$, the dot-dashed curve to $t = 201.2$, and the dotted curve to $t = 201.8$. The viscosities of the two fluids are chosen to be the same in order to exclude any viscosity stratification instabilities (see Yih (1967)) and isolate electrohydrodynamic instabilities - in the absence of a field, $V_b = 0$, the flow is stable and $h \equiv 0$. The linear instabilities saturate to what appear to be nonlinear travelling waves that span almost the whole extent of the channel; the interface approaches the boundaries but remains at a small but finite distance from them for the whole duration of the computation (such behaviour has been confirmed for much longer computations with times as large as 10^4 and different parameters). This is in contrast to situations with no background flow (i.e. $\tilde{Q} = 0$ in our notation) where electrostatic instabilities lead to interfacial contact with the wall - see for example the theoretical studies of Craster & Matar (2005), Tseluiko & Papageorgiou (2007*b*), Tseluiko & Papageorgiou (2007*a*), Barannyk *et al.* (2015*a*) for both planar and cylindrical geometries as well as fields acting parallel to the undisturbed interface, as well as the experiments of Schaffer *et al.* (2001). In figure 10.2.b we quantify these observations in the presence of flow by monitoring the minimum distance of the interface to the walls as $\tilde{Q}$ varies - to fix matters we do this for different runs and calculate minimal approaches at a large time $t = 300$. The results indicate that the minimum distance increases as $\tilde{Q}$ increases thus confirming the earlier findings that there is a flow-induced stabilisation of touchdown events. As mentioned already, when $\tilde{Q} = 0$ we expect

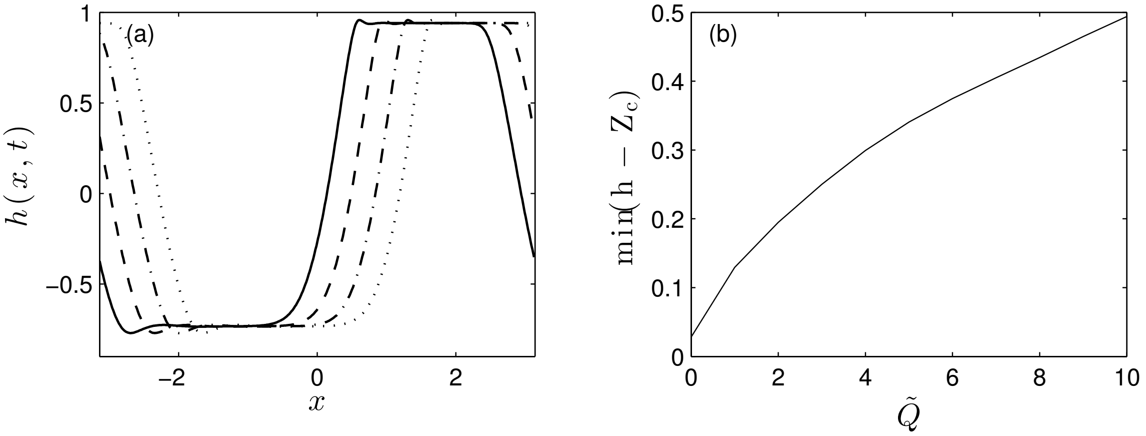

Figure 10.2. (a) Interface $h(x,t)$ at $t = 200$ (solid curve), $t = 200.6$ (dashed curve), $t = 201.2$ (dot dashed curve) and $t = 201.8$ (dotted curve). Walls are at $y = -0.9$ ($Z_c = 0.9$) and $y = 1$ ($\beta = 1$). Other parameters are, $\tilde{Q} = 1$, $V_b = 3$, $\bar{\epsilon}_1 = 1$, $\bar{\epsilon}_2 = 5$, $m_2 = 1$. (b) Minimum distance between the interface and the lower boundary at time $t = 300$ as the flow rate $\tilde{Q}$ varies.

asymptotic thinning with touchdown as $t \to \infty$, and the finite value of approximately 0.02 given in figure 10.2.b reflects the fact that t is not large enough - larger t would lead to smaller values (see Craster & Matar (2005), Tseluiko & Papageorgiou (2007*b*) for example).

Even though the solutions presented in figure 10.2.a appear to be nonlinear travelling waves, closer analysis of the data establishes that they are in fact travelling time-periodic waves similar to the ones observed in the previous chapter. To accurately predict such dynamics we make use of the energy of the solution (the L^2-norm of h) defined as

$$E(t) = \int_{-\pi/k}^{\pi/k} h^2(x,t)\, dx, \tag{10.3}$$

As before, we also calculate dE/dt in order to construct phase planes presented below. Panels 10.3.a-b give the evolution of $E(t)$ for $\tilde{Q} = 10$ and 100, respectively. In both cases we observe time periodic behaviour (approximately five periods of oscillation are included in each case) with the period decreasing as $\tilde{Q}$ increases. In fact the period for $\tilde{Q} = 10$ is approximately equal to 0.8 time units while that for $\tilde{Q} = 100$ is approximately 0.08 time units, a decrease by a factor of 10 indicating that the frequency of oscillation is proportional to $\tilde{Q}$ when this becomes large - an asymptotic theory along with compar-

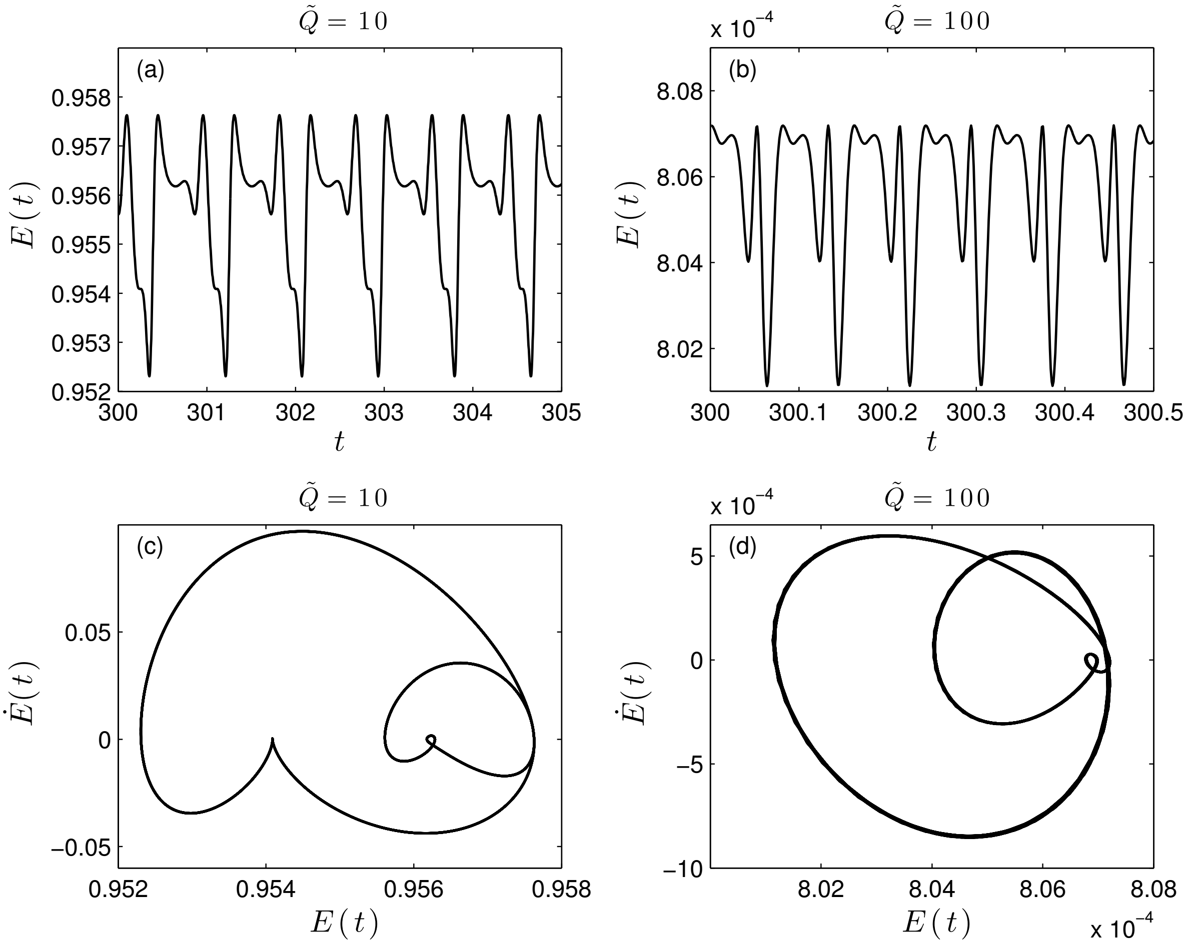

Figure 10.3. Time evolution of the energy $E(t)$ for (a) $\tilde{Q} = 10$ and (b) $\tilde{Q} = 100$. Phase planes of the energy: E versus dE/dt for (c) $\tilde{Q} = 10$ and (d) $\tilde{Q} = 100$. All other parameters are the same as in figure 10.2.

isons with the numerical data is presented in Section 10.10 for the more complicated case of wavy lower boundaries. Another feature of the results in figures 10.3.a-b is the small amplitude of the time dependent oscillations about a mean value, with these amplitudes again decreasing as $\tilde{Q}$ increases. Confirmation of the time periodicity of the solution is provided in the phase plane plots in panels 10.3.c-d that have been produced for longer time intervals than those shown in panels (a) and (b). The two distinct loops correspond to the small and large amplitude superimposed oscillations of the two time signals.

We conclude that the dynamics in channels with flat walls lead to the formation of periodic "pillars" similar to the ones found experimentally by Schaffer *et al.* (2001) and theoretically by Craster & Matar (2005) in the absence of a background flow. However due to the presence of flow these structures travel down the channel and also undergo time-periodic modulations while keeping a finite separation distance from the walls. These findings are in agreement with the results described in the previous chapter for the case when the two fluids are leaky dielectrics.

10.4. Wavy lower boundary: interfacial response to non-uniform confinement geometries

In this section we present results of computations of (10.1) for a sinusoidal lower boundary given by

$$y = -z(x) = -Z_c + d_b \cos(k_b x). \tag{10.4}$$

The initial condition is (10.2) as before - recall that $2\pi/k$ selects the length of the computational domain. The parameter d_b measures the wall amplitude and k_b its wavenumber. When $d_b = 0$ we reduce to the flat case and we will use the linear stability results of Section 10.2 to guide the computations when $d_b \neq 0$. In particular for a given set of parameters the linear theory predicts a critical wavenumber k_c below which instability is supported and we investigate the two cases (a) $k < k_c$ and (b) $k > k_c$ to show that they delineate distinct types of large time solutions. In case (b) the interface very quickly reaches a steady state and adopts the wavenumber k_b of the wavy boundary but with a much smaller amplitude; in case (a) we find travelling time periodic structures that are similar to those for the flat boundary case (see figure 10.2 for example), but are modulated due to the wavy confining wall and "squeeze" past it. Typical results are given in figure 10.4 for wall parameters $k_b = 4$ and $d_b = 0.1$ and mean position $y = -Z_c = -0.9$; the other parameters are $\tilde{Q} = 0.1$ and $V_b = 3$. The results in panel 10.4.a correspond to an initial condition having $k = 2$ (i.e. twice the wavelength of the wavy wall) which

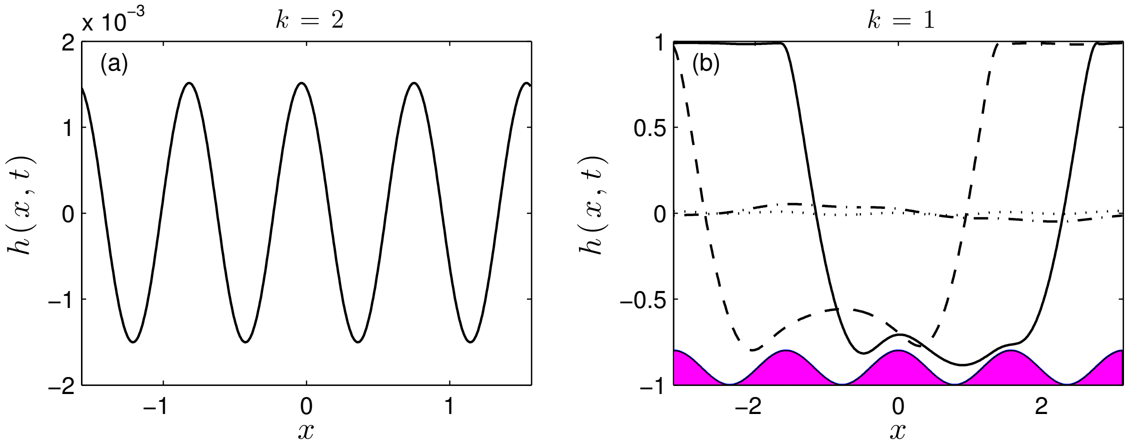

Figure 10.4. Flow past a sinusoidal wavy wall of mean position $y = -0.9$ and having amplitude $d_b = 0.1$ and wavenumber $k_b = 4$; the scaled relative permittivities are $\bar{\epsilon}_1 = 1$ and $\bar{\epsilon}_2 = 5$, the flow rate is $\tilde{Q} = 0.1$ and the lower wall potential $V_b = 3$. (a) Initial condition (10.2) with $k = 2$. Interface $h(x,t)$ shown at time $t = 100$ after the solution has reached steady state. (b) Longer initial perturbation having $k = 1$. Interface $h(x,t)$ at $t = 1$ (dotted line), $t = 25$ (dot dashed line), $t = 75$ (dashed line) and $t = 100$ (solid line). The shaded area represents the lower boundary.

is larger than k_c for the chosen parameters and so the flow reaches a steady state (h is shown at $t = 100$ here) with the interface inheriting the pattern of the wavy wall (but with a smaller amplitude of roughly 1.5×10^{-3} compared with $d_b = 0.1$). In panel 10.4.b we set $k = 1 < k_c$ and observe that the unstable longer wavelength perturbation grows nonlineary to travelling pillar like structures found for flat walls, but at the same time sweeps over the topography modulating its shape as it moves downstream. Profiles are shown at times ranging from $t = 1$ (dotted curve) to $t = 100$ (solid curve) and as found previously for flat walls, throughout the evolution the interface gets close to the upper and lower walls but does not touch them.

The results presented in figure 10.4 can be understood with a more detailed comparison with linear theory for flat walls. We can anticipate that as long as the wall amplitude d_b is not large (in the results $d_b = 0.1$) the bifurcation from a non-uniform steady state to a more complicated modulated travelling wave, should correlate with flat wall linear theory. This is confirmed in the results presented in figure 10.5. We fix $k = 1$ in the initial conditions and compute solutions for a wavy wall having $d_b = 0.1$ and $k_b = 1$ at increasing values of V_b starting from $V_b = 1.5$. We quantify the solutions by estimating a wave speed c that measures the streamwise motion of the interfacial wave (the solution

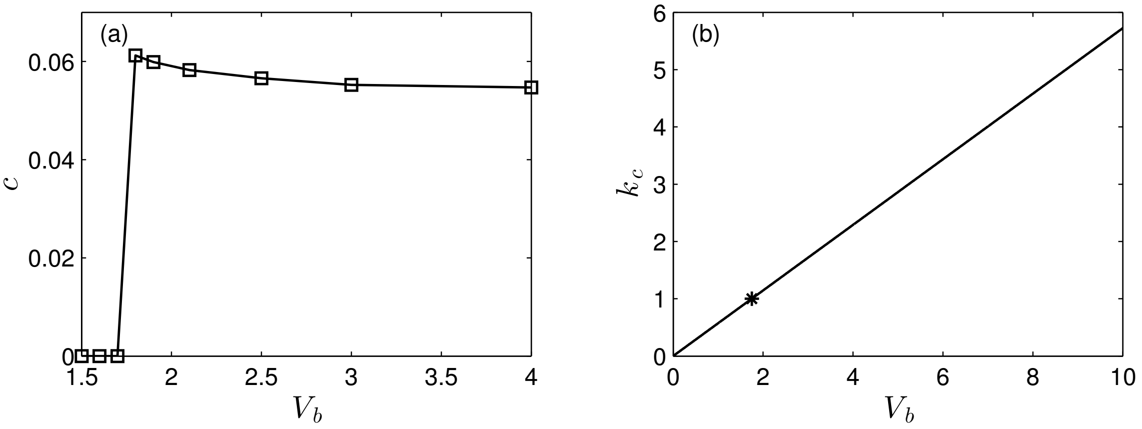

Figure 10.5. (a) Estimated interfacial wave speeds c for flows over a sinusoidal boundary with $d_b = 0.1$, $k_b = 1$ and $Z_c = 0.9$; (b) Neutral stability curve showing the critical wavenumber k_c as a function of V_b from linear theory with a flat bottom wall. The star corresponds to wavenumber $k_c = 1$ and $V_{crit} = 1.75$. The relative permittivities are $\bar{\epsilon}_1 = 1$ and $\bar{\epsilon}_2 = 5$ and the flow rate is $\tilde{Q} = 0.1$.

is not exactly a travelling wave of permanent form - it is time periodic and travelling). This is done by following trajectories in the $x - t$ plane of given points on the interface and defining a speed by estimating the slope of given trajectories using least squares regression. The results are given in figure 10.5.a and it is clearly seen that a bifurcation from stationary waves (these are non-uniform steady states) to travelling modulated waves takes place at a critical value $V_b \approx 1.5$. A direct comparison with the flat case linear theory is possible from the critical stability curve in $k_c - V_b$ space depicted in figure 10.5.b; in fact we find that k_c varies linearly with V_b and at $k_c = 1$ the critical value V_{crit} above which instability occurs is given by $V_{crit} = 1.75$, in complete agreement for the bifurcation value from steady to time modulated travelling waves for wavy walls. We conclude that there is a direct correlation between the stability of the flat and wavy wall cases; the critical voltage V_{crit} found for the flat case corresponds to the value V_b that marks the transition from steady state solutions to time modulated travelling waves.

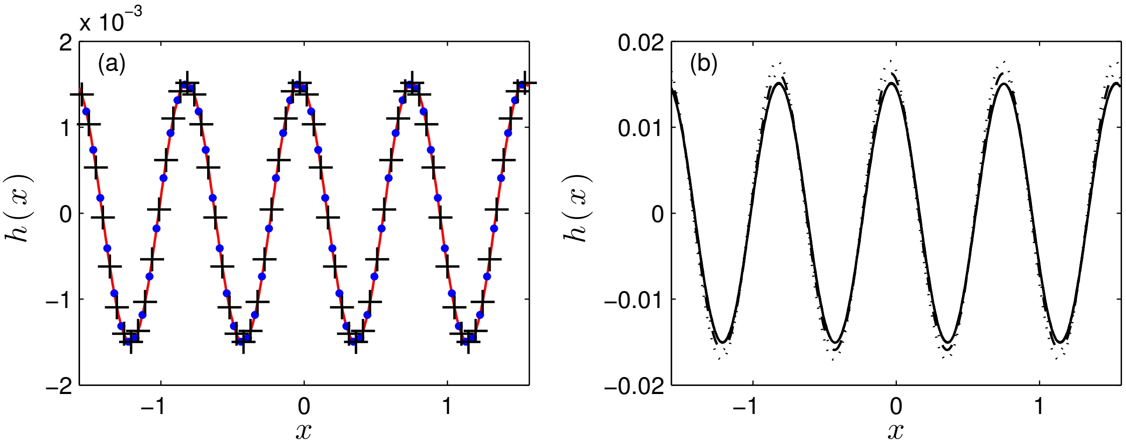

Figure 10.6. (a) Comparison between the full time dependant numerical solution (solid line), the numerical solution of the steady state ODE (crosses) and the analytical solution (dots) with wall amplitude $\varepsilon = 0.1$. (b) Comparison between the analytical solution (solid line) and the numerical solutions $h(x)/\varepsilon$ for $\varepsilon = 0.1$ (dashed line), $\varepsilon = 0.2$ (dot-dashed line) and $\varepsilon = 0.3$ (dotted line). Same parameters as in figure 10.4(a).

10.5. Non-uniform steady states for different wall amplitudes

The transition between the two different types of solutions for the wavy boundary problem was described above and quantified using linear theory for flat walls. We now focus on calculating steady states of the evolution equation (10.1) by solving

$$\left\{ \frac{D_3}{6m_2} \left[D_4 p_{2x}^{(0)} + 3m_2 f_2 \right] \right\}_x = 0 \tag{10.5}$$

Equation (10.5) is solved using centred finite differences to discretise derivatives and a Newton-Kantorovich method to solve the resulting set of nonlinear algebraic equations. As a check the solutions were compared with those given by the time dependent code at least for values of $V_b < V_{crit}$ where the solutions are stable - for completeness this is included in figure 10.6.a for $d_b = 0.1$, $k_b = 4$, $\tilde{Q} = 0.1$ and $V_b = 3$ and it is seen that agreement is excellent.

10.6. Analytical solution for small wall waviness

The steady states presented in §10.5 were calculated numerically for arbitrary wall waviness and in what follows we proceed analytically and construct asymptotic solutions valid for small wall perturbations. We can do this by writing the lower wall as $z(x) = Z_c + \varepsilon Z(x)$ where $\varepsilon \ll 1$, and looking for an asymptotic solution of the form $h(x) = \varepsilon H_0(x) + O(\varepsilon^2)$. Substituting these into (10.5) gives, to leading order

$$AH_0 + BH_{0x} + CH_{0xxx} = -DZ - EZ_x, \tag{10.6}$$

where A, B, C, D and E are constants that depend on the physical parameters in the problem (they are found as needed by using the symbolic manipulator Maple). To fix things we proceed with a sinusoidal wall perturbation of wavelength $2\pi/k_b$ and specifically take $Z(x) = -\cos(k_b x)$ in order to enable comparisons with nonlinear steady states computed for wavy wall perturbations given by (10.4). It follows that the general solution of equation (10.6) is given by

$$H_0(x) = \sum_{i=1}^{3} C_i \mathrm{e}^{\lambda_i x} + C_4 + Re(p)\cos(kk_b x) - Im(p)\sin(kk_b x), \tag{10.7}$$

where C_i, $i = 1, 2, 3, 4$ are constants and λ_i, $i = 1, 2, 3$ are the roots of $A + B\lambda + C\lambda^3 = 0$. The complex number p is given by

$$p = \frac{D + ikk_b E}{A + ikk_b B - i(kk_b)^3 C}.$$

The constants C_i, $i = 1, 2, 3, 4$ corresponding to the homogeneous solution, are found by imposing periodic boundary conditions over $x \in [-\pi/k, \pi/k]$ and the conservation of mass integral constraint on H_0

$$\int_{-\pi/k}^{\pi/k} H_0(x)dx = 0. \tag{10.8}$$

In the special case when k_b, k are integers with $k_b \neq \lambda_i$ for $i = 1, 2, 3$, it can be shown that the roots of $A + B\lambda + C\lambda^3 = 0$ are such that $Re(\lambda) \neq 0$ and hence the homogeneous contribution to the solution cannot be spatially periodic. In such cases the expression for the interface simplifies to

$$H_0(x) = Re(p)\cos(kk_b x) - Im(p)\sin(kk_b x). \tag{10.9}$$

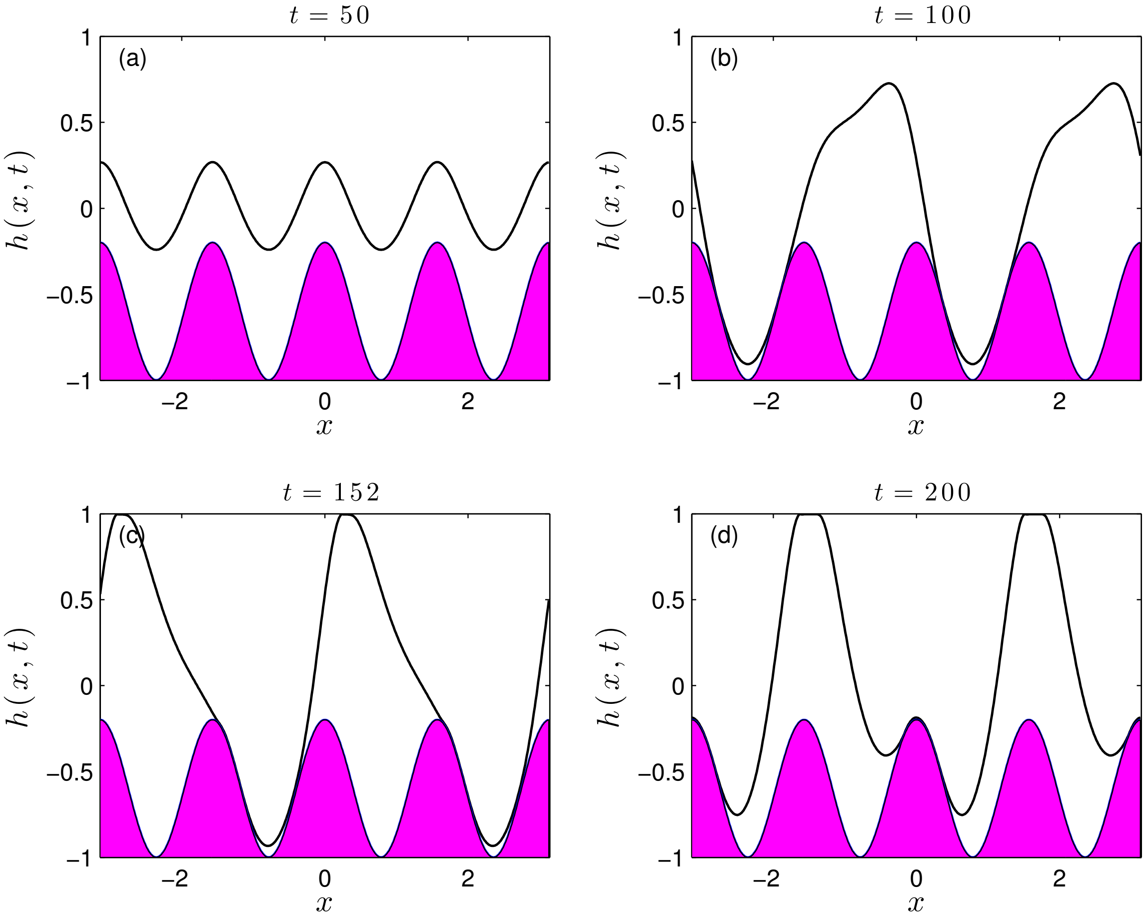

Figure 10.7. Interface $h(x,t)$ at final times (a) t=50, (b) t=100, (c) t=152 and (d) t=200. Other parameters are $V_b = 7$, $\tilde{Q} = 0.0345$, $d_b = 0.4$, $k_b = 4$, $Z_c = 0.6$, $\beta = 1$, $\bar{\epsilon}_1 = 1$, $\bar{\epsilon}_2 = 2$, and $m_2 = 1$.

In figure 10.6.a we superimpose the leading order analytical solution (10.9) with $\varepsilon = 0.1$ along with the full time dependent numerical solution integrated to steady state, and the numerical solution of (10.5). Panel 10.6.b considers larger wall amplitudes $\varepsilon = 0.2$, 0.3 and it can be seen that the leading order solution (10.9) is reasonably accurate even beyond its expected range of validity. Note that inclusion of ε^2 corrections is expected to improve the agreement as found in the related studies of falling films over topography, e.g. Tseluiko *et al.* (2008*b*).

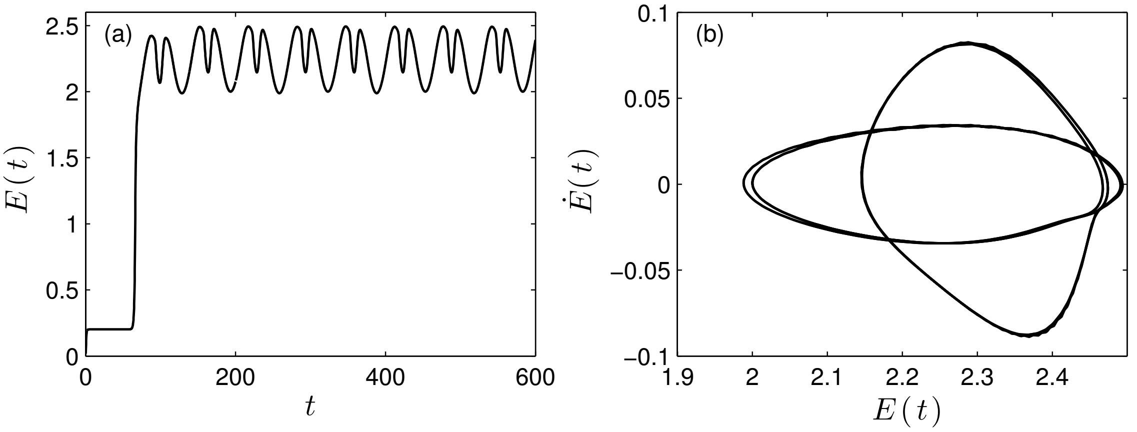

Figure 10.8. (a) Time evolution of the energy $E(t)$ of the solution presented in figure 10.7. (b) Phase plane of the energy: E versus dE/dt for times between $t = 200$ and $t = 600$.

10.7. Large amplitude sinusoidal boundary

In this section we examine the flow through highly constricted channels with wavy boundaries that occupy nearly half of the channel width. In the computations described next, the initial condition is chosen to be $h(x, 0) = 0$. In the absence of a field (or for weak fields) we would expect to reach the non-uniform steady states given by solutions of (10.5). For large wall amplitudes, an additional physical feature of the steady states is the formation of vortices in the troughs that are now deep enough to accommodate them - see below for numerical results; for related single phase problems such as falling films over sinusoidally corrugated walls see the experiments of Pollak & Aksel (2013*a*). At large enough values of the voltage parameter V_b, the unsteady numerical simulations predict that the interface initially reaches a state state, but eventually instability sets in with the dynamics transitioning to what we have termed “walking behaviour”. This behaviour can be mainly characterised by three stages: first the flow looses stability and parts of the interface get attracted to the lower wavy wall and other parts to the flat upper wall; this transient stage continues with the interface going into the troughs and over the crests in very close proximity to the wavy wall, with regions ahead (or behind) reaching the upper wall; finally the dynamics enters a final state that resembles a travelling wave parts of which hug the lower wavy wall and other parts the upper wall. It is quite striking to discover that the resulting nonlinear dynamics are time periodic for a large range of parameters that were studied. Representative computations are provided in figure 10.7 for $V_b = 7$, $\tilde{Q} = 0.0345$, and a wavy wall with mean position $y = -0.6$, wall amplitude $d_b = 0.4$ and wavenumber $k_b = 4$. The scaled channel height is $y = 1(\beta = 1)$ and the scaled relative permittivities are $\bar{\epsilon}_1 = 1$, $\bar{\epsilon}_2 = 2$ (recall that $m_2 = 1$). Panel 10.7.a shows the solution close to its unstable steady state (this is at dimensionless time $t = 50$), while panels 10.7.b-d at times $t = 100$, 152, 200 depict solutions from the three stages described above. For $t > 200$ the dynamics enters the time-periodic attractor mentioned earlier and this is quantified further in figure 10.8 that considers the flow from $t = 200$ to $t = 600$. Panel 10.8.a shows the evolution of the energy norm $E(t)$ from $t = 0$ until the final time $t = 600$; it is seen that the solution quickly reaches a nonuniform steady state (this is characterised by the the constant value $E(t) \approx 0.2$ until approximately $t = 70$), and then rapidly looses stability to a much higher energy state that eventually becomes time-periodic. Conclusive evidence of the time-periodicity is provided in panel 10.8.b that constructs the energy phase plane which is seen to be a closed curve consisting of four almost congruent loops - inspection of panels (a) and (b) shows that there are four energy minima and four maxima over one period and the period is approximately equal to 130 time units.

In order to inspect the flow more thoroughly and in particular to obtain insight regarding the vorticity and subsequent mixing capabilities in such systems, we write the fluid velocity in the lower layer (analogously in the upper layer if we wish) in terms of the streamfunction $\psi(x, y)$ such that $u_2^{(0)} = \psi_y$ and $v_2^{(0)} = -\psi_x$. Using the expression for the horizontal fluid velocity given by equation (7.97) readily yields

$$\psi(x, y, t) = \frac{p_{2x}^{(0)}}{2m_2}\left(\frac{y^3}{3} - z(x)^2\, y\right) + f_2\left(\frac{y^2}{2} + z(x)\, y\right) + c_1(x), \tag{10.10}$$

where $c_1(x)$ is found by setting $\psi(x, -z(x), t) = 0$, i.e. the lower wall is defined to be a zero streamline. Figure 10.9 provides the instantaneous streamlines of the flow depicted in figure 10.7, at four consecutive times $t = 96$, 98, 100, 106 (the bar on the right shows the value of ψ in the contour plots). As described earlier and seen in figure 10.9, a distinct feature of the flow, at a fixed time, is that parts of the interface are in close proximity to troughs while ahead (behind) of these regions the interface climbs over the hump to reach the upper wall. What is interesting is that every time the interface goes over the wall humps and the lower fluid extends up to the upper wall, two strong counter rotating vortices form in close proximity to each other - see for example panel 10.9.d. As time increases these vortices get swept along downstream by the flow. A more detailed depiction of this flow feature is provided in figure 10.10 that shows an enlargement in the vicinity of the wall hump where the vortices are and at times before and after the hump.

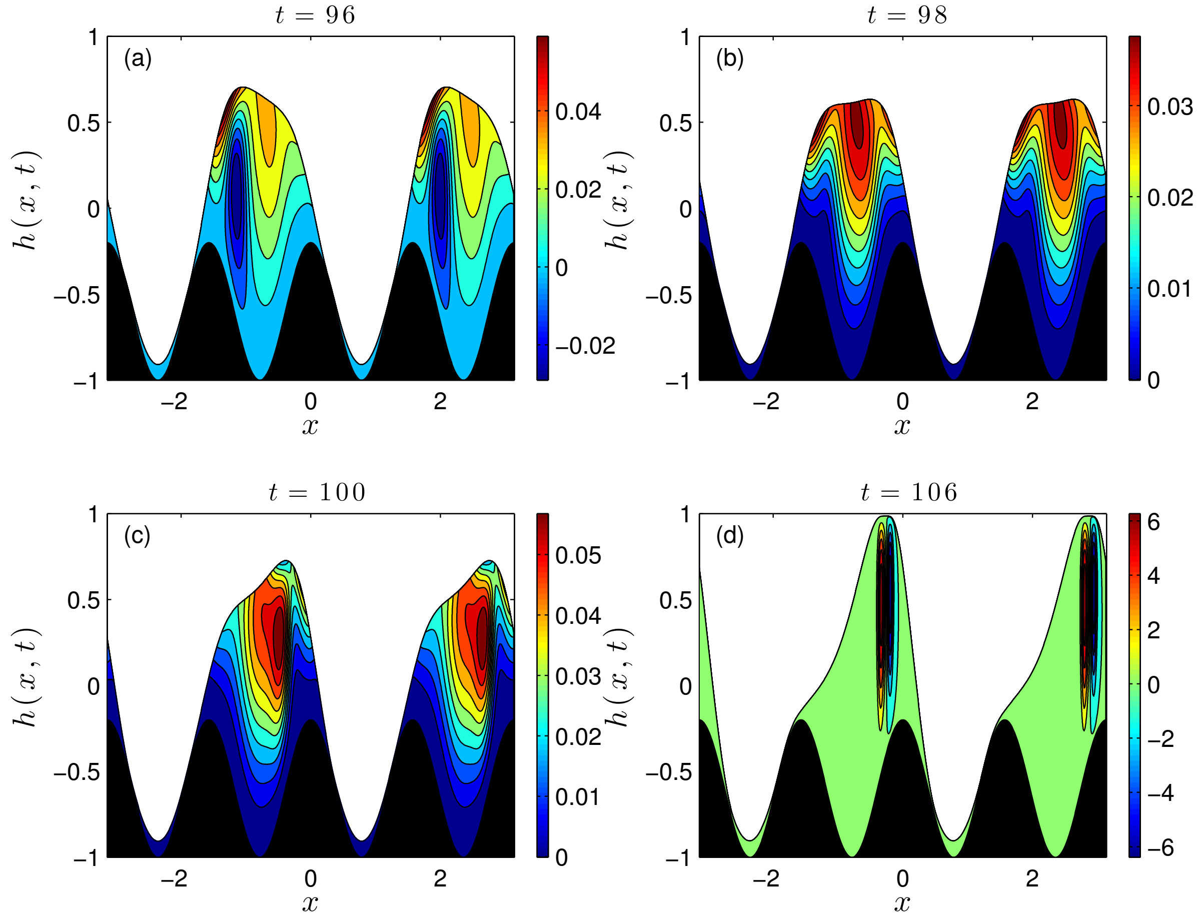

Figure 10.9. Instantaneous streamlines at (a) $t = 96$, (b) $t = 98$, (c) $t = 100$ and (d) $t = 106$. All other parameters as in figure 10.7.

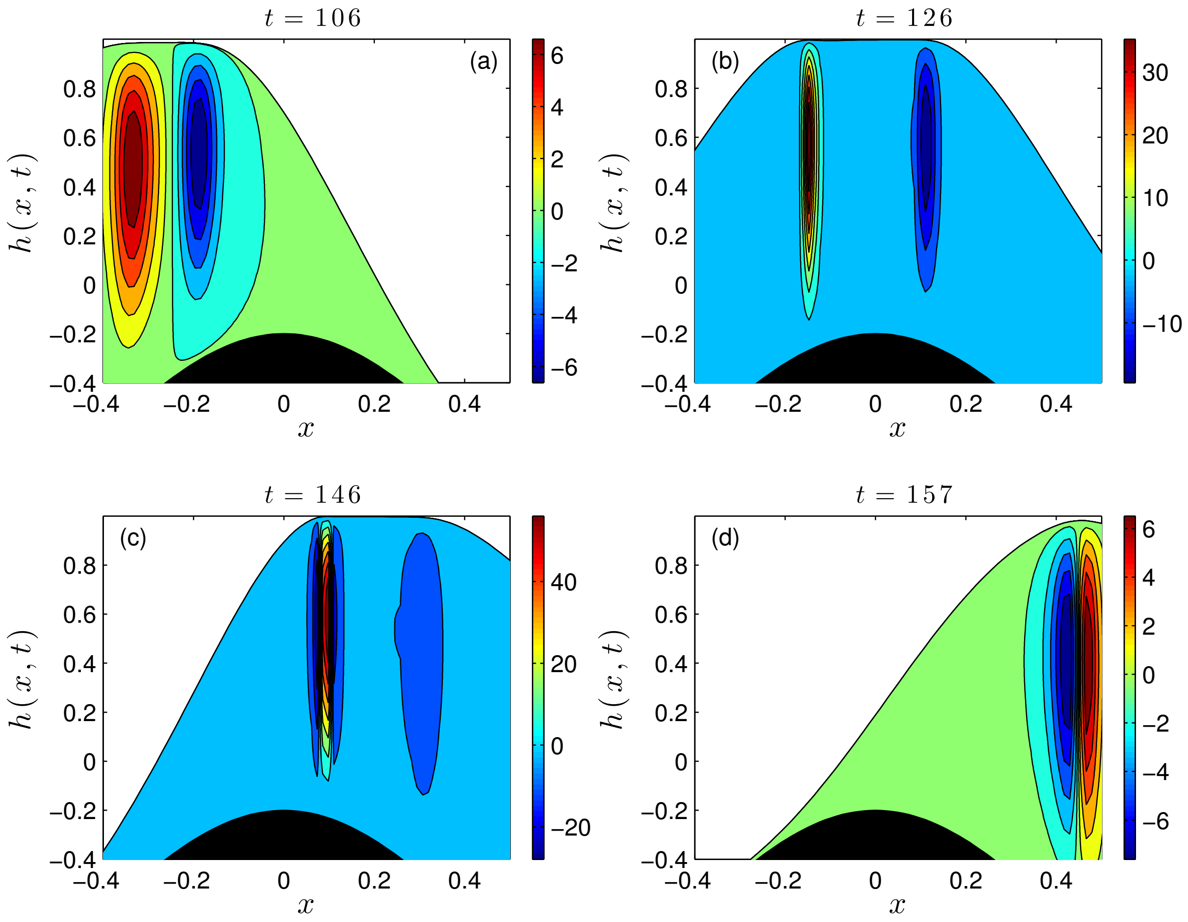

Figure 10.10. Instantaneous streamlines at (a) $t = 106$, (b) $t = 126$, (c) $t = 146$ and (d) $t = 157$. All other parameters as in figure 10.7.

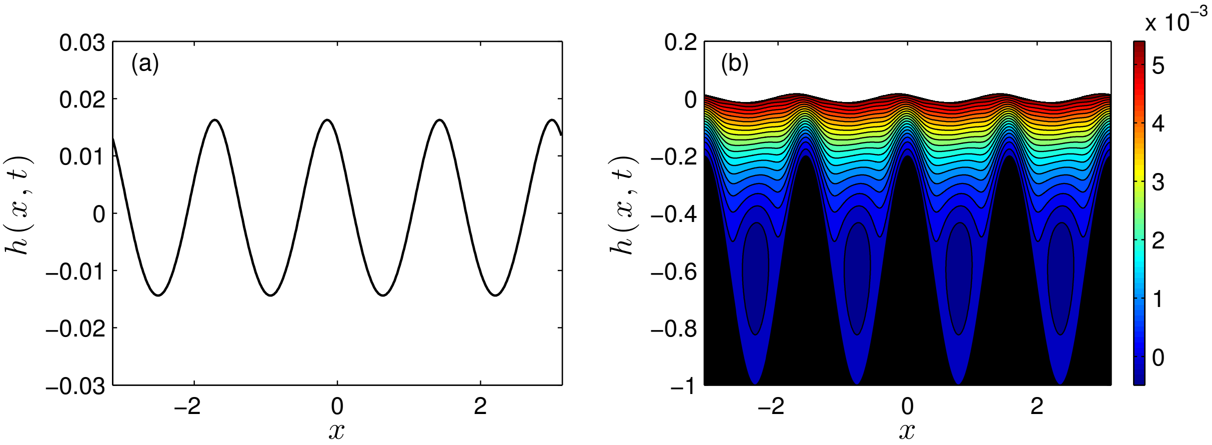

Figure 10.11. (a) Interface $h(x, t)$ and (b) streamlines at time t=100. Parameters are the same as in figure 10.7 but with a different voltage $V_b = 2$.

For example, the vortices at times $t = 126$ and $t = 146$ that are just over the hump, are seen to be more compact and the stream function attains much larger values compared with the other two times when the vortices are either behind or ahead of the hump. In turn, the vorticity generated is large and it may be possible to exploit such phenomena to induce electrostatically induced mixing at low Reynolds numbers and small flow rates.

We conclude this section by considering the same large amplitude wavy boundary as above but now take a smaller value $V_b = 2$. In such cases the interface reaches a steady state with vortices and flow recirculation taking place in the troughs, with the remaining flow unidirectionally moving over the peaks. Numerical results are given in figure 10.11 with panel (a) showing the interface at $t = 100$ after steady state has been reached, and panel (b) shows the streamlines of the corresponding state. The vortices are clearly seen in the troughs and we note that they are fairly weak with the flow in their vicinity almost stagnant. Such flows may be useful in processes such as cell trapping with the troughs acting as micro chambers (see Introduction for comments on cell trapping).

The results in this section indicate that for a given imposed flow rate the wall geometry can be manipulated (both its amplitude and its period in the case of sinusoidal corrugations, for example) along with the imposed electric field, to obtain dynamical behaviour in confined micro scale geometries that can be useful in applications. The structures computed are fully nonlinear and are most likely not amenable to analytical descriptions. They are underpinned by loss of stability of nonuniform steady states and in what follows we consider such stability questions analytically using linear Floquet analysis.

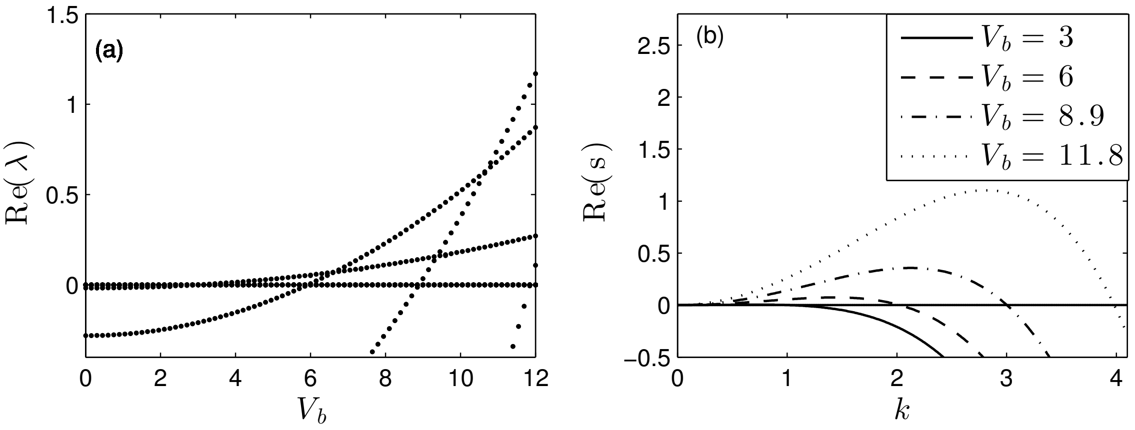

Figure 10.12. (a) Real part of the growth rate λ as the applied voltage V_b is varied for a flat boundary case. (b) Real part of the growth rate s versus wavenumber k as calculated from the linear stability analysis in §10.2 for $V_b = 3$ (solid line), $V_b = 6$ (dashed line), $V_b = 8.9$ (dot-dashed line) and $V_b = 11.8$ (dotted line). Other parameters are $\tilde{Q} = 0.1$, $\beta = 1$, $\bar{\epsilon}_1 = 1$, $\bar{\epsilon}_2 = 2$, $m_2 = 1$.

10.8. Floquet stability analysis of nonuniform flows

The objective of this section is to use linear stability theory to establish ranges of values of V_b (other parameters fixed, for instance) for which the flow transitions from nonuniform steady states to the "walking behaviour" we described in the previous section. A natural setting for the analysis is to use Floquet theory since the underlying flows are spatially periodic. Given a steady state $h_s(x)$ (this is a solution of equation (10.5) for example) we write $h(x,t) = h_s(x) + \tilde{h}(x,t)$, substitute into (10.1) and linearise to obtain

$$\tilde{h}_t + \Big[f_1\,\tilde{h} + f_2\,\tilde{h}_x + f_3\,\tilde{h}_{xxx}\Big]_x = 0, \tag{10.11}$$

where $f_i = f_i(h_s, h_{sx}, h_{sxxx}, z, z_x)$ for $i = 1, 2, 3$ are periodic functions of x with the same period as the steady state solution, and they are found using Maple. Looking for solutions of the form

$$\tilde{h}(x,t) = F(x)\,\exp\left(\lambda t + ikx\right),$$

where $F(x)$ is a periodic function with the same spatial period as $\tilde{h}(x,t)$ and the eigenvalue λ is complex, equation (10.11) becomes

$$\begin{aligned}\lambda F + F\left[f_{1x} + ik(f_1 + f_{2x} - k^2 f_2 - ik^3 f_{3x} + k^4 f_3)\right] + \\ + F'\left[f_1 + f_{2x} + 2ikf_2 - 3k^2 f_{3x} - 4ik^4 f_3\right] + \\ + F''\left[f_2 + 3ikf_{3x} - 6k^2 f_3\right] + F'''\left[f_{3x} + 4ikf_3\right] + F''''\left[f_3\right] = 0.\end{aligned} \tag{10.12}$$

In the calculations that follow we consider perturbations of the same wavelength as the underlying solution: since we are looking for solutions of the form $F(x)\exp(\lambda t + ikx)$, where $F(x)$ is a periodic function with the same spatial period as the the underlying solution, it is sufficient to consider the case with $k = 0$. To clarify this point further we write $F(x) = \exp i\bar{k}x$ with $0 < \bar{k} < 1$ and we see that even if $k = 0$ all perturbations with the length of the domain or less are accounted for by $F(x)$. In what follows we analyse a typical case having flow rate $\tilde{Q} = 0.1$, and sinusoidal lower wall topography of amplitude $d_b = 0.4$, wavenumber $k_b = 4$ and mean value $y = -Z_c = -0.6$ (other parameters are as before with $\beta = 1$, $\bar{\epsilon}_1 = 1$, $\bar{\epsilon}_2 = 2$, $m_2 = 1$). Keeping these parameters fixed, we vary the voltage V_b and compute the eigenvalues λ numerically. For each V_b we find n eigenvalues where n is the number of discretisation points in x. Derivatives of $F(x)$ are found using spectral differentiation matrices. Since we are essentially interested in detecting instability as V_b varies, we found it useful to track only those eigenvalues whose real part is sufficiently large, and used $Re(\lambda) > -0.4$.

The code was tested for the trivial case of a flat wall (this in turn gives $h_s(x) = 0$) whose results were given in §10.2. In the Floquet setting of this problem we need to solve

$$\lambda F + AF_x + BF_{xx} + CF_{xxxx} = 0 \tag{10.13}$$

where A, B and C are the same constants as the ones found in equation (11.3). The calculated real part of λ versus V_b is given in figure 10.12.a where as noted above, only eigenvalues greater than -0.4 are shown. The results show different modes and how they become unstable as V_b increases. The first mode becomes unstable when $V_b = 3$, and then there are subsequent crossings by the second mode at $V_b = 6$, the third at $V_b = 8.9$ and the fourth at $V_b = 11.8$. Panel 10.12.b shows the growth rate as a function of wavenumber for different V_b as found in §10.2. The values of V_b above which the modes $k = 1$, 2, 3, 4 become successively unstable, are confirmed to be the same as those found using the Floquet analysis.

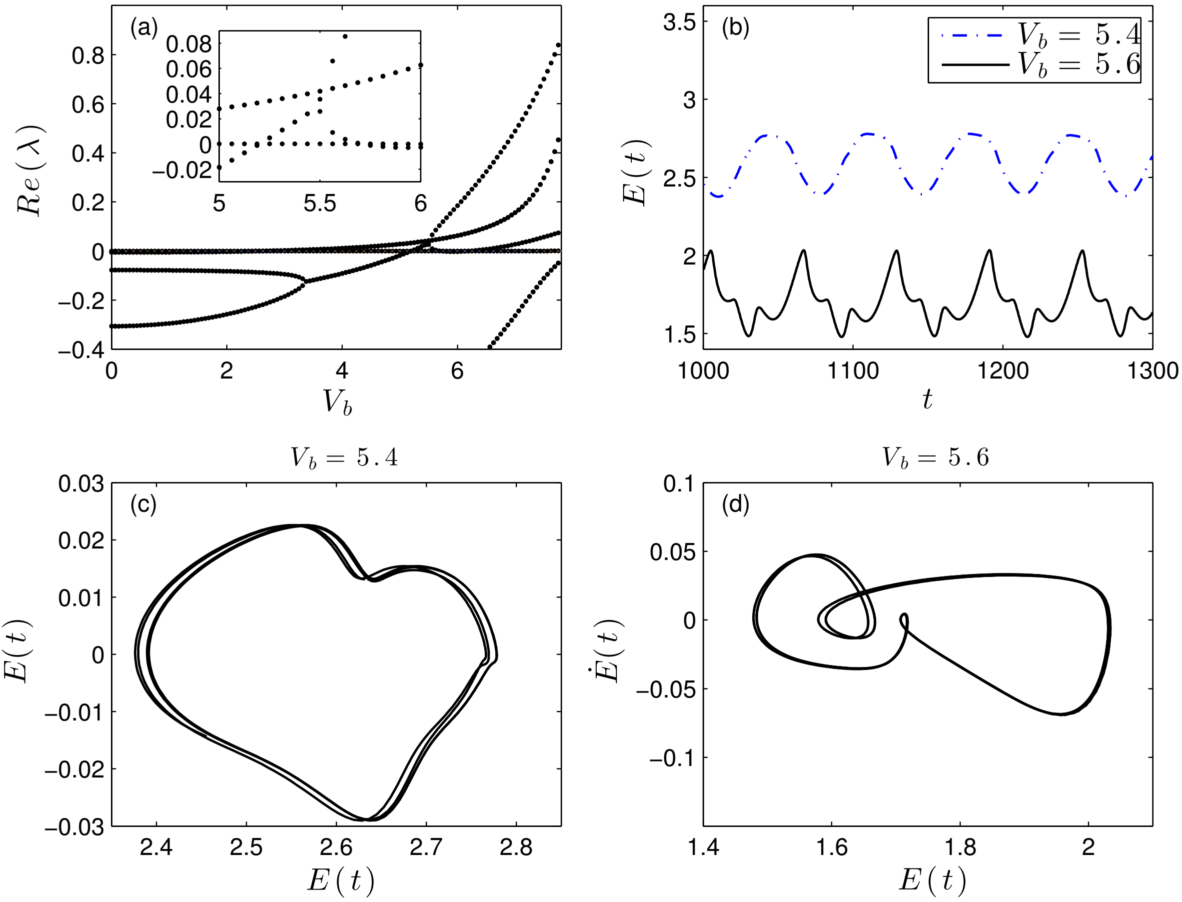

Figure 10.13. (a) Real part of the growth rate λ versus applied voltage V_b. Same parameters as in figure 10.12 with $d_b = 0.4$, $k_b = 4$ and $Z_c = 0.6$. (b) Time evolution of the energy $E(t)$. Applied voltage is $V_b = 5.4$ (dot-dashed line) and $V_b = 5.6$ (solid line). The bottom figures show the phase plane of the energy for (c) $V_b = 5.4$ and (d) $V_b = 5.6$.

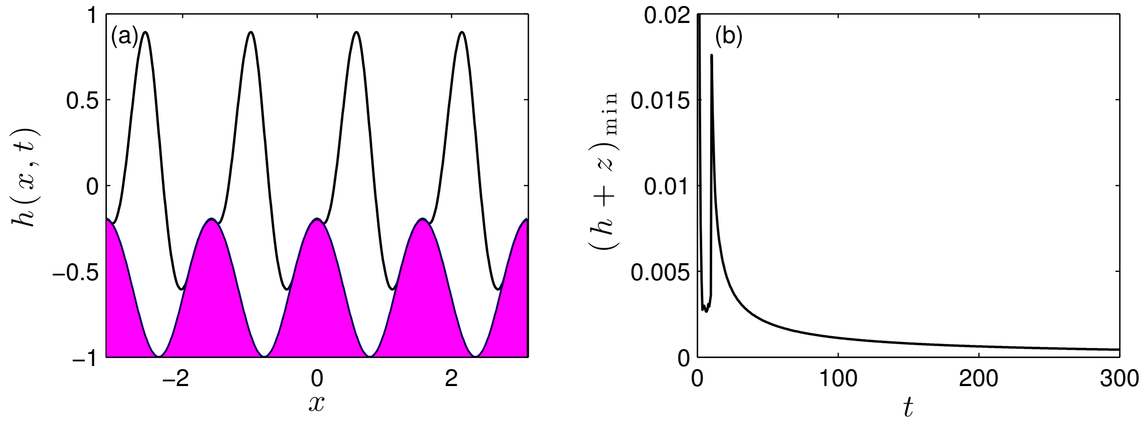

Figure 10.14. (a) Interface $h(x,t)$ at $t_{final} = 300$ for same parameters as figure 10.13 and $V_b = 20$. (b) Minimum of the gap between the interface and the boundary against time.

Next we consider the case with a wavy boundary and parameters as given above, and compute the eigenvalues λ from equation (10.12) with $k = 0$. Figure 10.13.a shows the variation of the real part of λ with V_b, and note that the first crossing yielding instability occurs at $V_b = 2.6$. This has been confirmed from the nonlinear time dependent computations that predict stability of nonuniform states for these parameters when $V_b < 2.6$. The next mode crossing to become unstable occurs at around $V_b = 5.2$. Some intricate behaviour is found near this point and the inset in figure 10.13.a depicts branches in more detail. It is seen that the branch that crossed at $V_b \approx 5.2$ itself pitchfork bifurcates at $V_b \approx 5.5$ into two branches. To observe the differences in the dynamics, we took values $V_b = 5.4$ and $V_b = 5.6$ that are below and above the critical value $V_b = 5.5$, and ran large time simulations of the nonlinear initial value problem. We find that the solution transitions into the "walking behaviour" described earlier and the energy norms along with the corresponding phase planes are included in panels 10.13.b-d. The lower voltage energy norm is less intricate than that for $V_b = 5.6$ in the sense that it does not contain as high frequency oscillations. It is also clear from figure 10.13.b that the time-averaged energy values are different and we can conclude that the two solutions are on different branches. More information regarding the dynamics of these solutions are given in the phase planes in panels 10.13.c-d - even though we cannot state this conclusively, it appears that the dynamics for $V_b = 5.4$ are quasi-periodic in time whereas those for $V_b = 5.6$ are periodic and more analogous to those found earlier - e.g. figure 10.8.

The results presented in figure 10.13 are for moderate values of $V_b \leq 8$. Even though a detailed bifurcation study and stability of the resulting branches is of intrinsic interest, it is beyond the aims of this work, but we illustrate the richness of expected behaviour by considering several larger values of V_b. For example, solution of the initial value problem starting from a flat interface (all other parameters as in figure 10.13) and for a relatively high voltage of $V_b = 20$, indicates that after some initial transient oscillations appears to reach a steady state that is stuck at the lower wall troughs but is well separated from the upper wall. Figure 10.14 shows the solution at a final computed time $t_{final} = 300$ and closer inspection of the results shows that the thin films of the lower fluid that form on the wall humps are slowly draining with time. The minimum thickness of these films is plotted against time in panel 10.14.b and the slow draining is clearly observed. This solution is another attracting state (albeit quasi-static) and essentially asymptotically traps regions of fluid 2 between successive wall humps with the upper fluid 2 flowing above them as can be seen from figure 10.14.a. We note that the simulations indicate that the film thickness does not vanish in finite time in agreement with other related thinning film problems - see for example Craster & Matar (2005), Tseluiko & Papageorgiou (2007*b*). (Physically, addition of attracting van der Waals forces would rupture the thin film in finite time, see Erneux & Davis (1993), Savettaseranee *et al.* (2003).) For $V_b = 8.5$ we see the two attracting states competing with each other with the solution going to the "stuck" behaviour first and then going into a "walking" behaviour. In the former state, the solution undergoes time periodic oscillations without translating down the channel, before losing stability to the "walking" state. Snapshots of the two solutions are included in figure 10.16.a at times $t = 60$ (dashed curve) and $t = 300$ (solid curve), along with the evolution of the energy $E(t)$ that indicates the time periodic behaviour at smaller times and the transition to the "walking" state at larger times. Note that the "walking" state evolves time periodically with a much longer period than that of the "stuck" solution.

10.9. Flows at high fluxes $\tilde{Q}$

So far we have explored the behaviour of the system for a low overall flow rates characterised by small values of $\tilde{Q}$. In this section we consider the behaviour of the confined electrified flow over large amplitude sinusoidal topography and at relatively large values of $\tilde{Q}$. To fix matters we consider the same parameters as before (e.g. figure 10.13) but now take $\tilde{Q} = 20$ and vary the voltage parameter V_b.

We begin by considering the linear stability of the nonuniform steady states for $\tilde{Q}$ as V_b varies. The results are shown in figure 10.15 that depicts the real part of λ for

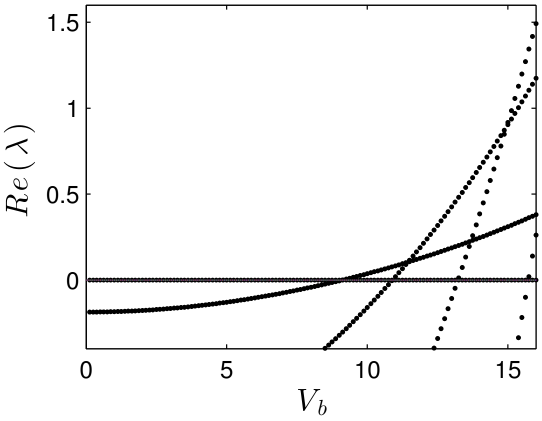

Figure 10.15. Real part of the growth rate λ versus the applied voltage V_b. Same parameters as figure 10.13 but with $\tilde{Q} = 20$.

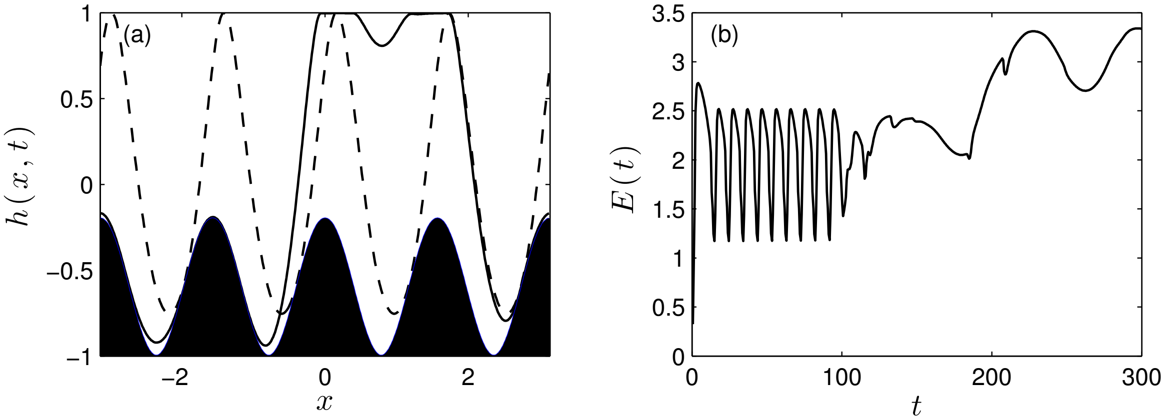

Figure 10.16. (a) Interface at times $t = 60$ (dashed curve) and $t = 300$ (solid curve) for same parameters as figure 10.13 and $V_b = 8.5$. (b) Energy $E(t)$ plotted as time is varied.

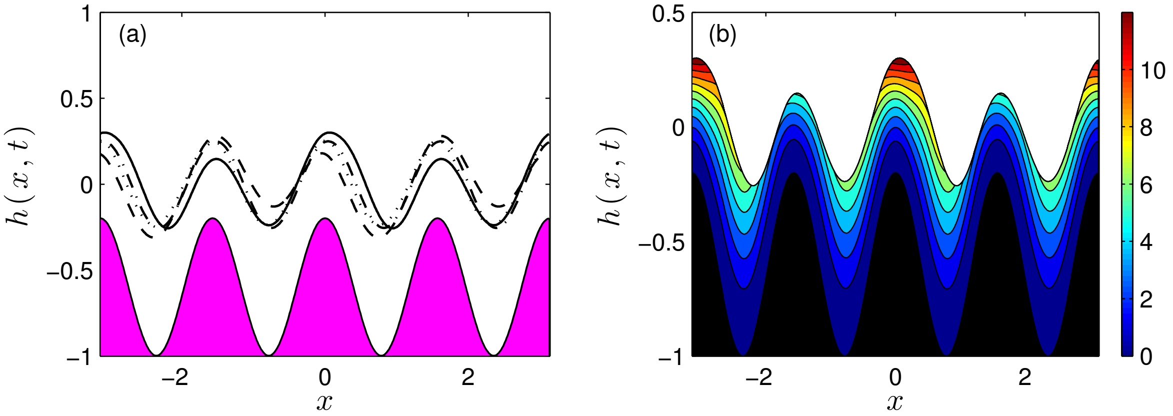

Figure 10.17. (a) Interface $h(x,t)$ at $t = 1$ (dotted line), $t = 25$ (dot dashed line), $t = 75$ (dashed line) and $t = 100$ (solid line). (b) Streamlines at time t=100. Parameters are the same as in figure 10.7 but with $V_b = 14$ and $\tilde{Q} = 20$.

different V_b. It is found that there is a crossing at $V_b \approx 9.1$ so that all perturbations with wavelength equal to the domain size are stable for voltages below this value. Comparing these results with those in figure 10.13 that has $\tilde{Q} = 0.1$, we can conclude that generally a higher flow rate has a stabilising effect.

To investigate the dynamics into the unstable regime we pick $V_b = 14$ which according to the results in figure 10.15 supports three unstable modes. The initial value problem is solved starting from a flat interface initial condition and following the nonlinear development until $t = 100$ or more. Representative results are given in figure 10.17; panel 10.17.a shows the interfacial shape at $t = 1$, 25, 75 and 100 and the results predict clearly that at this moderately large value of $\tilde{Q} = 20$ the interface is in phase with the lower wall topography but at the same time performs small amplitude (and in fact high frequency) time-dependent oscillations. Panel 10.17.b shows the instantaneous streamlines at the final time $t = 100$ and we can see that the fluid flows over the topography without any vortices present - we note that such regimes are therefore not advantageous for mixing or fluid trapping phenomena found earlier.

10.10. Asymptotic Solution for large $\tilde{Q}$

The results in figure 10.17 (as well as several other numerical experiments not reported here) suggest that as $\tilde{Q}$ increases the flow is a steady state that is modulated spatiotem-

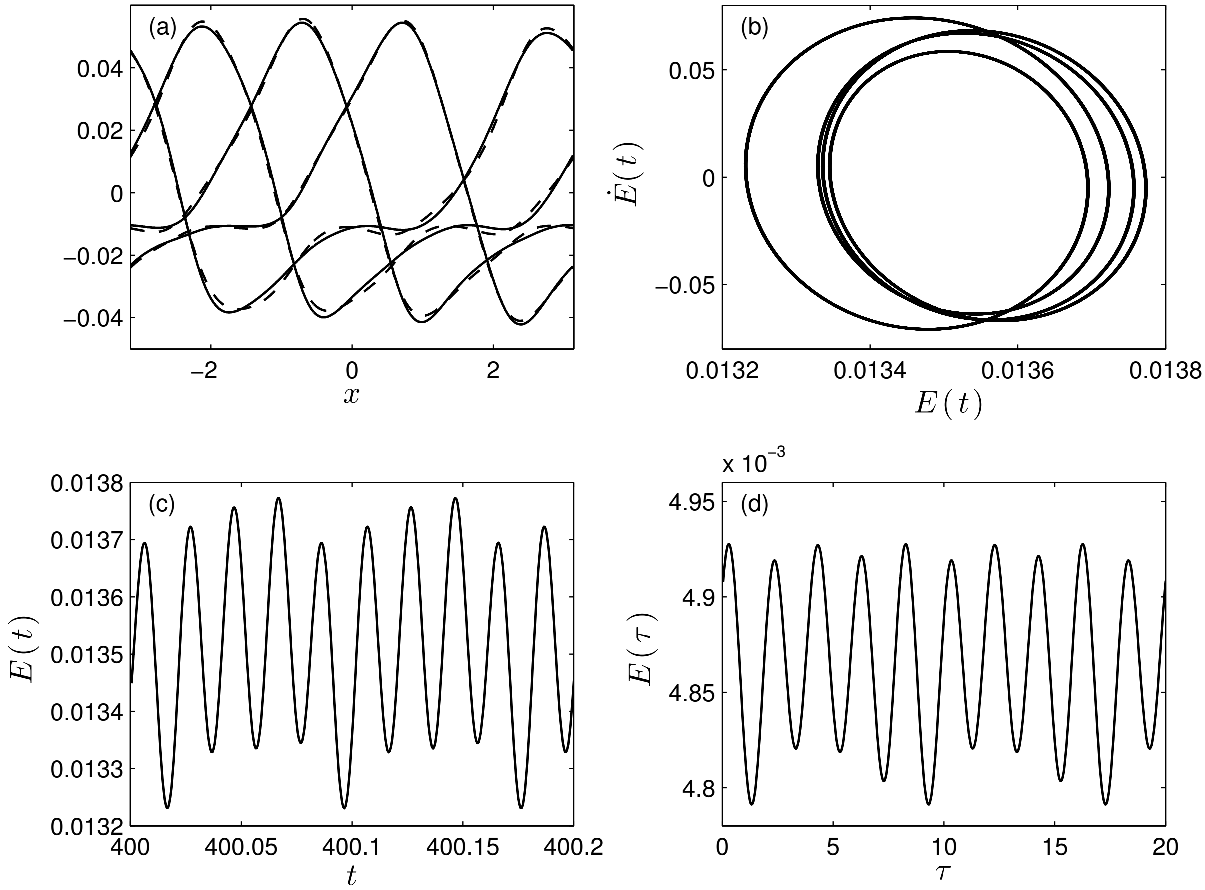

Figure 10.18. (a) Full numerical solution minus the steady state solution $h(x,t)-h_0(x)$ (dashed line) compared with the asymptotic solution $\delta H(x,\tau)$ (solid line) at four different times with $t=\tau/\tilde{Q}$. (b) Phase plane of the energy $E(t)$. (c) $E(t)$ plotted as time t is varied. (d) $E(\tau)$ plotted as time τ is varied.

porally by a small amplitude and high frequency component. This observation is now formalised by considering asymptotic solutions to equation (10.1) for large $\tilde{Q}$. Setting $\delta = 1/\tilde{Q} \ll 1$, we seek a solution of (10.1) of the form

$$h(x,t) = h_0(x) + \delta H(x,\tau) + \ldots, \qquad \tau = t/\delta, \tag{10.14}$$

where $h_0(x)$ is the steady state solution at these parameter values, i.e. a solution of (10.5). The equation for $H(x,\tau)$ emerges at $\mathscr{O}(\delta)$ and reads

$$H_\tau + \left\{ \tilde{F}(h_0(x), z(x))\, H \right\}_x = 0, \tag{10.15}$$

where $\tilde{F}$ is a function of $h_0(x)$, the lower boundary shape $z(x)$ and its only other dependence is on the physical parameters of the system.

Equation (10.15) is solved numerically for an initial condition given by the full time dependant numerical solution at a selected time (and after transients have died out) minus the steady state $h_0(x)$, and with $\tilde{Q} = 100$ (so that $\delta = 0.01$). The asymptotic solution $\delta H(x, t/\delta)$ is compared with $h(x,t) - h_0(x)$ in figure 10.18.a for four different times and we see that the agreement between the two is excellent. Panel 10.18.b shows the phase plane of the energy of $h(x,t) - h_0(x)$ coming from the full numerical computation - the spatiotemporal modulation mentioned above is clearly seen from the figure. Panel 10.18.c shows the evolution of $E(t)$ over approximately ten oscillation cycles. In panel 10.18.d we include the evolution in τ of the energy $E_a(\tau) = \int_{-\pi}^{\pi} \delta^2 H^2(x,\tau) dx$ of the asymptotic correction, where once again ten oscillation cycles are included. This data was used to estimate the frequencies f_t and f_τ of oscillation of the full and asymptotic solutions, respectively. We find that $f_t/f_\tau \approx 100 = \tilde{Q} = 1/\delta$ as expected. This provides additional evidence of the relevance of the asymptotic solutions at large $\tilde{Q}$ (in fact we found good agreement for $\tilde{Q}$ as small as 10).

10.11. Summary of research

We have examined the behaviour of an interface between two fluids sandwiched between a flat electrode and a patterned electrode. The case with a flat lower boundary is explored first: a linear stability analysis shows that the system is unstable for a finite range of wave numbers. To confirm this prediction, the evolution equation is solved numerically: in the flat boundary case the results show that initially small perturbations take the form of columnar structures that are reminiscent of those found in the previous chapter.

Next, a relatively small waviness is imposed on the lower boundary and two types of behaviour are observed. For wavenumbers that are unstable in the flat case, moving structures develop with their shape affected by the wavy boundary. For stable wavenumbers, the interface reaches a steady state that mimics the lower boundary. By tracking the speed of the waves in the wavy boundary case, it is shown that the transition from one type of behaviour to the other occurs at a critical voltage which is in agreement with the critical voltage found from the linear stability analysis of the flat boundary case. An analytical solution is found for the case when the voltage is below critical.

The amplitude of the boundary is increased and the full numerical solution shows that the boundary has a much stronger influence on interfacial dynamics and the linear analysis for the flat case is no longer helpful to make any predictions on stability. In the case with four humps that occupy nearly half of the height of the domain, the interface reaches a non uniform steady state that mimics the topography and for large enough voltages, it starts sliding over the boundary. For low voltages, the interface stays at the steady state and fluid recirculates inside the troughs making this a favourable environment for cell trapping. For a range of voltages, the interface exhibits a “walking” motion which causes the fluid in the lower layer to alternate between sliding through the troughs and forming strong vortices above the peaks suggesting that this particular behaviour of the system is desirable for efficient mixing. A Floquet analysis gives the ranges of voltages for each type of behaviour. To complete the analysis, we look at the system with very strong overall flow rate and find that increasing the fluid flux has a stabilising effect on the system and the vortices in the lower layer are suppressed making such a solution less desirable for efficient mixing. Full numerical results show that for a much higher flow the topography has a stronger influence on interfacial dynamics even for low amplitudes of the wavy boundary. Finally, an asymptotic solution is found for large values of the overall flow rate $\tilde{Q}$ which is used to find the frequency of oscillation of the interface.

11. Two layer flow of thin perfect dielectric films between two corrugated electrodes

In this chapter, we aim to explore how the inclusion of topography on the top boundary influences the types of behaviour identified in the previous section. We extend the analysis described in §10 to a system with corrugations on both the top and the bottom boundaries i.e. when $z(x) = -Z_c + d_{b1}\cos(k_{b1}x)$ and $\beta(x) = B_c - d_{b2}\cos(k_{b2}x + \phi)$ where B_c, Z_c, d_{b1}, d_{b2} and ϕ are constants and k_{b1}, k_{b2} are the wavenumbers. We consider the top and the bottom boundaries to have the same sinusoidal shape with the same wavenumber $k_{b1} = k_{b2} = 4$ and same distance from the undisturbed interface $Z_c = B_c = 0.9$ and $d_{b1,2} = 0.2$. We look at two cases: the case when the top is offset from the bottom by $\phi = \pi$ (see §11.1) and the case when the top and the bottom corrugations are symmetrical i.e. $\phi = 0$ (see §11.2). The evolution equation is the same as before:

$$h_t + \left\{ \frac{D_3}{6m_2} \left[D_4 p_{2x}^{(0)} + 3m_2 f_2 \right] \right\}_x = 0 \tag{11.1}$$

where $D_3 = (h+z)^2$ and $D_4 = h - 2z$ and f_2 and $p_{2x}^{(0)}$ are functions of $h(x,t)$, its derivatives and the functions that define the shapes of the two boundaries $z(x)$ and $\beta(x)$.

We begin our investigation by extending the Floquet analysis presented in §10.8 to include a non-constant top boundary. As before, we consider perturbations of the same wavelength as the underlying solution and obtain the following eigenvalue problem:

$$\lambda F + F f_{1x} + F_x f_1 + f_{2x} + F_{xx} f_2 + F_{xxx} f_{3x} + F_{xxxx} f_3 = 0 \tag{11.2}$$

where $F(x)$ is a periodic function with the same spatial period as the solution. In this case the functions f_i $(i = 1, 2, 3)$ also depend on $\beta(x)$:

$$f_i = f_i(h_s, h_{sx}, h_{sxxx}, z, z_x, \beta, \beta_x)$$

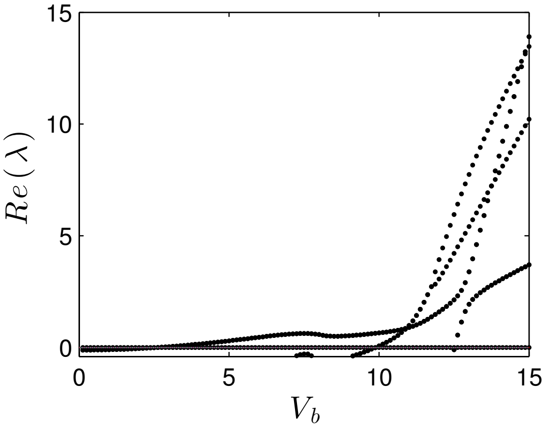

Figure 11.1. Real part of the growth rate λ vs applied voltage V_b. Top offset.

We choose to analyse a typical case when $\tilde{Q} = 0.0345$, $\bar{\epsilon}_1 = 1$, $\bar{\epsilon}_2 = 2$, $m_1 = 1$, $m_2 = 1$. We keep these parameters fixed and vary the voltage V_b to investigate the stability of the system. In the next two sections we present the plots of the real part of the eigenvalues λ against the voltage for two different geometries and compare this with full time dependant results.

11.1. Offset boundaries

In this section we analyse the stability of the system when the upper and lower boundaries have the following shapes: $y = -0.9 + 0.2\cos(4x)$ and $\beta(x) = 0.9 - 0.2\cos(4x + \pi)$. We begin by plotting the real parts of the eigenvalues λ against the voltages V_b in figure 11.1 to get an idea of the points where changes in the behaviour of the system might occur. The first crossing of the x-axis is at $V_b = 2.6$ which is the same value of the voltage for which we have a first crossing in the case of just a single wavy boundary. There is a crossing of two branches of eigenvalues at $V_b = 10.8$ which leads us to look at the full time dependant solutions for voltages both below and above that value to see if we detect any changes in the behaviour of the system.
As before we make use of the energy and examine the plots of the L^2-norm of h against time for four values of the voltage. We also compute the full time dependant numerical simulation: figure 11.3 shows the profiles of the interface for each of these four voltages at time $t = 400$. From figure 11.2.a we see that for voltages that are quite far from the crossing of the two branches of eigenvalues such as $V_b = 8$ the energy plot has a similar

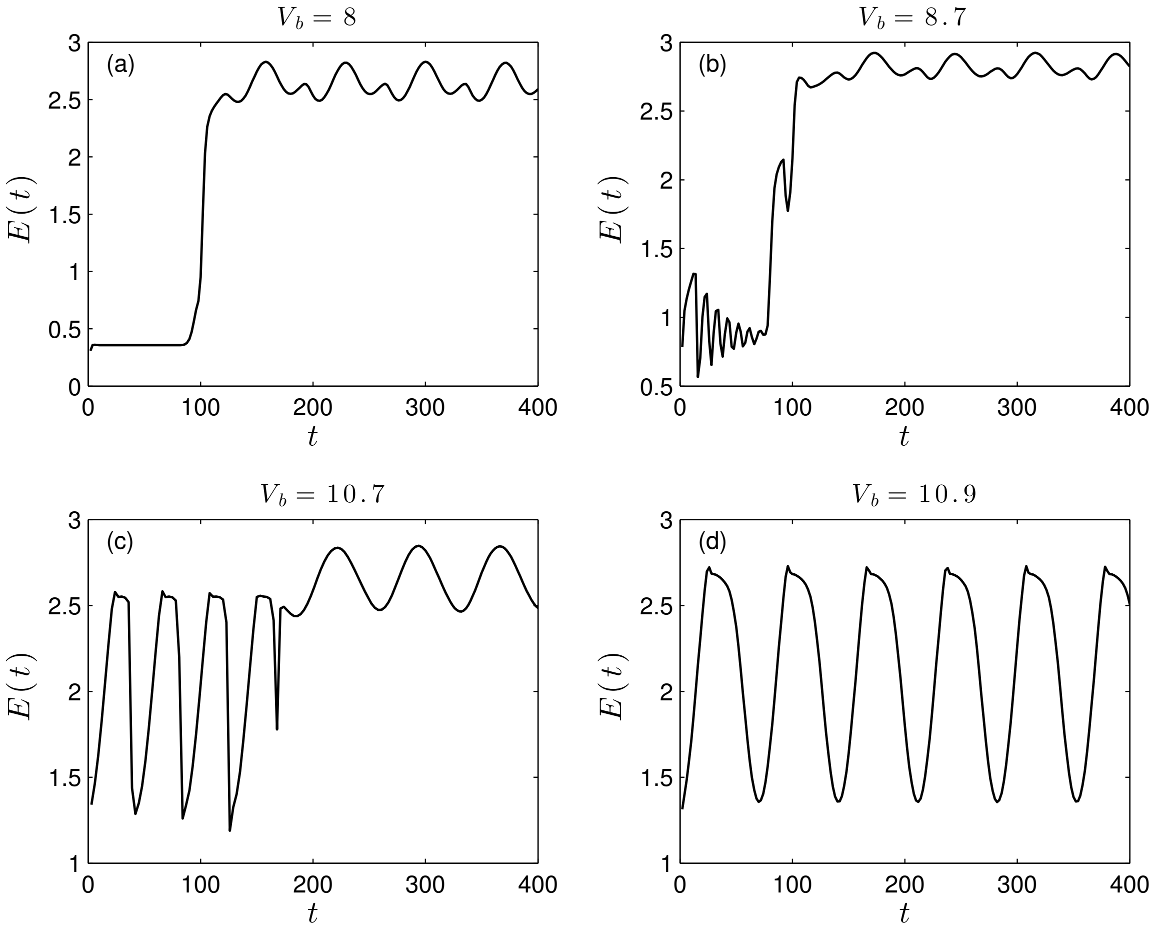

Figure 11.2. Energies at different voltages (a) $V_b = 8$, (b) $V_b = 8.7$, (c) $V_b = 10.7$ and (d) $V_b = 10.9$. Top corrugation is offset from the bottom by $\phi = \pi$.

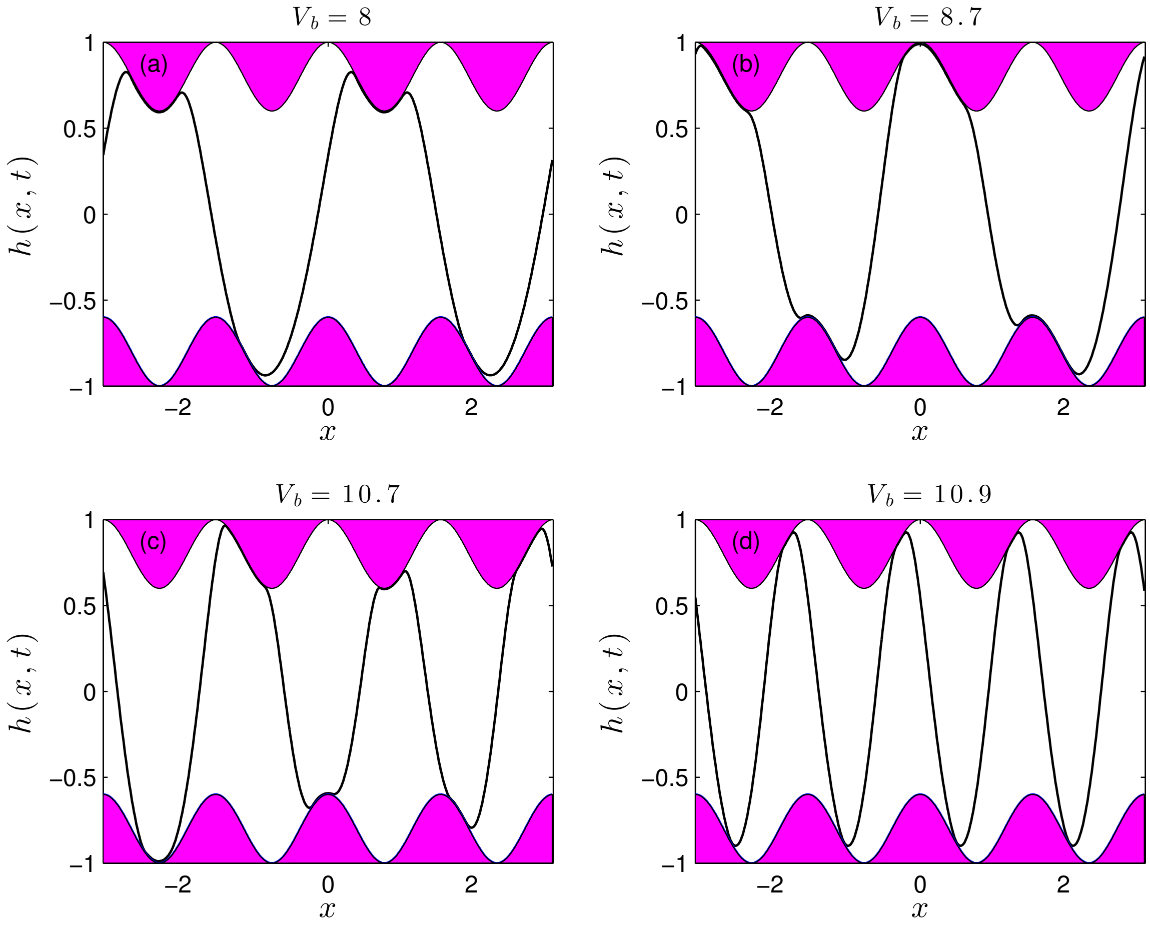

Figure 11.3. Interface at $t = 400$ at voltages (a) $V_b = 8$, (b) $V_b = 8.7$, (c) $V_b = 10.7$ and (d) $V_b = 10.9$. Top corrugation is offset from the bottom by $\phi = \pi$.

structure to the one corresponding to the “walking” behaviour which we analysed in the case of a flat top: there is an initial time period when the interface is stable and hence the energy is constant; at a later time the solution takes the form of a time modulated wave which leads to the doubly peaked profile of the energy (compare with figure 10.13.b). When we compute the full time dependant solution we find that indeed the interface evolves in a “walking” motion, and a profile of it is given at time $t = 400$ in figure 11.3.a. For voltages above the crossing e.g. $V_b = 10.9$ the energy is immediately time periodic without going through the constant phase and, as we see from figure 11.3.d, the interface has the same wavenumber as the corrugation and travels with its peaks sliding over the sinusoidal boundaries. In between those two voltages there is a competition between the two behaviours: for $V_b = 8.7$ the interface takes the wavenumber of the boundary and oscillates initially and later transitions into the “walking” behaviour as in the case of $V_b = 8$. For $V_b = 10.7$ the interface has again the same wavenumber as the boundaries initially and it attempts to go into the “sliding” behaviour such as the one for $V_b = 10.9$ but gets “stuck”. It later starts travelling with a combination of the “sliding” and the “walking” behaviours.

We have thus identified two distinct behaviours of the interface: for voltages $2.6 \leq V_b \leq 8$ the interface has a similar behaviour to the “walking” motion analysed in the case of one corrugated electrode; for voltages $10.9 \leq V_b$ the interface “slides” over the boundary and takes the wavenumber of the corrugation; for voltages $8 \leq V_b \leq 10.9$ we have competition between the two behaviours. We conclude that including a top electrode corrugation of the same shape as the bottom electrode and offset by $\phi = \pi$ does not affect the value of the critical voltage necessary to drive the system out of equilibrium and for a range of voltages we have the “walking” behaviour seen previously. For high enough voltages the inclusion of the top boundary causes the interface to take the wavenumber of the boundaries as it slides over them, a behaviour we had not see in the previous setup.

11.2. Symmetrical boundaries

We move on to examining the behaviour of the system in the case of two symmetrical boundaries with shapes $y = -0.9 + 0.2\cos(4x)$ and $\beta(x) = 0.9 - 0.2\cos(4x)$ and as before, we start by plotting the real parts of the eigenvalues λ against the voltages V_b (figure 11.4.a). The first crossing of the x-axis is at $V_b = 2.6$ which is the same value of the voltage for which we have a first crossing in the case of just one wavy boundary and in the case of two offset boundaries. We encounter problems when numerically calculating the steady states at $V_b = 5.75$: for higher voltages we increase the value of V_b

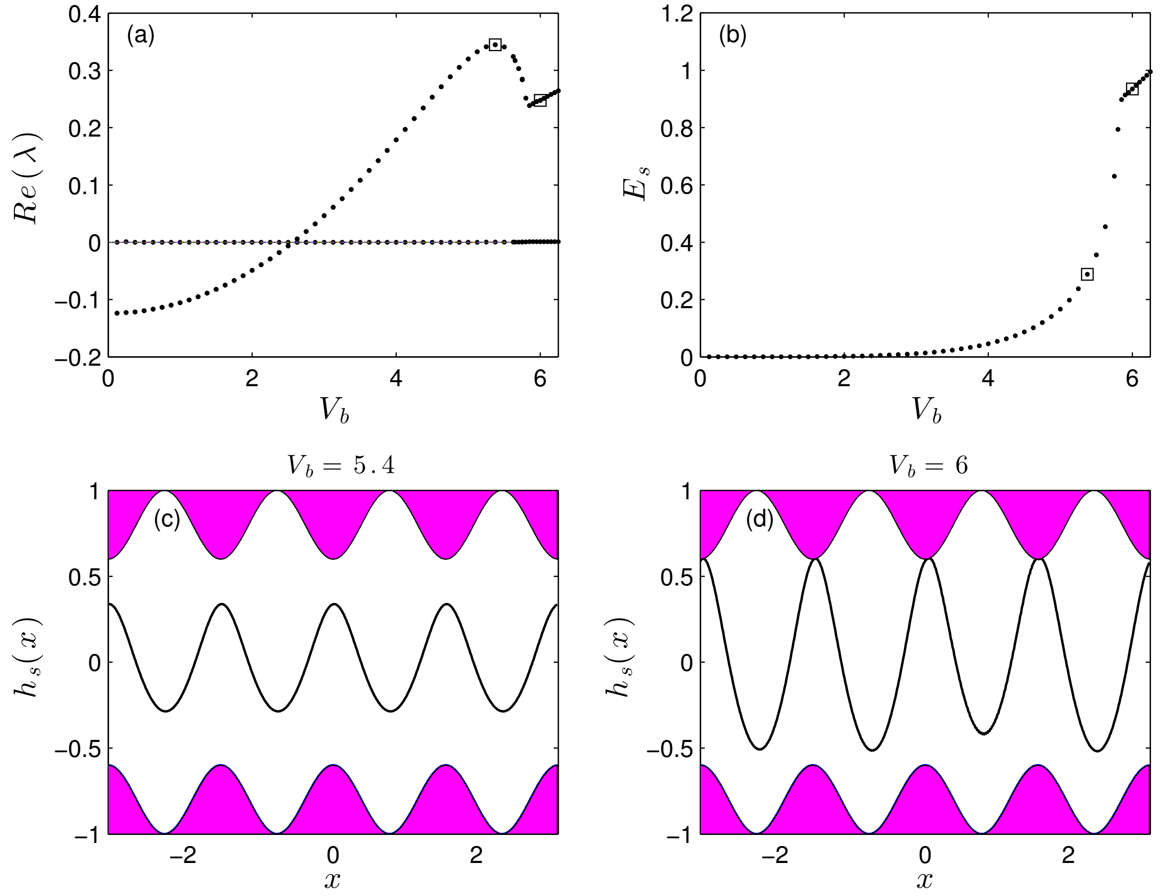

Figure 11.4. (a) Real part of the growth rate λ vs applied voltage V_b. (b) energies of the steady states at different voltages V_b. The squares highlight the eigenvalues and the energies at two voltages $V_b = 5.4$ and $V_b = 6$. Bottom panels show the steady state profiles of the interface for (c) $V_b = 5.4$ and (d) $V_b = 6$. Top and bottom symmetrical.

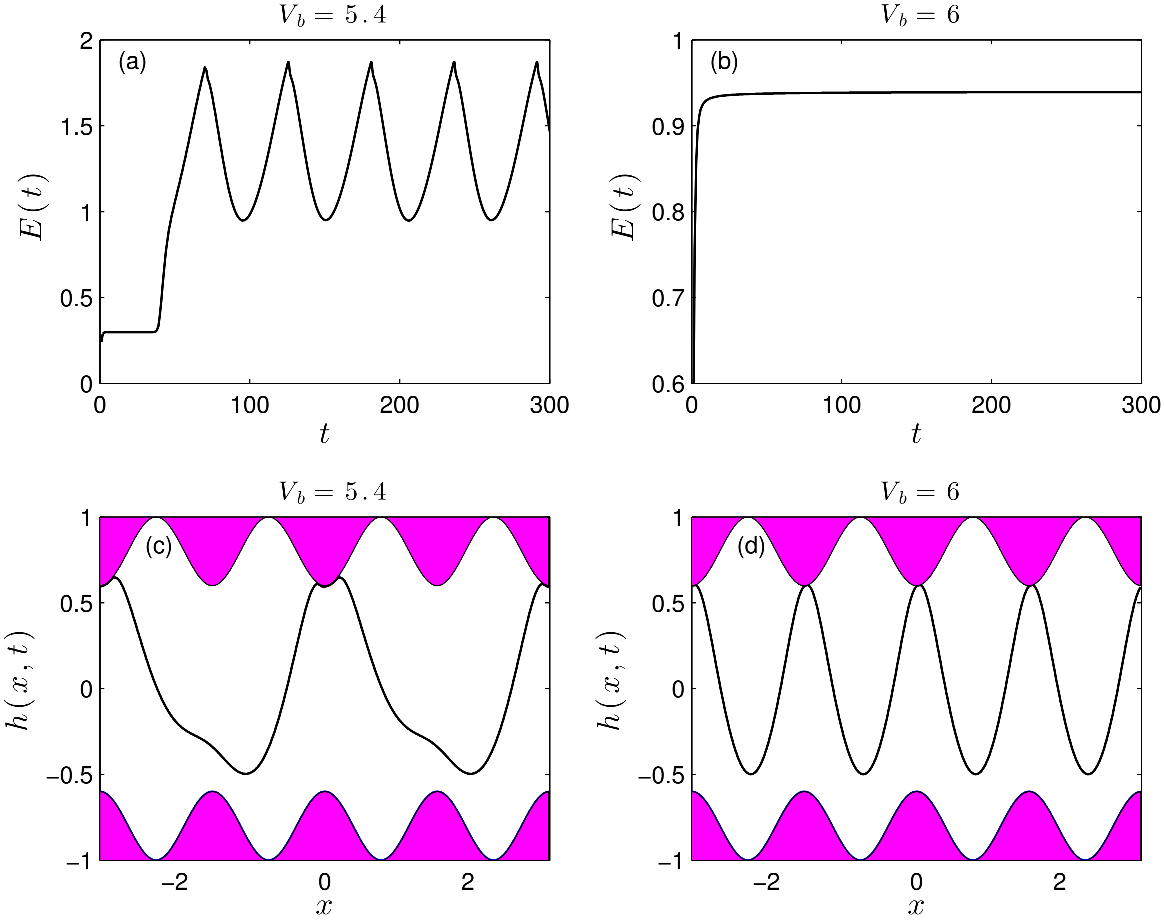

Figure 11.5. Top panels are plots of the energy $E(t)$ against time for (a) $V_b = 5.4$ and (b) $V_b = 6$. Bottom panels show the profile of the interface calculated using the full time dependant numerical simulation at $t = 100$ for (c) $V_b = 5.4$ and (d) $V_b = 6$. Top and bottom symmetrical.

by very small increments and use a continuation technique to find the steady solutions. When we plot the energy of the steady states (figure 11.4.b) and the real parts of the eigenvalues (figure 11.4.a) against the voltage V_b we notice an abrupt change in behaviour at $V_b = 5.85$. The bottom panels of figure 11.4 are the steady state profiles for two voltages, one below $V_b = 5.85$ and one above: the steady profile for the higher voltage appears to touch the top boundary which might explain the change in behaviour in the branch of eigenvalues. We perform full time dependant numerical simulations to find that for voltages below $V_b = 5.85$ the interface travels in a way that is reminiscent of the "walking" behaviour found in previous sections. However for voltages above that value the interface approaches the top boundary closely and slowly drains. Figure 11.5 gives the plots of the energies for the two voltages against time and the profiles of the interface found from time dependant simulations for time $t = 100$. For $V_b = 5.4$ the energy is initially constant and after a certain time it is time periodic; the full numerical solution is similar to the "walking" solutions found in previous sections. For $V_b = 6$ the energy increases very fast initially and then is nearly constant with a very slow increase which corresponds to the interface reaching the boundary and slowly draining.

We have thus found a critical voltage $V_{bc} = 5.85$: for voltages below that value, the interface travels and its movement may be exploited for mixing; for higher voltages the interface creates columnar structures that mimic the boundary similar to the ones found in the case of two flat boundaries (Craster & Matar, 2005) which could be useful for patterning. We conclude that the inclusion of a symmetrical boundary does not affect the value of the voltage necessary to drive the system out of equilibrium; however it limits the range of voltages which permit the "walking" behaviour. In addition, for voltages above $V_b = 5.85$ the interface mimics the shape of the boundaries and nearly touches the top electrode slowly draining, thus creating a fixed pattern.

11.3. Analytical Solution

We found that adding a corrugation to the top boundary does not affect the value of the critical voltage above which the system is driven out of equilibrium. Below this value $V_b = 2.6$ we expect the interface to reach a steady state. We extend the analysis in §10.6 and seek an analytical solution of the system when both wall corrugations are shallow. Let us assume that the depth of the boundaries is small so that we can write the shape of the boundary as $z(x) = Z_c + \epsilon Z(x)$ and $\beta(x) = B_c + \epsilon b(x)$ the interface height as $h(x) = \epsilon H_0(x) + O(\epsilon^2)$ where ϵ is small. These are substituted into eq.(10.5) and at leading order we get:

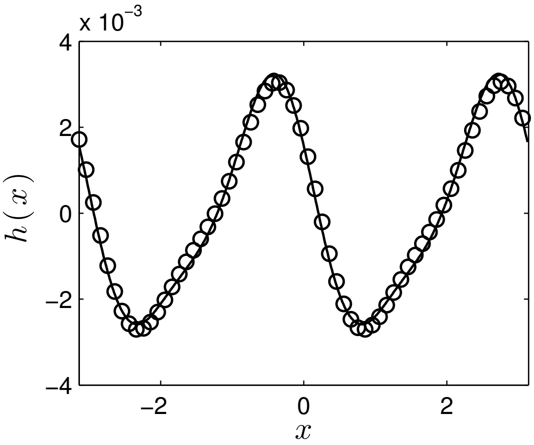

Figure 11.6. Numerical steady state solution compared to the analytical solution of eq.(11.3) for $k_{b1} = 2$, $k_{b2} = 4$, $\phi = \sqrt{2}$.

$$AH_0 + BH_{0x} + CH_{0xxx} = -DZ - EZ_x - Fb - Gb_x \tag{11.3}$$

where A, B, C, D, E, F and G are constants that depend on the physical parameters in the problem and are found using Maple.
Let us consider the case when $z(x) = Z_c - d_b \cos(k_{b1}x)$, $\beta(x) = B_c - d_b \cos(k_{b2}x + \phi)$ so that we have $Z(x) = -\cos(k_{b1}x)$, $b(x) = -\cos(k_{b2}x + \phi)$ and $\epsilon = d_b$. Then the general solution of eq.(11.3) is given by:

$$\begin{aligned} H_0(x) =& C_1 \exp(\lambda_1 x) + C_2 \exp(\lambda_2 x) + C_3 \exp(\lambda_3 x) + C_4 && (11.4)\\ &+ Re(p)\cos(kk_{b1}x) - Im(p)\sin(kk_{b1}x) + Re(q)\cos(kk_{b2}x) - Im(q)\sin(kk_{b2}x) && (11.5)\end{aligned}$$

where C_i, $i = 1, 2, 3, 4$ are constants, λ_i, $i = 1, 2, 3$ are the roots of $A + B\lambda + C\lambda^3 = 0$. p and q are given by the following expressions:

$$p = \frac{D + ikk_bE}{A + ikk_bB - i(kk_b)^3C},$$
$$q = \frac{FM - kGL + iFL + ikMG}{A + ikk_bB - i(kk_b)^3C},$$

where $L = \sin(\phi)$ and $M = \cos(\phi)$. The constants C_i, $i = 1, 2, 3, 4$ are found applying periodic boundary conditions at $x = \pm\pi/k$ and an integral constraint on H_0:

$$\int_{-\pi/k}^{\pi/k} H_0(x)dx = 0 \tag{11.6}$$

In the special case when $k_b, k \in Z$ with $k_b \neq \lambda_i$ for $i = 1, 2, 3$, it can be shown that the roots of $A + B\lambda + C\lambda^3 = 0$ are such that $Re(\lambda) \neq 0$ and hence the expression for the interface simplifies to:

$$H_0(x) = Re(p)\cos(kk_{b1}x) - Im(p)\sin(kk_{b1}x) + Re(q)\cos(kk_{b2}x) - Im(q)\sin(kk_{b2}x) \tag{11.7}$$

Figure 11.6 gives a comparison between the steady state solution calculated numerically and the analytical solution given by eq.(11.5) for a case when the top and bottom sinusoidal corrugations have different wavenumbers and the top is offset by $\phi = \sqrt{2}$ and we find excellent agreement.

11.4. Summary of research

We have examined the behaviour of an interface between two perfect dielectric fluids sandwiched between two sinusoidal electrodes. We consider two cases: one when the top boundary is offset from the bottom and the other when the top and bottom electrodes are symmetrical. We make use of the Floquet analysis presented in the previous chapter to analyse the stability of the system for changing applied voltage. For all three cases (flat top, offset top and symmetrical top) the critical voltage required to drive the system out of equilibrium is the same. For slightly higher voltages the system reaches an initial steady state and then transitions into the “walking” behaviour described in the previous chapter. For the case of an offset top, we have identified a range of voltages for which the interface takes the wavenumber of the corrugations and “slides” past them. There is also a range of voltages for which we have competition between the “sliding” and “walking” regimes with highly oscillatory initial behaviour. For the case of symmetrical corrugations we found a critical voltage above which the interface gets “stuck” i.e. it takes the wavenumber of the electrode shape, nearly touches the top wall and slowly drains thus creating a pattern. Finally, we found an analytical solution valid for shallow wall corrugations for the range of voltages when the system is stable. This solution is valid for any wavenumbers and any value of the parameter ϕ which determines how far offset the top and the bottom corrugations are.

12. Two layer flow of thin perfect dielectric films over steps

In this chapter we examine the behaviour of the system presented in §10 but instead of having a sinusoidal lower boundary we consider flow over a step. This is to investigate the effect of a sudden sharp change in the boundary. The lubrication approximation used throughout this part of the thesis assumes small free surface slopes which means that our equations could potentially fail for a sharp step topography. However several numerical studies (Gaskell *et al.*, 2004; Mazouchi & Homsy, 2001) show that results from the lubrication equations are accurate for such flows which justifies our use of this approximation. The evolution equation for the interface is exactly the same as in §10 with the bottom electrode having the following shape:

$$z(x) = Z_c + \frac{d_b}{\pi}\left(\arctan\left(\frac{x - x_l}{d_c}\right) - \arctan\left(\frac{x - x_r}{d_c}\right)\right) \tag{12.1}$$

where d_c determines the steepness of the steps with smaller values of the parameter corresponding to steeper steps; $x_r - x_l$ gives the width of the step. Throughout this chapter we shall consider a system with the following parameters: $Z_c = 0.2$, $d_b = 0.8$, $d_c = 10^{-2}$, $x_r - x_l = \pi$.

12.1. Flow over a step in the absence of electric fields

We begin our analysis by considering flow over a step in the absence of electric fields in order to check if our model is consistent with previous studies, such as the work of Tseluiko *et al.* (2013) and Lenz & Kumar (2007). Both consider steady states of flow over a step with Tseluiko *et al.* (2013) analysing gravity-driven flow of one layer of fluid and Lenz & Kumar (2007) investigating the behaviour of the interface between two fluids flowing over a step without an incline. We consider steady state solutions of the system which are found with the help of our steady state numerical solver outlined in chapter 10.

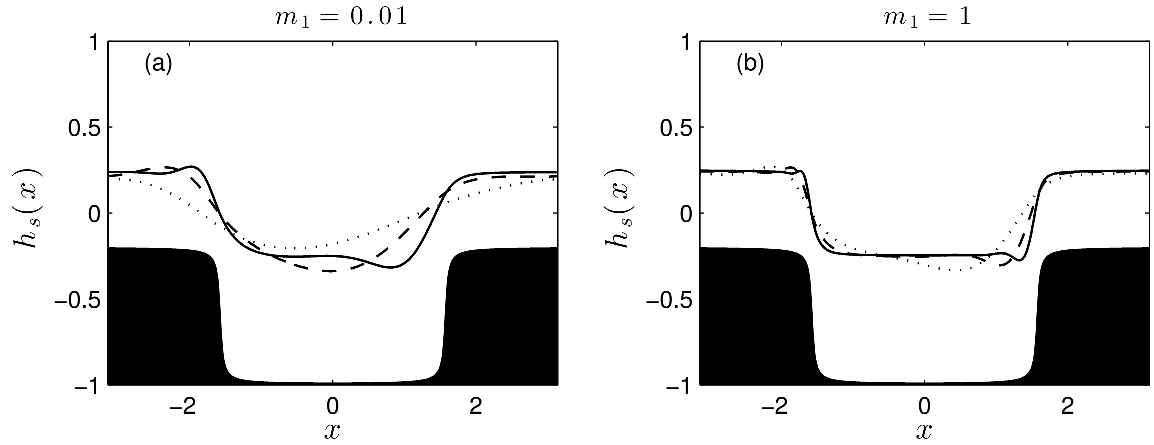

Figure 12.1. Steady state profiles of the interfacial height $h_s(x)$ with no applied electric field for varying flux $Q = 1$ (dotted line), $Q = 10$ (dashed line), $Q = 100$ (solid line). Viscosity ratio is (a) $m_1 = 0.01$ and (b) $m_1 = 1$.

Figures 12.1 give the interfacial height profiles for three different values of the flux Q. Figure 12.1.a shows steady state solutions for the case when the top fluid has a much lower viscosity then the bottom one and this is a reasonable approximation for the one fluid flow examined by Tseluiko *et al.* (2013). Figure 12.1.b gives steady state solutions for the case when both the top and the lower fluid have the same viscosity and this is similar to the setup considered by Lenz & Kumar (2007). In both cases smaller fluxes lead to smoother solutions and changes in the viscosity ratio have relatively small effects, with capillary ridges decreasing in height as the viscosity ratio increases which is in agreement with previous findings (Lenz & Kumar, 2007). The profiles in figure 12.1.a are qualitatively similar to the ones found by Tseluiko *et al.* (2013) and the ones in 12.1.b are in agreement with those described by Lenz & Kumar (2007). This reassures us of the validity of our model and we proceed to investigate the system in the presence of electric fields.

12.2. Floquet analysis for varying voltage

In this section we consider flow over a step under the effect of electric fields. We investigate the stability of the system as we vary the voltage with the help of the Floquet analysis outlined in §10.8. Throughout this chapter we vary the voltage V_b and fix all the other parameters: $\tilde{Q} = 0.0345$, $\epsilon_1 = 1$, $\epsilon_2 = 2$, $m_{1,2} = 1$, $\beta = 1$.
Figure 12.2 gives the plots of the real and imaginary parts of the eigenvalues λ as we

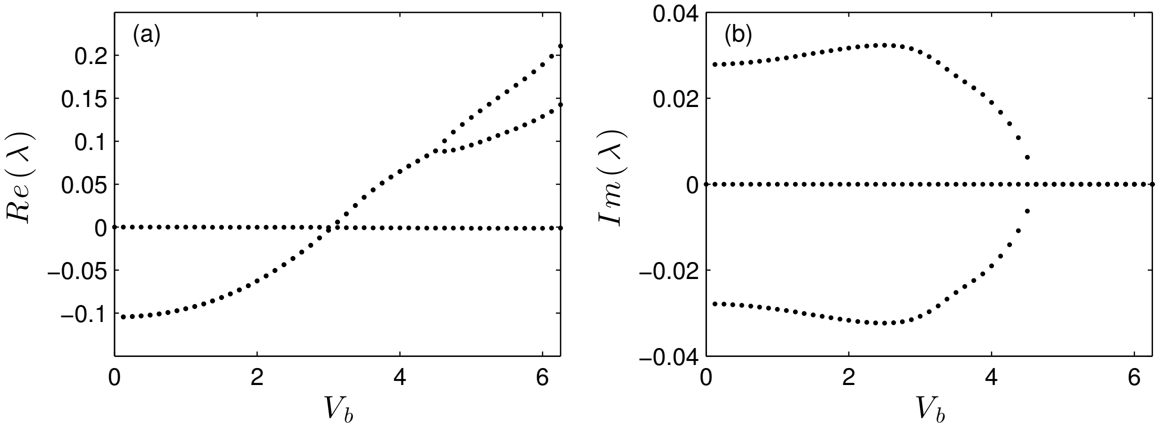

Figure 12.2. (a) Real and (b) imaginary parts of the growth rate λ vs applied voltage V_b. Bottom has step.

vary the applied voltage V_b. The first crossing of eigenvalues in figure 12.2 occurs at $V_b = 3$ so the system is stable below that value. The branch of real parts of eigenvalues splits into two branches at $V_b = 4.5$ which suggests there might be a change from one type of behaviour to another. As before we make use of the energy $E(t)$ and examine the plots of the L^2-norm of h against time for two values of the voltage, one above $V_b = 4.5$ and one below. Figures 12.3.a,b are plots of $E(t)$ of the system for $V_b = 4$ and $V_b = 5$ respectively and for the latter we observe that $E(t)$ has more oscillations and a more intricate structure. The differences in the dynamics can be further illustrated in the phase planes of the energy for $V_b = 4$ and $V_b = 5$ in figures 12.3.c,d. The results suggest that the two solutions are on different branches and the transition from one branch to the other occurs at $V_b = 4.5$ where the real parts of eigenvalues appear to bifurcate.

We compare these findings with the full time dependant solutions for $V_b = 4$ (see figure 12.4) and $V_b = 5$ (see figure 12.5). In the first case we have a time modulated travelling wave with peaks forming over the edges of the step. In the second case we have a peak forming over the left step which oscillates but fails to travel. These findings are in agreement with our Floquet analysis: in the first case we have a non-zero wave speed which corresponds to the non-zero imaginary part of the eigenvalues λ when $V_b = 4$; in the second case the wave does not travel and indeed the imaginary part of the eigenvalues is zero for $V_b = 5$.

Through the use of Floquet theory we have identified three different regimes. The system is fully stable below $V_b = 3$, when for $3 \leq V_b \leq 4.5$ the solution is in the form of time modulated travelling waves and for $4.5 \leq V_b$ the interface oscillates without travelling.

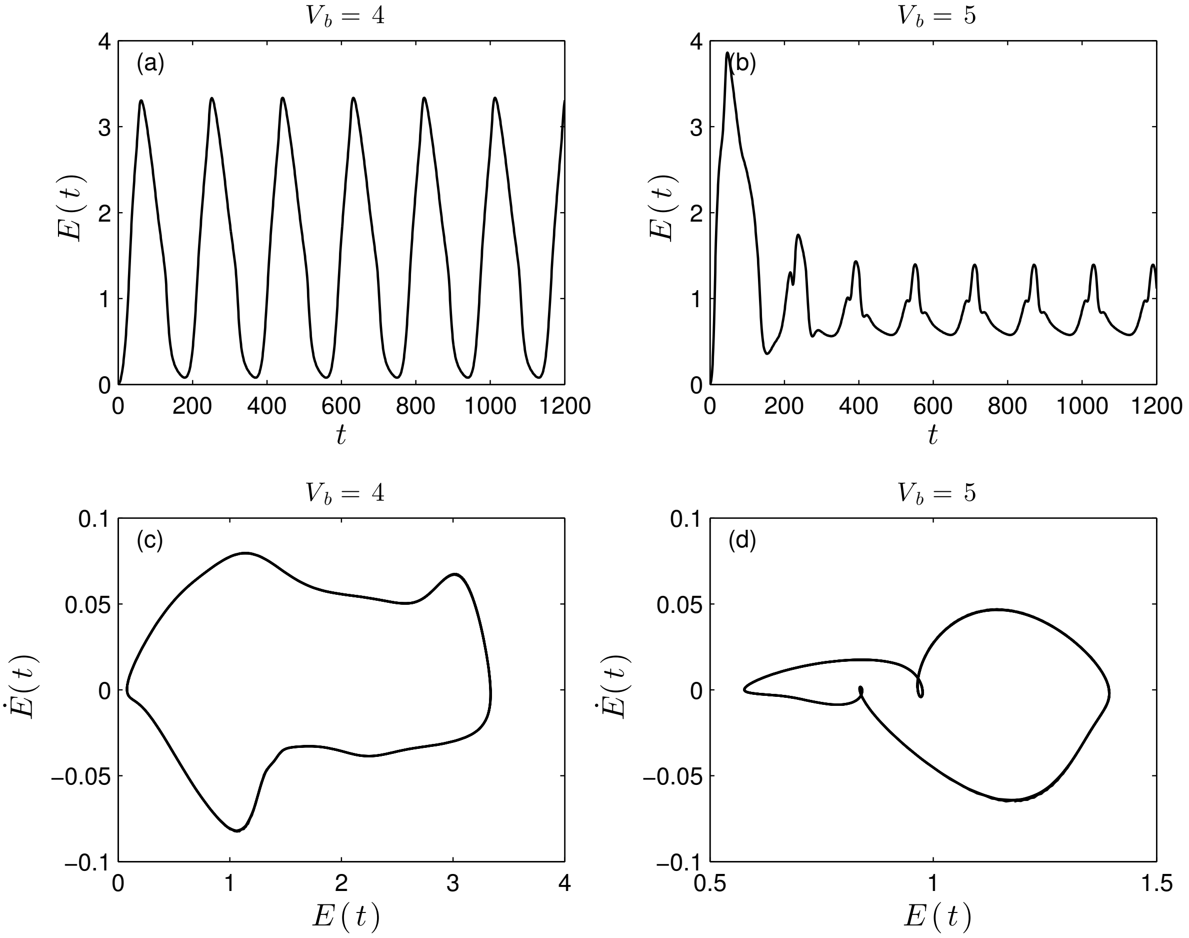

Figure 12.3. Top panels show $E(t)$ plotted as time is varied for (a) $V_b = 4$ and (b) $V_b =$. The bottom figures show the phase plane of the energy for (c) $V_b = 4$ and (d) $V_b = 5$.

12.3. Summary of research

We have examined the behaviour of an interface between two perfect dielectric fluids that flow over a step. First we investigated the steady states of the system in absence of electric fields and found that the interface tends to mimic the interface with lower fluxes leading to smoother profiles. For higher fluxes we recovered the capillary ridges and troughs that form preceding the step-down and the step-up respectively that were analysed by Lenz & Kumar (2007). We then examined the stability of the system for changing applied voltage with the help of a Floquet analysis. The plots of the eigenvalues suggest three different regimes: the system is completely stable below a certain value of the voltage, then we see time modulated travelling waves for a range of voltages and finally for voltages above a certain value we have an oscillating solution that does not travel. The points when the behaviour of the system appears to change found from the stability analysis are in perfect agreement with the full time dependant simulations.

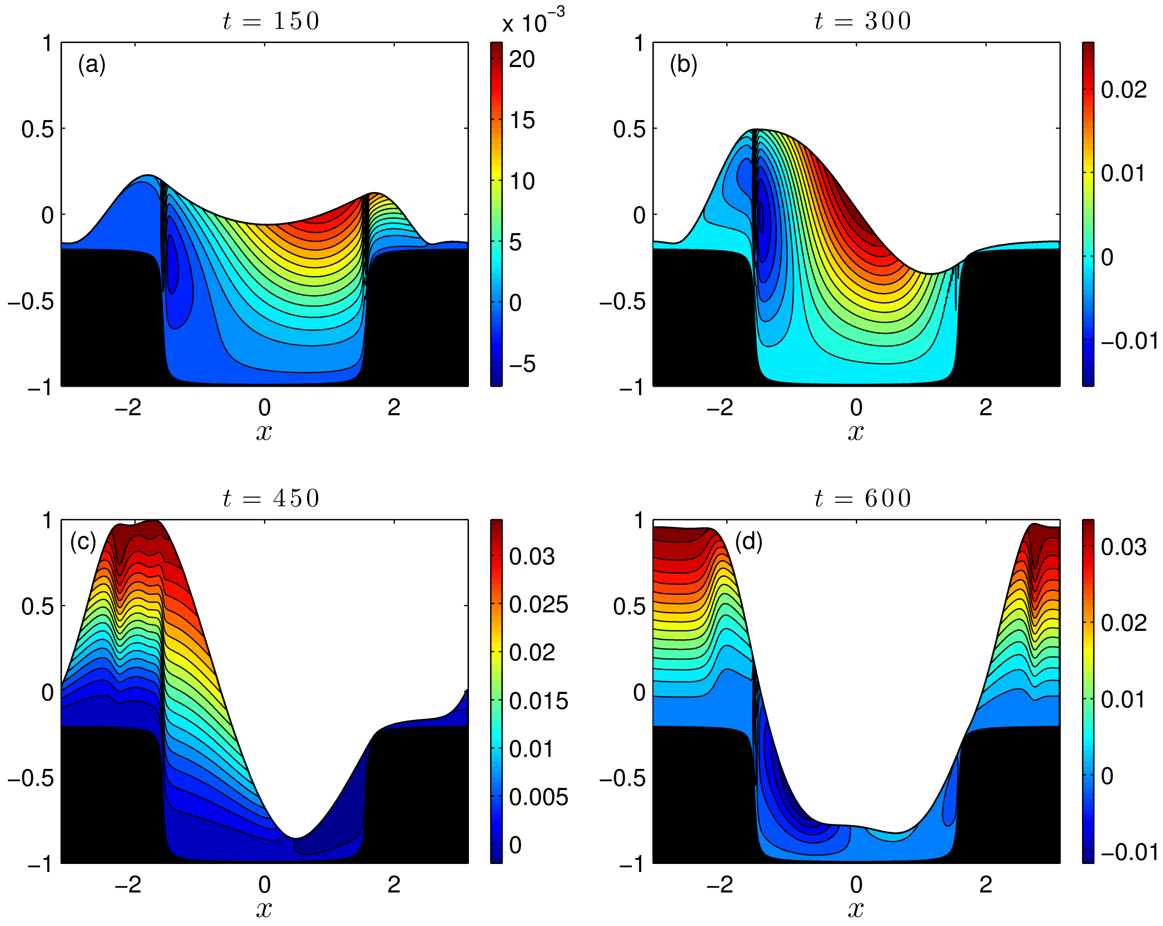

Figure 12.4. Interface and streamlines for $V_b = 4$ at (a) $t = 150$, (b) $t = 300$, (c) $t = 450$ and (d) $t = 600$.

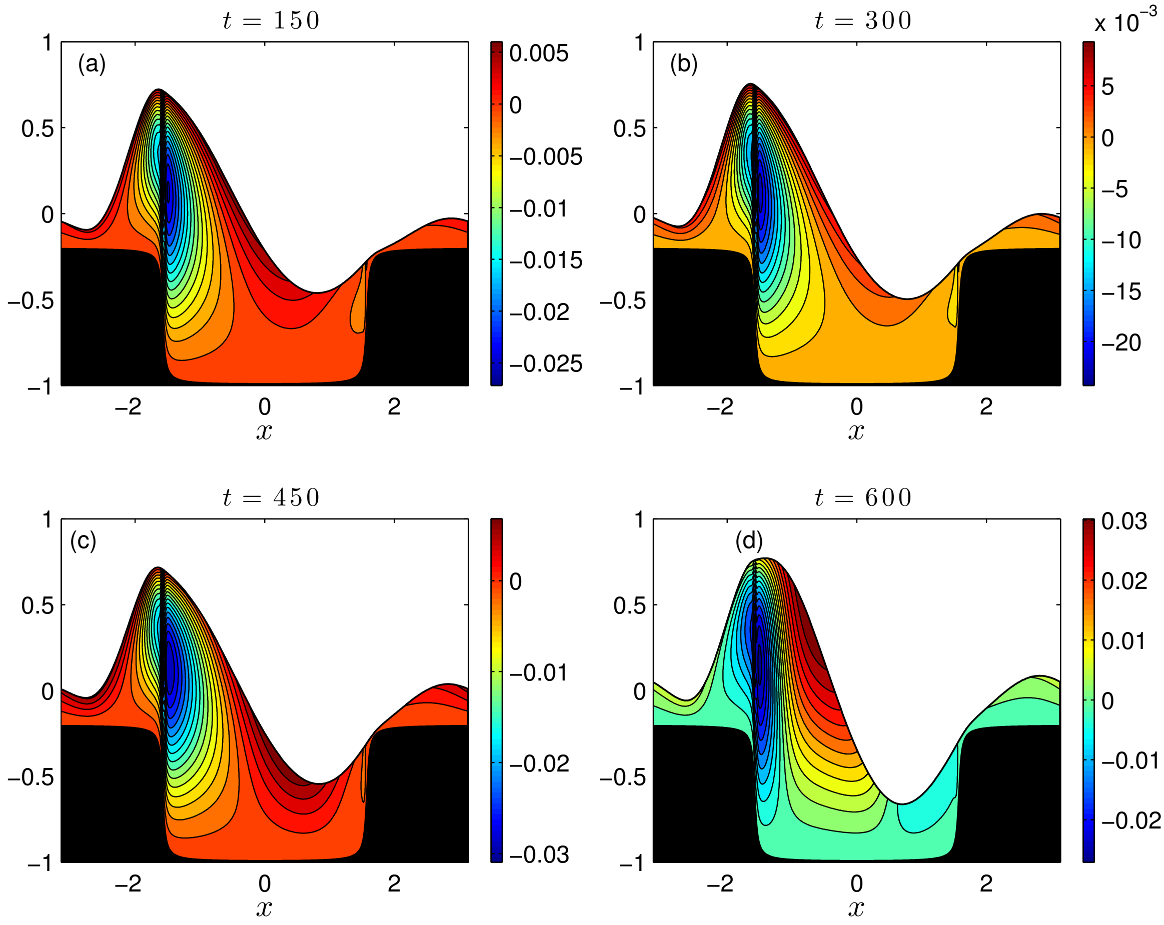

Figure 12.5. Interface and streamlines for $V_b = 5$ at (a) $t = 150$, (b) $t = 300$, (c) $t = 450$ and (d) $t = 600$.

13. Concluding remarks

We have presented a mathematical model for the behaviour of an interface between two fluids that flow between two electrodes. The fluids can be either taken to be perfect dielectrics, where no free charge is present, or leaky dielectrics, where the charge accumulates at the interface. In the latter case a current conservation equation based on Ohmic conductivity needs to be included. A long-wavelength approximation is made to derive time dependant evolution equations for the interface and the charge which are one dimensional in space. The system is parametrized by the dimensionless flow rate, voltage and ratios of viscosities and permittivities. The evolution equations are solved numerically using two FORTRAN codes which are both based on the method of lines and Gear's method for the time integration.

We begin by analysing the stability of an electrified fluid sheet under the effect of a tangential electric field in the case when the ratio of fluid to electric time scales is taken to be of $O(1)$. We find that instability occurs if $\epsilon_p\sigma_R > 1$, where ϵ_p is the ratio of dielectric permittivities and σ_R is the ratio of electric conductivities. This result is in agreement with previous work by Papageorgiou & Petropoulos (2004) and Ozen *et al.* (2006). Our numerical solution suggests that rupture of the sheet can occur at finite times with the horizontal fluid velocity and the surface charge becoming locally unbounded. A similarity solution of the second kind is presented for the behaviour of the system near rupture.

We move on to exploring the behaviour of the interface between two leaky dielectric fluids flowing with a constant flow rate between two flat electrodes held at constant voltages. A linear stability analysis shows that there exists a band of unstable modes and that electrical effects are destabilising while changes in the overall flow rate do not affect the value of the critical wavenumber required for instability. Numerical results show that initially small perturbations grown and develop into time modulated travelling waves that move at constant speed. Increasing the overall flow rate leads to higher wave speeds and smaller wave amplitudes which suggests that the electrically induced patterns analysed by Craster & Matar (2005) can be "swept away" by higher fluxes.

In our next section we consider a similar setup but this time we assume that the fluids are perfect dielectrics and we introduce a corrugation on the bottom electrode. We initially consider a sinusoidal lower boundary of relatively small amplitudes and find that the interface either reaches a steady state which mimics the shape of the corrugation or forms travelling structures that are reminiscent of the ones found in the case of flat boundaries but which are now sliding over the patterned wall. For small amplitude corrugations there is a correlation between the critical voltage for which the transition between the two types of solution happens and the linear stability analysis for a flat lower boundary. However, the information found from the latter is no longer sufficient to determine the ranges of voltages for various types of solutions in the case of sinusoidal boundaries of larger amplitude. In this case we make use of a Floquet stability analysis which is better suited for problems with a non uniform base state. Our numerical solutions help us identify a few different types of dynamics which occur at different values of the applied voltage and our Floquet analysis gives the ranges of voltages for which these behaviours are possible. Below a critical voltage the system reaches a steady state with the same wavenumber as the lower boundary. For a range of voltages the interface appears to "slide" over the corrugation and for higher voltages the interface has yet another behaviour which we call "walking" motion. The differences between the dynamics of the two cases are clearly seen when comparing the L^2-norms of h: in the second case we have a more intricate structure. The transition from one type of behaviour to the other occurs for a voltage at which the branches of the real parts of the eigenvalues found from the Floquet analysis cross. We also analyse the behaviour of the solution for relatively large fluxes and find that the frequency of oscillation of the interface is proportional to the value of the overall flow rate.

Having established a robust linear stability analysis based on Floquet theory we seek to apply it to different geometries. We include a corrugation to the top boundary and analyse two cases: one where the top has the same shape as the lower boundary but is offset by π and another one where the top and bottom corrugations are symmetrical. A Floquet analysis shows that the critical voltage required for instability is not affected by the addition of the waviness to the top boundary. In the case of the offset top we find a range of voltages for which the interface has a "walking" motion and another range for which the interface takes the wavenumber of the boundaries and "slides" over them. The second type of behaviour was not found in the case of just one flat boundary. In the case of two symmetrical boundaries there is a range of "walking" solutions but above a critical voltage the interface approaches the upper wall very closely and fixes in a pattern that slowly drains much like the patterns found by Craster & Matar (2005). Finally, an analytical solution is found for shallow boundaries of any shape which is in good agreement with our full numerical solution.

In the final chapter we examine the case of flow over a step with a flat top electrode. Through a comparison between full numerical solutions and the plots of the eigenvalues found from Floquet analysis we identify three different types of behaviour. For low enough voltages the interface reaches a steady state. For a range of voltages it travels in a time modulated fashion and at higher voltages it oscillates without travelling.

In all of the above cases we have also looked at the streamlines of the fluid in the lower layer and found that for certain values of the voltage and the flow rate we have vortices in the troughs which could be used for cell trapping in bioanalytical applications. The intricate behaviour of the "walking" motion is particularly suited to enhance mixing within one of the layers. We now have a useful tool based on Floquet theory which helps us to determine the ranges of voltages for which each type of behaviour occurs. Often it is enough to change the voltage to produce a completely different type of dynamics which can be exploited in microfluidic devices.

The system has a rich variety of behaviours and we have chosen to analyse and present a few of the most interesting cases. However we have developed a numerical scheme and a routine for calculating the eigenvalues in the Floquet analysis which so far have given results which are in excellent agreement with each other. It would be fairly straightforward to use our numerical setup to analyse systems with different geometries and different values of the physical parameters to discover more interesting dynamics with potential applications in microfluidic devices.

One possible way to expand this investigation would be to test the results presented in chapter 10 in an experimental setup to see if changing the applied voltage in a microfluidic two phase flow can indeed produce an environment that is either favourable for mixing or cell trapping. Moreover, the mixing behaviour could be investigated further by conducting an analysis of the system with a passive tracer. Finally, the quasi periodicity of the system described in chapter 10 can be explored by analysing the return maps of the energy.

Bibliography

Akrivis, G. , Papageorgiou, D. T. & Smyrlis, Y.-S. 2011 Linearly implicit methods for a semi linear parabolic system arising in two-phase flows. *IMA Journal of Numerical Analysis* **31**, 299–321.

Andersen, M. B. & Bruus, H. 2012 Electrokinetics of nanochannels and porous membranes with dynamic surface charges. PhD thesis, Technical University of Denmark, Department of Micro-and Nanotechnology.

Andersen, M. B. , Soestbergen, M. V. , Mani, A. , Bruus, H. , Biesheuvel, P. M. & Bazant, M. Z. 2012 Current-induced membrane discharge. *Physical Review Letters* **109** (10), 108301.

Andersson, H. & van den Berg, A. 2003 Microfluidic devices for cellomics: a review. *Sensors and actuators B: Chemical* **92** (3), 315–325.

Balmforth, N. J. & Craster, R. V. 2000 Dynamics of cooling domes of viscoplastic fluid. *Journal of Fluid Mechanics* **422**, 225–248.

Baral, D. R. , Hutter, K. & Greve, R. 2001 Asymptotic theories of large-scale motion, temperature, and moisture distribution in land-based polythermal ice sheets: a critical review and new developments. *Applied Mechanics Reviews* **54** (3), 215–256.

Barannyk, L. , Papageorgiou, D. T. , Petropoulos, P. & Vanden-Broeck, J.-M. 2015*a* Nonlinear dynamics and wall touch-up in unstably stratified multilayer flows in horizontal channels under the action of electric fields. *SIAM Journal on Applied Mathematics* **75**, 92–113.

Barannyk, L. L. , Papageorgiou, D. T. & Petropoulos, P. G. 2012 Suppression of RayleighTaylor instability using electric fields. *Mathematics and Computers in Simulation* **82** (6), 1008–1016.

Barannyk, L. L. , Papageorgiou, D. T. , Petropoulos, P. G. & Vanden-Broeck, J. M. 2015*b* Nonlinear dynamics and wall touch-up in unstably stratified multilayer flows in horizontal channels under the action of electric fields. *SIAM Journal on Applied Mathematics* **75** (1), 92–113.

Ben, Y. & Chang, H. C. 2002 Nonlinear Smoluchowski slip velocity and micro-vortex generation. *Journal of Fluid Mechanics* **461**, 229–238.

Chang, H. C. & Yeo, L. Y. 2010 *Electrokinetically driven microfluidics and nanofluidics*. Cambridge University Press.

Chang, H. C. , Yossifon, G. & E. A Demekhin, E. A. 2012 Nanoscale electrokinetics and microvortices: how microhydrodynamics affects nanofluidic ion flux. *Annual Review of Fluid Mechanics* **44**, 401–426.

Cheng, L. J. & Chang, H. C. 2011 Microscale pH regulation by splitting water. *Biomicrofluidics* **5** (4), 046502.

Chou, S. Y. & Zhuang, L. 1999 Lithographically induced self-assembly of periodic polymer micropillar arrays. *Journal of Vacuum Science & Technology B* **17** (6), 3197–3202.

Cimpeanu, R. , Papageorgiou, D. T. & Petropoulos, P. G. 2014 On the control and suppression of the Rayleigh-Taylor instability using electric fields. *Physics of Fluids (1994-present)* **26** (2), 022105.

Conroy, D. T. , Craster, R. V. , Matar, O. K. , Cheng, L. J. & Chang, H. C. 2012 Nonequilibrium hysteresis and wien effect water dissociation at a bipolar membrane. *Physical Review E* **86** (5), 056104.

Corless, R. M. , Gonnet, G. H. , Hare, D. E. , Jeffrey, D. J. & Knuth, D. E. 1996 On the Lambert W function. *Advances in Computational mathematics* **5** (1), 329–359.

Craster, R. V. & Matar, O. K. 2005 Electrically induced pattern formation in thin leaky dielectric films. *Physics of Fluids (1994-present)* **17** (3), 032104.

Craster, R. V. & Matar, O. K. 2009 Dynamics and stability of thin liquid films. *Reviews of modern physics* **81** (3), 1131.

Dubrovina, E. , Craster, R. V. & Papageorgiou, D. T. 2016 Two layer electrified pressure-driven flow in topographically structured channels. *Journal of Fluid Mechanics, Submitted for publication* .

EIJKEL, J. & BERG, A. V. D. 2005 Nanofluidics: what is it and what can we expect from it? *Microfluidics and Nanofluidics* **1** (3), 249–267.

ERICKSON, D. & LI, D. 2004 Integrated microfluidic devices. *Analytica Chimica Acta* **507** (1), 11–26.

ERNEUX, T. & DAVIS, S. H. 1993 Nonlinear rupture of free films. *Physics of Fluids A: Fluid Dynamics (1989-1993)* **5** (5), 1117–1122.

FEYNMAN, R. P. , LEIGHTON, R. B. & SANDS, M. 1979 *The Feynman lectures on physics*, , vol. 2.

FRILETTE, V. J. 1957 Electrogravitational transport at synthetic ion exchange membrane surfaces. *The Journal of Physical Chemistry* **61** (2), 168–174.

GASKELL, P. H. , JIMACK, P. K. , SELLIER, M. , THOMPSON, H. M. & WILSON, M. C. T. 2004 Gravity-driven flow of continuous thin liquid films on non-porous substrates with topography. *Journal of Fluid Mechanics* **509**, 253–280.

GRANDISON, S. , PAPAGEORGIOU, D. T. & VANDEN-BROECK, J. M. 2007 Interfacial capillary waves in the presence of electric fields. *European Journal of Mechanics-B/Fluids* **26** (3), 404–421.

GROTBERG, J. B. 1994 Pulmonary flow and transport phenomena. *Annual Review of Fluid Mechanics* **26** (1), 529–571.

GUBALA, V. , HARRIS, L. F. , RICCO, A. J. , TAN, M. X. & WILLIAMS, D. E. 2011 Point of care diagnostics: status and future. *Analytical chemistry* **84** (2), 487–515.

HUNT, M. , PAPAGEORGIOU, D. T. & VANDEN-BROECK, J. M. 2014 Electrostatic effects on linear and nonlinear waves in hanging film flows. *Procedia IUTAM* **11**, 58–68.

HUPPERT, H. E. 2006 Gravity currents: a personal perspective. *Journal of Fluid Mechanics* **554**, 299–322.

KARAPETSAS, G. & BONTOZOGLOU, V. 2015 Non-linear dynamics of a viscoelastic film subjected to a spatially periodic electric field. *Journal of Non-Newtonian Fluid Mechanics* **217**, 1–13.

KHANDURINA, J. & GUTTMAN, A. 2002 Bioanalysis in microfluidic devices. *Journal of Chromatography A* **943** (2), 159–183.

KINDAL, E. & ATKINSON, P. 1997 *The numerical solution of integral equations of the second kind*, , vol. 4. Cambridge University Press.

KNUTTON, S. 1979 Studies of membrane fusion. V. Fusion of erythrocytes with non-haemolytic Sendai virus. *Journal of cell science* **36** (1), 85–96.

KO, S. H. , SONG, Y. A. , KIM, S. J. , KIM, M. , HAN, J. & KANG, K. H. 2012 Nanofluidic preconcentration device in a straight microchannel using ion concentration polarization. *Lab on a Chip* **12** (21), 4472–4482.

KOHLHEYER, D. , EIJKEL, J. C. , SCHLAUTMANN, S. , VAN DEN BERG, A. & SCHASFOORT, R. B. 2007 Microfluidic high-resolution free-flow isoelectric focusing. *Analytical chemistry* **79** (21), 8190–8198.

KUMAR, K. , NIKOLOV, A. D. & WASAN, D. T. 2002 Effect of film curvature on drainage of thin liquid films. *Journal of Colloid and Interface Science* **256** (1), 194–200.

LEE, J. H. , SONG, Y. A. & HAN, J. 2008 Multiplexed proteomic sample preconcentration device using surface-patterned ion-selective membrane. *Lab on a Chip* **8** (4), 596–601.

LEFEBVRE, A. 1988 *Atomization and sprays*, , vol. 1040. CRC press.

LENZ, R. D. & KUMAR, S. 2007 Steady two-layer flow in a topographically patterned channel. *Physics of Fluids (1994-present)* **19** (10), 102103.

LEVICH, V. G. 1962 *Physicochemical hydrodynamics*, , vol. 689. Prentice-Hall.

LI, F. , OZEN, O. , AUBRY, N. , PAPAGEORGIOU, D. T. & PETROPOULOS, P. G. 2007 Linear stability of a two-fluid interface for electrohydrodynamic mixing in a channel. *Journal of Fluid Mechanics* **583**, 347–377.

LIU, Y. , MO, C. , LIU, L. , FU, Q. & YANG, L. 2016 Linear stability analysis of an electrified incompressible liquid sheet streaming into a compressible ambient gas. *Proceedings of the Institution of Mechanical Engineers, Part C: Journal of Mechanical Engineering Science* p. 0954406215625674.

LUO, H. & POZRIKIDIS, C. 2006 Shear-driven and channel flow of a liquid film over a corrugated or indented wall. *Journal of Fluid Mechanics* **556**, 167–188.

MADSEN, N. K. & SINCOVEC, R. F. 1979 Algorithm 540: PDECOL, general collocation software for partial differential equations. *ACM Transactions on Mathematical Software (TOMS)* **5** (3), 326–351.

MAEHLMANN, S. & PAPAGEORGIOU, D. T. 2011 Interfacial instability in electrified plane couette flow. *Journal of Fluid Mechanics* **666**, 155–188.

MAFE, S. & RAMIREZ, P. 1997 Electrochemical characterization of polymer ion exchange bipolar membranes. *Acta polymerica* **48** (7), 234–250.

MANZANARES, J. A. , ABD S. MAFE, W. D. M. & REISS, H. 1993 Numerical simulation of the nonequilibrium diffuse double layer in ion-exchange membranes. *The Journal of Physical Chemistry* **97** (32), 8524–8530.

MARRUCCI, G. 1969 A theory of coalescence. *Chemical engineering science* **24** (6), 975–985.

MAZOUCHI, A. & HOMSY, G. M. 2001 Free surface Stokes flow over topography. *Physics of Fluids (1994-present)* **13** (10), 2751–2761.

MELCHER, J. R. & SCHWARZ, J. W. J. 1968 Interfacial relaxation overstability in a tangential electric field. *Physics of Fluids (1958-1988)* **11** (12), 2604–2616.

MELCHER, J. R. & SMITH, C. V. 1969 Electrohydrodynamic charge relaxation and interfacial perpendicular field instability. *Physics of Fluids* **12** (4), 778–790.

MELCHER, J. R. & TAYLOR, G. I. 1969 Electrohydrodynamics: a review of the role of interfacial shear stresses. *Annual Review of Fluid Mechanics* **1** (1), 111–146.

MIKSIS, M. J. & IDA, M. P. 1998*a* The dynamics of thin films I: General theory. *SIAM Journal on Applied Mathematics* **58** (2), 456–473.

MIKSIS, M. J. & IDA, M. P. 1998*b* The dynamics of thin films II: Applications. *SIAM Journal on Applied Mathematics* **58** (2), 474–500.

NIE, Z. & KUMACHEVA, E. 2008 Patterning surfaces with functional polymers. *Nature Materials* **7** (4), 277–290.

ONSAGER, L. 1934 Deviations from Ohm's law in weak electrolytes. *The Journal of Chemical Physics* **2**, 599.

Ozen, O. , Papageorgiou, D. T. & Petropoulos, P. G. 2006 Nonlinear stability of a charged electrified viscous liquid sheet under the action of a horizontal electric field. *Physics of Fluids (1994-present)* **18** (4), 042102.

Papaefthymiou, E. S. , Papageorgiou, D. T. & Pavliotis, G. A. 2013 Nonlinear interfacial dynamics in stratified multilayer channel flows. *Journal of Fluid Mechanics* **734**, 114–143.

Papageorgiou, D. T. & Petropoulos, P. G. 2004 Generation of interfacial instabilities in charged electrified viscous liquid films. *Journal of engineering mathematics* **50** (2-3), 223–240.

Papageorgiou, D. T. & Vanden-Broeck, J. M. 2004*a* Antisymmetric capillary waves in electrified fluid sheets. *European Journal of Applied Mathematics* **15** (06), 609–623.

Papageorgiou, D. T. & Vanden-Broeck, J. M. 2004*b* Large-amplitude capillary waves in electrified fluid sheets. *Journal of Fluid Mechanics* **508**, 71–88.

Pease, L. F. & Russell, W. B. 2002 Linear stability analysis of thin leaky dielectric films subjected to electric fields. *Journal of Non-Newtonian Fluid Mechanics* **102** (2), 233–250.

Petzold, L. R. 1982 A description of DASSL: A differential/algebraic system solver. *Proc. IMACS World Congress* pp. 430–432.

Pollak, T. & Aksel, N. 2013*a* Crucial flow stabilisation and multiple instability branches of gravity-driven films over topography. *Phys. Fluids* **25**, 024103.

Pollak, T. & Aksel, N. 2013*b* Crucial flow stabilization and multiple instability branches of gravity-driven films over topography. *Physics of Fluids (1994-present)* **25** (2), 024103.

Ramkrishnan, A. & Kumar, S. 2013 Electrohydrodynamic effects in the leveling of coatings. *Chemical Engineering Science* **101**, 785–799.

Ramkrishnan, A. & Kumar, S. 2014 Electrohydrodynamic deformation of thin liquid films near surfaces with topography. *Physics of Fluids (1994-present)* **26** (12), 122110.

Rubinstein, I. & Zaltzman, B. 2000 Electro-osmotically induced convection at a permselective membrane. *Physical Review E,* **62** (2), 2238.

Rubinstein, S. M. , Manukyan, G. , Staicu, A. , Rubinstein, I. , Zaltzman, B. , Lammertink, R. G. H. , Mugele, F. & Wessling, M. 2008 Direct observation of a nonequilibrium electro-osmotic instability. *Physical review letters,* **101** (23), 236101.

Savettaseranee, K. , Papageorgiou, D. T. , Petropoulos, P. G. & Tilley, B. S. 2003 The effect of electric fields on the rupture of thin viscous films by van der Waals forces. *Physics of Fluids (1994-present)* **15** (3), 641–652.

Saville, D. A. 1997 Electrohydrodynamics: the Taylor-Melcher leaky dielectric model. *Annual review of fluid mechanics* **29** (1), 27–64.

Schaffer, E. , Thurn-Albrecht, T. , Russell, T. P. & Steiner, U. 2000 Electrically induced structure formation and pattern transfer. *Nature* **403** (6772), 874–877.

Schaffer, E. , Thurn-Albrecht, T. , Russell, T. P. & Steiner, U. 2001 Electrohydrodynamic instabilities in polymer films. *EPL (Europhysics Letters)* **53** (4), 518.

Schiesser, W. E. 2012 *The numerical method of lines: integration of partial differential equations*. Elsevier.

Schorner, M. , Reck, D. & Aksel, N. 2015 Does the topographys specific shape matter in general for the stability of film flows? *Physics of Fluids (1994-present)* **27** (4), 042103.

Schweizer, P. & Kistler, S. 2012 *Liquid Film Coating: Scientific principles and their technological implications*. Springer Science & Business Media.

Sheludko, A. 1967 Thin liquid films. *Advances in Colloid and Interface Science* **1** (4), 391–464.

Slouka, Z. , Senapati, S. & Chang, H. C. 2014 Microfluidic systems with ion-selective membranes. *Annual Review of Analytical Chemistry* **7**, 317–335.

Sollner, K. 1950 Recent advances in the electrochemistry of membranes of high ionic selectivity. *Journal of The Electrochemical Society* **97** (7), 139C–151C.

SooHoo, J. R. & Walker, G. M. 2009 Microfluidic aqueous two phase system for leukocyte concentration from whole blood. *Biomedical microdevices* **11** (2), 323–329.

Strathmann, H. , Grabowski, A. & Eigenberger, G. 2013 Ion-exchange membranes in the chemical process industry. *Industrial & Engineering Chemistry Research* **52** (31), 10364–10379.

Tilley, B. S. , Petropoulos, P. G. & Papageorgiou, D. T. 2001 Dynamics and rupture of planar electrified liquid sheets. *Physics of Fluids (1994-present)* **13** (12), 3547–3563.

Toner, M. & Irimia, D. 2005 Blood-on-a-chip. *Annual review of biomedical engineering* **7**, 77.

Tseluiko, D. & Blyth, M. G. 2009 Effect of inertia on electrified film flow over a wavy wall. *Journal of Engineering Mathematics* **65** (3), 229–242.

Tseluiko, D. , Blyth, M. G. & Papageorgiou, D. T. 2013 Stability of film flow over inclined topography based on a long-wave nonlinear model. *Journal of Fluid Mechanics* **729**, 638–671.

Tseluiko, D. , Blyth, M. G. , Papageorgiou, D. T. & Vanden-Broeck, J. M. 2008*a* Effect of an electric field on film flow down a corrugated wall at zero Reynolds number. *Physics of Fluids (1994-present)* **20** (4), 042103.

Tseluiko, D. , Blyth, M. G. , Papageorgiou, D. T. & Vanden-Broeck, J. M. 2008*b* Electrified viscous thin film flow over topography. *Journal of Fluid Mechanics* **597**, 449–475.

Tseluiko, D. & Papageorgiou, D. T. 2007*a* Dynamics of a viscous thread surrounded by another viscous fluid in a cylindrical tube under the action of a radial electric field: breakup and touchdown singularities. *SIAM Journal on Applied Mathematics* **67**, 1310–1329.

Tseluiko, D. & Papageorgiou, D. T. 2007*b* Nonlinear dynamics of electrified thin liquid films. *SIAM Journal on Applied Mathematics* **67**, 1310–1329.

Vaynblat, D. , Lister, J. R. & Witelski, T. P. 2001 Rupture of thin viscous films by van der Waals forces: Evolution and self-similarity. *Physics of Fluids (1994-present)* **13** (5), 1130–1140.

Wang, Y. , Pant, K. , Chen, Z. , Wang, G. , Diffey, W. F. , Ashley, P. & Sundaram, S. 2009 Numerical analysis of electrokinetic transport in micro-nanofluidic interconnect preconcentrator in hydrodynamic flow. *Microfluidics and nanofluidics* **7** (5), 683–696.

Wang, Y. C. , Stevens, A. L. & Han, J. 2005 Million-fold preconcentration of proteins and peptides by nanofluidic filter. *Analytical chemistry* **77** (14), 4293–4299.

Weinstein, S. J. & Ruschak, K. J. 2004 Coating flows. *Annu. Rev. Fluid Mech.* **36**, 29–53.

Wu, N. & Russell, W. B. 2009 Micro-and nano-patterns created via electrohydrodynamic instabilities. *Nano Today* **4** (2), 180–192.

Xu, T. 2005 Ion exchange membranes: state of their development and perspective. *Journal of Membrane Science* **263** (1), 1–29.

Yang, Q. , Li, B. Q. & Ding, Y. 2013*a* 3D phase field modeling of electrohydrodynamic multiphase flows. *International Journal of Multiphase Flow* **57**, 1–9.

Yang, Q. , Li, B. Q. & Ding, Y. 2013*b* A numerical study of nanoscale electrohydrodynamic patterning in a liquid film. *Soft Matter* **9** (12), 3412–3423.

Yi, C. , Li, C. W. , Ji, S. & Yang, M. 2006 Microfluidics technology for manipulation and analysis of biological cells. *Analytica Chimica Acta* **560** (1), 1–23.

Yih, C.-S. 1967 Instability due to viscosity stratification. *Journal of Fluid Mechanics* **27**, 337–352.

Yossifon, G. , Mushenheim, P. , Chang, Y. C. & (2009), H. C. C. 2009 Nonlinear current-voltage characteristics of nanochannels. *Physical Review E* **79** (4), 046305.

Zubarev, N. M. 2004 Nonlinear waves on the surface of a dielectric liquid in a strong tangential electric field. *Physics Letters A* **333** (3), 284–288.

Zubarev, N. M. & Kochurin, E. A. 2013 Three-dimensional nonlinear waves at the interface between dielectric fluid in an external horizontal electric field. *Journal of Applied Mechanics and Technical Physics* **54** (2), 212–217.

Zubarev, N. M. & Zubareva, O. V. 2010 Propagation of large-amplitude waves on dielectric liquid sheets in a tangential electric field: Exact solutions in three-dimensional geometry. *Physical Review E* **82** (4), 046301.

A. Appendix

A.1. Voltage potential V^{far} in the outer layer

To calculate V^{far} it is necessary to introduce an outer variable:

$$y = \frac{Y}{\delta}$$

Then equation (7.15) becomes:

$$V^{far}_{xx} + V^{far}_{YY} = 0 \tag{A.1}$$

Taking Fourier transforms of the above equation leads to the following expression for to $\hat{V}^{far}$:

$$\hat{V}^{far} = \delta\alpha_0(k,t)\exp(-|k|Y) + \delta^2\alpha_1(k,t)\exp(-|k|Y) + O(\delta^3) \tag{A.2}$$

Matching with V_1 gives:

$$\hat{V}^{far} = -\delta i\text{sgn}(k)\hat{H}_0\frac{\sigma_R - 1}{2\sigma_R}\exp(-|k|Y) + O(\delta^2) \tag{A.3}$$

We use the following manipulation to determine V^{far}:

$$\mathscr{F}^{-1}\left\{\frac{\exp(-|k|Y)}{|k|}\right\} = -\frac{1}{\pi}\log r$$

$$\mathscr{F}^{-1}\left\{\frac{-ik\exp(-|k|Y)}{|k|}\right\} = -\frac{x}{\pi r^2}$$

$$\hat{V}^{far} = \delta\mathscr{F}\left\{-\frac{x}{\pi r^2}\right\}\mathscr{F}\left\{H_0\right\}\frac{\sigma_R - 1}{2\sigma_R} + O(\delta^2)$$

$$V^{far} = \delta\frac{\sigma_R - 1}{2\sigma_R}\left(-\frac{x}{\pi r^2}\right) * (H_0) + O(\delta^2)$$

It turns out that at the boundary $y = H(x,t)$, $Y \to 0$ and so $V^{far} \to 0$.

A.2. Constants in the steady states

$$
\begin{aligned}
\bar{P}_x &= -\frac{6}{B} \\
a_1 &= \frac{m_2 a_2}{m_1} \\
a_2 &= \frac{A\bar{P}_x}{2}
\end{aligned} \tag{A.4}
$$

where

$$
\begin{aligned}
A &= \frac{m_1 - \beta^2 m_2}{m_2(m_1 + \beta m_2)} \\
B &= \frac{2\beta^3}{m_1} + \frac{2}{m_2} + \frac{3\beta^2 m_2 A}{2m_1} - \frac{3A}{2};
\end{aligned} \tag{A.5}
$$

A.3. Functions in section §7.3.4

A.3.1. Horizontal velocity and voltage potential at $O(1)$

$$
e_1(x,t) = \frac{p_x^{(0)}}{2m_1} D_5, \qquad e_2(x,t) = \frac{p_x^{(0)}}{2m_2} D_5,
$$

$$
p_x^{(0)} = \frac{1 - \int_h^\beta \bar{u}_1 dy - \int_{-z}^h \bar{u}_2 dy}{D_6}
$$

where

$$
\begin{aligned}
D_1 &= -(h-\beta)^2 \\
D_2 &= h + 2\beta \\
D_3 &= (h+z)^2 \\
D_4 &= h - 2z \\
D_5 &= \frac{m_1(z^2 - h^2) + m_2(h^2 - \beta^2)}{m_1(h+z) + m_2(\beta - h)} \\
D_6 &= \frac{m_2 D_1(2D_2 + 3D_5) + m_1 D_3(2D_4 + 3D_5)}{12 m_1 m_2}
\end{aligned} \tag{A.6}
$$

$$\begin{aligned}\int_h^\beta \bar{u}_1 dy &= D_1\left[\frac{\bar{P}_x}{6m_1}D_2+\frac{a_1}{2}\right]\\ \int_{-z}^h \bar{u}_2 dy &= D_3\left[\frac{\bar{P}_x}{6m_2}D_4+\frac{a_2}{2}\right]\end{aligned} \tag{A.7}$$

$$d_1=\frac{\epsilon_2+q^{(0)}(h+z)}{\epsilon_2(h-\beta)-\epsilon_1(h+z)}, \qquad d_2=\frac{\epsilon_1+q^{(0)}(h-\beta)}{\epsilon_2(h-\beta)-\epsilon_1(h+z)} \tag{A.8}$$

A.3.2. Horizontal velocity at $O(\delta)$

$$u_1^{(1)}=\frac{p_{1x}^{(1)}}{2m_1}(y^2-\beta^2)+f_1(x,t)(y-\beta) \tag{A.9}$$

$$u_2^{(1)}=\frac{p_{2x}^{(1)}}{2m_2}(y^2-z^2)+f_2(x,t)(y+z) \tag{A.10}$$

From eq. (7.74):

$$p_{2x}^{(1)}=p_{1x}^{(1)}-h_{xxx}-\epsilon_1 d_{1x}d_1+\epsilon_2 d_{2x}d_2 \tag{A.11}$$

From eq. (7.75):

$$m_2f_2=m_1f_1+h(p_{1x}^{(1)}-p_{2x}^{(1)})-q^{(0)}[d_1(h-\beta)]_x \tag{A.12}$$

From eq. (7.76):

$$\begin{aligned}f_1\left[(h-\beta)-\frac{m_1}{m_2}(h+z)\right] =& -p_{1x}^{(1)}\left[\frac{h^2-\beta^2}{2m_1}-\frac{h(h+z)}{m_2}\right]\\ &-p_{2x}^{(1)}\frac{(h+z)^2}{2m_2}\\ &-q^{(0)}\frac{(h+z)}{m_2}[(d_1+c_1)(h-\beta)]_x\end{aligned} \tag{A.13}$$

From eq. (7.77):

$$-D_1\left[\frac{p_{1x}^{(1)}}{6m_1}D_2+\frac{f_1}{2}\right]=D_3\left[\frac{p_{2x}^{(1)}}{6m_2}D_4+\frac{f_2}{2}\right] \tag{A.14}$$

$$\begin{aligned}
f_1(x,t) &= \frac{E_2 p_{1x}^{(1)} + E_3 p_{2x}^{(1)} + E_4 q^{(0)}}{E_1} \\
f_2(x,t) &= \frac{1}{m_2}\left\{\left[h + \frac{E_2}{E_1}m_1\right] p_{1x}^{(1)} + \left[\frac{E_3}{E_1}m_1 - h\right] p_{2x}^{(1)} + \left[\frac{E_4}{E_1}m_1 + E_5\right] q^{(0)}\right\} \\
p_{2x}^{(1)} &= \frac{-E_6(h_{xxx} + \epsilon_1 d_{1x} d_1 - \epsilon_2 d_{2x} d_2) - E_8 q^{(0)}}{E_6 + E_7}
\end{aligned} \tag{A.15}$$

$$\begin{aligned}
E_1 =& (h-\beta) - \frac{m_1}{m_2}(h+z) \\
E_2 =& -\left[\frac{h^2-\beta^2}{2m_1} - \frac{h(h+z)}{m_2}\right] \\
E_3 =& -\frac{(h+z)^2}{2m_2} \\
E_4 =& -\frac{(h+z)}{m_2}[d_1(h-\beta)]_x \\
E_5 =& -[d_1(h-\beta)]_x \\
E_6 =& -\frac{D_1 D_2}{6m_1} - \frac{E_2 D_1}{E_1} - \frac{D_3}{2}[h + (E_2 m_1/E_1)] \\
E_7 =& -\frac{D_1 E_3}{2E_1} + \frac{E_3 D_4}{3} - \frac{D_3}{2}[(E_3 m_1/E_1) - h] \\
E_8 =& -\frac{E_4 D_1}{2E_1} - \frac{D_3}{2}[(E_4 m_1/E_1) + E_5]
\end{aligned} \tag{A.16}$$

$$u_1^{(0)}|_{y=h} = (h-\beta)\left[\frac{p_x^{(0)}}{2m_1}(h+\beta) + e_1\right] \tag{A.17}$$

$$u_1^{(1)}|_{y=h} = (h-\beta)\left[\frac{p_{1x}^{(1)}}{2m_1}(h+\beta) + f_1\right] \tag{A.18}$$

Evolution equations:

$$h_t + \left\{ \frac{D_3}{6m_2} \left[D_4(\bar{P}_x + p_x^{(0)} + \delta p_{2x}^{(1)}) + 3m_2(a_2 + e_2 + \delta f_2) \right] \right\}_x = 0$$

$$q_t^{(0)} + \left\{ (h - \beta) \left[(\bar{P}_x + p_x^{(0)}) \frac{(h + \beta)}{2m_1} + a_1 + e_1 \right] q^{(0)} \right\}_x = S_1 d_1 - S_2 d_2 \qquad \text{(A.19)}$$

A.4. Pressures in section §7.3.5

$$\begin{aligned} p_{1x}^{(0)} &= p_{2x}^{(0)} + h_{xxx} + \epsilon_1 d_{1x} d_1 - \epsilon_2 d_{2x} d_2 \\ p_{2x}^{(0)} &= \frac{-E_6(h_{xxx} + \epsilon_1 d_{1x} d_1 - \epsilon_2 d_{2x} d_2) - E_8 q^{(0)}}{E_6 + E_7} - \frac{1 - \int_h^\beta \bar{u}_1 dy - \int_{-z}^h \bar{u}_2 dy}{E_6 + E_7} \end{aligned} \qquad \text{(A.20)}$$